

INFORMATION TO USERS

This manuscript has been reproduced from the microfilm master. UMI films the text directly from the original or copy submitted. Thus, some thesis and dissertation copies are in typewriter face, while others may be from any type of computer printer.

The quality of this reproduction is dependent upon the quality of the copy submitted. Broken or indistinct print, colored or poor quality illustrations and photographs, print bleedthrough, substandard margins, and improper alignment can adversely affect reproduction.

In the unlikely event that the author did not send UMI a complete manuscript and there are missing pages, these will be noted. Also, if unauthorized copyright material had to be removed, a note will indicate the deletion.

Oversize materials (e.g., maps, drawings, charts) are reproduced by sectioning the original, beginning at the upper left-hand corner and continuing from left to right in equal sections with small overlaps. Each original is also photographed in one exposure and is included in reduced form at the back of the book.

Photographs included in the original manuscript have been reproduced xerographically in this copy. Higher quality 6" x 9" black and white photographic prints are available for any photographs or illustrations appearing in this copy for an additional charge. Contact UMI directly to order.

UMI

A Bell & Howell Information Company
300 North Zeeb Road, Ann Arbor MI 48106-1346 USA
313/761-4700 800/521-0600



INCORPORATING STRUCTURAL INFORMATION INTO
INTERPRETATION OF SATELLITE IMAGES OF FORESTS

by

Degui Gu

A dissertation submitted in partial fulfillment of the
requirements for the degree of

Doctor of Philosophy

University of Washington

1998

Approved by _____

Alan G. Hillier

Chairperson of Supervisory Committee

Program Authorized
to Offer Degree _____

Geophysics Program

Date _____

June 8, 1998

UMI Number: 9836178

UMI Microform 9836178
Copyright 1998, by UMI Company. All rights reserved.
This microform edition is protected against unauthorized
copying under Title 17, United States Code.

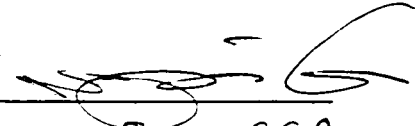
UMI
300 North Zeeb Road
Ann Arbor, MI 48103

Doctoral Dissertation

In presenting this dissertation in partial fulfillment of the requirements for the Doctoral degree at the University of Washington, I agree that the Library shall make its copies freely available for inspection. I further agree that extensive copying of this dissertation is allowable only for scholarly purposes, consistent with "fair use" as prescribed in the U.S. Copyright Law. Requests for copying or reproduction of this dissertation may be referred to University Microfilms, 1490 Eisenhower Place, P.O. Box 975, Ann Arbor, MI 48106, to whom the author has granted "the right to produce and sell (a) copies of the manuscript in microform and/or (b) printed copies of the manuscript made from microform."

Signature _____

Date _____


June 8, 1998

University of Washington

ABSTRACT

Incorporating Structural Information into
Interpretation of Satellite Images of Forests

by Degui Gu

Chairperson of the Supervisory Committee: Professor Alan R. Gillespie
Department of Geological Sciences

Surface structure plays an important role in controlling the bi-directional distribution function of natural surfaces. Spectral shape, hemispherical reflectance and anisotropic reflectance function all show some degree of dependence on surface roughness. As a result, the observed surface reflection data is not one-to-one correlated to surface composition, and there are generally non-unique interpretations of the observed data. Background knowledge on surface structures is thus important for extracting reliable information from satellite images, particularly for highly structured scenes such as forests.

The key in using spatial information is to understand the various spatial scales involved in satellite remote sensing. Image characteristics change with sensor resolution, and so does the nature of image interpretation. Depending on whether the interesting features are resolved or not, the interpretation of a given image can be either a subpixel-scale inversion problem or a pattern recognition problem. Therefore, the way to use structural information also differs for different problems in satellite image interpretation.

Four models have been developed in this work for a variety of remote-sensing applications. They have explored from different aspects the possibility of using structural information to improve the accuracy of computerized satellite image interpretation. The layered spectral mixture analysis model (LSMA) incorporates the structural information on mixed scenes to analyze the subpixel-scale abundance of interesting features. The SCS model corrects topographic effects in Landsat Thematic Mapper images of forests based on the subpixel-scale sun-canopy-sensor geometry. With the new contextual topographic correction approach, spatial contextual information is used to compensate for light loss on terrain slopes. The multi-scale textural classification (MSTC) algorithm extracts textural features to classify satellite images into unit maps.

Tests on simulated and Landsat Thematic Mapper images of forests suggest that these models have made considerable improvements over the models which are commonly used by the remote-sensing community. It has therefore demonstrated that spatial information is important in satellite image interpretation and deserves more attention.

TABLE OF CONTENTS

LIST OF FIGURES.....	v
LIST OF TABLES.....	xi
LIST OF ABBREVIATIONS.....	xii
INTRODUCTION.....	1
CHAPTER 1: SURFACE STRUCTURE, IMAGE RESOLUTION AND INTERPRETATION OF SATELLITE DATA.....	4
1.1 SIMULATION OF FOREST CANOPIES.....	4
1.2 EFFECTS OF SURFACE STRUCTURE ON ITS REFLECTION.....	8
1.2.1 Spectrum.....	8
1.2.2 Hemispherical reflectance.....	9
1.2.3 Anisotropic reflectance function.....	10
1.3 SCALE EFFECTS ON IMAGE CHARACTERISTICS.....	12
1.4 SCALE EFFECTSON IMAGE INTERPRETATION.....	14
1.5 SUMMARY.....	17
CHAPTER 2: SUBPIXEL-SCALE STRUCTURE AND SPECTRAL MIXTURE ANALYSIS.....	19
2.1 INTRODUCTION.....	19
2.2 SPECTRUM, COMPOSITION AND STRUCTURE OF NATURAL SURFACES.....	20
2.3 LINEAR SPECTRAL MIXTURE MODEL.....	25
2.3.1 SMA model.....	25
2.3.2 Endmember selection.....	26
2.3.3 Shade as an endmember.....	26

2.3.4 Interpretation of endmember fractions.....	26
2.4 LAYERED SPECTRAL MIXTURE MODEL.....	28
2.4.1 Two-layer spectral mixture analysis model.....	28
2.4.2 Endmember spectra.....	29
2.4.3 Intrinsic shade and inter-layer shade.....	30
2.4.4 Advantages of the layered model.....	31
2.4.5 Mixed layers.....	32
2.5 INVERSION OF CANOPY PARAMETERS.....	33
2.5.1 Canopy simulation.....	33
2.5.2 Results of simple spectral mixture analysis.....	35
2.5.3 Results of the layered spectral mixture model.....	37
2.5.4 Non-linear LSMA.....	38
2.6 SUMMARY.....	40
 CHAPTER 3: TOPOGRAPHIC NORMALIZATION OF LANDSAT TM	
IMAGES OF FOREST BASED ON SUBPIXEL-SCALE	
SUN-CANOPY-SENSOR GEOMETRY.....	
	44
3.1 INTRODUCTION	44
3.2 SUN-TERRAIN-SENSOR GEOMETRY CORRECTION MODELS.....	48
3.2.1 Cosine correction model.....	48
3.2.2 C-correction model.....	49
3.2.3 Minnaert correction model.....	50
3.2.4 Other models.....	50
3.3 DERIVATION OF THE SCS TERRAIN CORRECTION MODEL.....	51
3.3.1 Scale of light interaction within a canopy.....	51
3.3.2 Derivation of SCS model.....	52
3.3.3 Comparison with STS models.....	55
3.4 MODEL VERIFICATION WITH SIMULATED FOREST CANOPIES..	55

3.5 MODEL EVALUATION IN THE TEST SITE.....	59
3.5.1 Test site description.....	59
3.5.2 TM image preprocessing.....	60
3.5.3 Statistical evaluation of the SCS model.....	60
3.6 DISCUSSION.....	64
3.7 SUMMARY.....	65
CHAPTER 4: A STATISTICAL APPROACH FOR TOPOGRAPHIC	
CORRECTION OF SATELLITE IMAGES BY USING	
SPATIAL CONTEXT INFORMATION.....	
4.1 INTRODUCTION.....	67
4.2 ERRORS RELATED TO TOPOGRAPHIC CORRECTION.....	69
4.3 CONTEXTUAL TOPOGRAPHIC CORRECTION APPROACH.....	75
4.3.1 Formulation of the contextual approach.....	75
4.3.2 Estimation of $\hat{\rho}_c$	77
4.3.3 Error propagation in the contextual approach.....	79
4.4 APPLICATION RESULTS.....	81
4.4.1 Variance analysis.....	82
4.4.2 Visual examination of the corrected images.....	85
4.4.3 Impacts on classification accuracy.....	86
4.5 DISCUSSION.....	90
4.6 CONCLUSIONS.....	94
CHAPTER 5: A MULTI-SCALE TEXTURAL CLASSIFICATION ALGORITHM	
FOR INTERPRETATION OF SATELLITE IMAGES.....	
5.1 INTRODUCTION.....	96
5.2 CHARACTERISTICS OF SATELLITE IMAGE INTERPRETATION....	98
5.3 MULTI-SCALE TEXTURAL CLASSIFICATION	
(MSTC) ALGORITHM.....	101

5.3.1 Statistical Presentation.....	101
5.3.2 Defining uniform pixel blocks and estimating prior probabilities....	103
5.3.3 Implementation of MSTC.....	105
5.3.4 Interpretation of MSTC.....	107
5.3.5 Comparison with pure contextual/textural approaches.....	109
5.4 TESTS ON SYNTHETIC IMAGES.....	111
5.4.1 Image description.....	111
5.4.2 Evaluation of classification results.....	113
5.4.3 Sensitivity on initialization.....	117
5.5 TESTS ON TM IMAGES OF FORESTS.....	118
5.6 SUMMARY.....	124
CHAPTER 6: SUMMARY.....	126
BIBLIOGRAPHY.....	130

LIST OF FIGURES

<i>Number</i>	<i>Page</i>
Figure 1.1 Radiance leaving a surface element depends on both direct illumination and secondary illumination from nearby surface elements.....	6
Figure 1.2 Surface structure is a factor affecting the shape of reflectance spectrum.....	9
Figure 1.3 The hemispheric reflectance is largely dependent of surface structure. The rougher the surface, the darker it appears.....	10
Figure 1.4 Surface structure is an important factor controlling the directional distribution of reflected radiance. The directionality is stronger when the sun is lower than when it is higher.....	11
Figure 1.5 Low- and high-resolution images of a simulated surface covered with a rough forest canopy and a smooth forest canopy. (a) The ultra-high-resolution image (0.25m) clearly shows the shapes, distributions, and brightness of individual trees. (b) The high-resolution image (1m) shows vague but still detailed structures within the canopies. (c) The low-resolution image (32m) shows strong contrast between the two types of canopies. In (a) and (b) only a portion of the simulated canopy surface is shown.....	12
Figure 1.6 Image characteristics vary with image resolution. Brightness variation in low-resolution images is largely related to the difference in canopy types. In high-resolution images, brightness variation is dominated by the differences in illumination geometry and reflectance between individual canopy elements within each canopy type.....	14

Figure 2.1 Surface structure affects the linearity of spectral mixing. The scene consists of two endmembers, “soil” and “tree.” If the surface is assumed to be unstructured, its spectra (solid circles) can be presented as linear mixtures of the endmember spectra (squares). When surface structure is assumed, the actual spectra (open circles) significantly deviate from the linear spectral mixing line (gray line)23

Figure 2.2 Sketch illustrating the difference between spectral mixing in image and compositional mixing in the scene. (a) Two components are present in the scene, “ball” and “flat layer”. (b) Three image endmembers are shown in the spectral image: “ball,” sunlit “flat layer” and shadowed “flat layer”24

Figure 2.3 Structure and illumination geometry of simulated forest canopy data. Simulation 1: ball-shaped tree crown, sun elevation 30°; Simulation 2: ball-shaped tree crown, sun elevation 60°; Simulation 3: ellipsoid-shaped tree crown, sun elevation 30°; Simulation 3: ellipsoid-shaped tree crown, sun elevation 60°34

Figure 2.4 Endmember spectra used in simulating canopy spectra data. Random noise (20%) is added to account for the spectral variability in natural canopies.....36

Figure 2.5 Correlation between actual and estimated forest canopy coverage. Linear SMA model generally overestimates canopy closure for the simulated canopy data. The prediction errors are larger when the sun is lower (simulations 1 and 3) than higher (simulations 2 and 4)38

Figure 2.6 Correlation between actual and estimated forest canopy coverage. The LSMA model yields much better predictions than the linear SMA model in all simulations. Slight underestimates in the high canopy-closure end are evident for simulation 3, which is related to the

significant structures within the canopy layer.....	39
Figure 2.7 Average reflectance of the canopy layer varies with canopy closure in simulation 3. As canopy closure increases, the amount of shadows within the canopy layer increases and the canopy layer appears darker.....	41
Figure 2.8 The non-linear spectral mixing model slightly improves the accuracy of LSMA. The average prediction error is reduced from 7% in linear LSMA to 5.8% with the non-linear LSMA model.....	15
Figure 3.1 Geometrical presentation of sun-terrain-sensor geometry correction models: (a) forest canopy on the sloped terrain; (b) terrain rotated to horizontal; (c) after light compensation based on photometric functions; and (d) forest canopy on the flat terrain. Notice the sun-canopy-sensor geometry being changed from (a) through (c), and canopy structure in (c) no longer the same as in (d).....	46
Figure 3.2 Geometry of light interaction with canopy on sloped terrain. The incidence angle of solar illumination on the terrain slope differs from the incidence angle on the sunlit part of tree canopy, which determines the irradiance on the sunlit parts of canopies.....	54
Figure 3.3 Radiance from the simulated canopy on various slopes. Radiance is affected not only by the solar incidence angle, but also by the slopes, which are given under each curve.....	57
Figure 3.4 The SCS model fit to the simulated data. Most of the scattering in Figure 3.3 now disappears, indicating that the SCS model predicts terrain effects better than the Lambert model.....	57
Figure 3.5 Applicability of the SCS model to surfaces with various degrees of canopy closure. The SCS model is more appropriate than the Lambert model for canopies of 50% or higher canopy-closure, and the Lambert	

model is good only when the canopy-closure is lower than 50%.....	58
Figure 3.6 Scatter plots of TM band 5 normalized radiance vs. cosine of the solar incidence angle. (a) 8 October 1990 image; (b) 9 July 1992 image.....	61
Figure 4.1 Scatter plot of radiance-geometry for a conifer stand (consisting of 3488 TM pixels). Notice the amount of scatter in this diagram is about the same for all slopes.....	70
Figure 4.2 Standard deviations of TM bands 3, 4 and 5 radiance for the conifer stand on various slopes. Larger standard deviation corresponds to greater scatter on radiance-geometry diagram. Scatter is greater in band 4 than in band 5 and 3, but is not strongly correlated to topography.....	74
Figure 4.3 Correlation of the standard deviations in bands 3, 4 and 5 radiance. The strong correlation of standard deviations in different bands confirms that the scatter in these bands are more correlated to each other than to topography.....	74
Figure 4.4 Spatial context of a pixel. Shown is a 5x5 square neighborhood of the center pixel (shaded). All the pixels in the square together consist of the spatial context of the center pixel. The size and shape of the spatial context of a pixel can be chosen according to image resolution, scene complexity, and data quality in practice.....	76
Figure 4.5 The estimated band 4 reflectance distributions for the same conifer stand as in Figure 4.1. The reflectance estimated with the conventional approach (gray solid circles) shows much more scatter than with the contextual approach (black solid circles).....	83
Figure 4.6 Comparison of the variability of reflectance estimated with different methods. The contextual approach produces more uniform reflectance estimates over various slopes, but the conventional approach causes much larger variability on shaded slopes than on sun-facing slopes, for	

all three tested photometric functions.	83
Figure 4.7 Band 5 TM images of the test site. (a) uncorrected; (b) conventionally corrected; (c) contextually corrected and (d) spatially filtered version of image (b). The image is 240×170 pixels.	85
Figure 4.8 Spectral clusters of the four classes identified in the test site on uncorrected (a), conventionally corrected (b), and contextually corrected (c) images, respectively. Overlaps between different clusters are decreasing from (a) to (b) to (c).....	89
Figure 4.9 Classification accuracy improvements on the contextually corrected images. Classification accuracy was improved in conventionally corrected images in comparison to the uncorrected image, with similar magnitudes when using three different photometric functions. But the best classification was achieved in the contextually corrected image, yielding highest accuracy for all classes.....	91
Figure 5.1 Sketch to show how spectral context information is defined in MSTC. The pixel (shaded) to be considered is put into pixel blocks that represent possible unit partitions at its location. The pixel blocks are then evaluated based on their spectra to find which of them is most likely a true unit.....	106
Figure 5.2 Probability distribution in a uniform pixel block (a) and a mixed pixel block (b). Notice in (b) that the probability distributions of individual pixels have different peaks corresponding to their true memberships...	110
Figure 5.3 The synthetic testing image (a) and the truth map that generates it (b)....	112
Figure 5.4 Classification maps produced by the MLC (a), the ICM (b), and the MSTC (c), respectively.....	114
Figure 5.5 Classification accuracy of the MLC (squares), the ICM (triangles) and the MSTC (circles).....	115

Figure 5.6 Distribution of misclassified pixels on classification maps produced by ICM (a) and MSTC (b). The misclassified pixels are highlighted (bright) against the correctly classified pixels (dark).....	116
Figure 5.7 Classification maps produced by the ICM with different initializations. (a) uniform prior probability, (b) random prior probability and (c) single-color prior probability. The great differences between these maps indicate ICM's very sensitive dependence of the initialization....	116
Figure 5.8 Probability distribution of the MSTC classification map. Lower probabilities (darker) characterize unit boundaries and indicate the uncertainties in the classification map.....	118
Figure 5.9 Pseudo-color TM image of the Bluff Creek, Six Rivers National Forest, California. Bands 3, 4 and 5 are displayed as blue, green and red, respectively.....	119
Figure 5.10 TM band 4 and 5 spectral contrasts between different land cover types defined in the testing image. Water has very distinct spectra, but there are overlaps between other classes.....	120
Figure 5.11 Classification map of the testing TM image produced by MLC.....	122
Figure 5.12 Classification map of the testing TM image produced by MSTC.....	123

LIST OF TABLES

<i>Number</i>	<i>Page</i>
Table 2.1 Accuracy of canopy closure estimated with SMA and LSMA.....	37
Table 3.1 Symbols used in terrain correction models.....	49
Table 3.2 Tree parameters of the simulated forest canopies.....	56
Table 3.3 Performance of terrain correction models on the test site.....	62
Table 4.1 Normalized standard deviation of the estimated reflectance for a conifer stand in the test site.....	84
Table 4.2a Classification accuracy in uncorrected image.....	88
Table 4.2b Classification accuracy in conventionally corrected image.....	88
Table 4.2c Classification accuracy in contextually corrected image.....	88
Table 5.1 Features of classes in the synthetic image.....	112
Table 5.2 Classification accuracy of different classifiers in the synthetic image.....	114
Table 5.3 Classification accuracy in the TM image by MLC and MSTC.....	121

LIST OF ABBREVIATIONS

BRDF: Bi-directional Reflectance Distribution Function;
DEM: Digital Elevation Model;
ICM: Iterative Conditional Modes;
IFOV: Instantaneous Field of View;
LSMA: Layered Spectral Mixture Analysis;
MLC: Maximum Likelihood Classifier;
MRF: Markov Random Field;
MSTC: Multi-Scale Textural Classification;
NDVI: Normalized Difference Vegetation Index;
RMS: Root-Mean-Squared;
SCS: Sun-Canopy-Sensor;
SMA: Spectral Mixture Analysis;
STS: Sun-Terrain-Sensor;
TM: Thematic Mapper.

ACKNOWLEDGMENT

I am very grateful to all the supervisory committee members, Dr. Alan Gillespie, Dr. John Adams, Dr. Stewart Smith, Dr. Thomas Hinckley, Dr. Stephen Warren, and Dr. James Bardeen. It is their guidance and encouragement that have led me pass this milestone in my life. Their patience and kindness have made my journey much more enjoyable than it is supposed to be. Alan, John, Steve and Tom have made, in addition to correcting spelling and grammar mistakes in my manuscript, invaluable comments and suggestions which make this dissertation a much better piece of work than the very first version.

I am particularly in debt to Alan, who has given me both the academic freedom and provided the financial support, which together I believe to be a great fortune. With the freedom, I can focus on the problems which mostly interest me, whereas the financial support enables me to sustain my family when I am having fun in my research. His knowledge and expertise in and beyond remote sensing have kept me from becoming lost when I am digging the hole deeper and deeper.

I will remember Stewart for his encouragement and trust that he had shown me in my first two years at the University of Washington. I thank John for bringing me over to this fascinating problem when I was frustrated to find a suitable topic for my research. I appreciate Tom for his coffee and tree talks. Their concern and help about myself and my family have made a huge difference, and will always be remembered.

My fellow remote sensors in the remote sensing laboratory, Wen-Hao Li, Ginger Vogler, Gill Yamada, Robin Weeks, Steven Cothorn, Bill Gustafson, Kyle Bland, Milton Smith, Don Sabol and Steve Thompson, are just wonderful people with whom you want to work. Thanks are due to them for making the lab such a great working environment.

Finally, I would like to give my thanks to my family and friends. Particularly, the love from my wife, Wei, and my daughter, Stella, always takes the tiredness away from me and recharges me with fresh spirit and energy. Mr. Warren Mason has led me to know what is the most important in a person's life, and thanks to him and his family have been overdue for years.

This research, in a large part, was supported by NASA Contracts 5-31372 (EOS/ASTER).

INTRODUCTION

Remote-sensing data have become an important information source for scientific studies on a variety of geological and environmental problems. The capacity of large geographic coverage and repetitive measurement gives remote-sensing technology great advantages, particularly in regional- and continental-scale studies related to climate change, biodiversity, natural resource management and environmental monitoring.

Remote-sensing application is essentially the inversion of geophysical parameters from the measured images. In contrast to forward problems, inversion problems are in nature usually underdetermined, and there are usually more than one set of solutions. This is especially true regarding the interpretation of satellite images. The interaction of light with the atmosphere and natural surfaces is a complicated process which can not be modeled in an exact manner based on theories of electromagnetic wave propagation. Even with simplified atmospheric models that directly relate the radiance measured at the satellite to the reflectivity of the ground, the inferred surface composition may still be ambiguous. As we collect more ground information and understand more about this process, however, we can put more constraints on the inversion problem to get solutions closer to the truth. For this purpose, the interpretation of satellite data requires not only understanding the interaction of light with surface structures, but also certain background knowledge about the scene. The appropriate techniques should incorporate all available information to constrain the interpretation of satellite images. Because the spatial and spectral resolutions of satellite images are limited, the choice of interpretation techniques is critical to the successful extraction of the desired physical information about the scene. For this reason, we need to investigate which factors make the most

important contributions to spectral images of various types of natural surfaces, and develop corresponding image interpretation techniques.

It has been well understood that the spectrum of a surface largely depends on its biogeochemical composition, because different materials absorb and reflect electromagnetic energy differently. Absorption and reflection commonly vary with wavelength, so that different scene components may be characterized by distinct reflectance spectra. A large amount of information about the spectral properties of natural materials has been collected through laboratory and field measurements, and forms the basis for interpreting satellite images.

Besides composition, surface structure is another important factor controlling scene reflectance. A bulk sample of a particular mineral may look different in color and brightness simply due to variation in grain size. Both numerical simulations and field observations have confirmed that structure is the most important factor controlling the directional variability in reflection of many vegetated surfaces, such as forest and crop canopies. Even though the significance of surface structures has been recognized for years, however, such information has not been used effectively used in many, perhaps most, studies involving applied remote sensing. This may help explain why quantitative remote-sensing interpretations have been difficult to extend beyond local training areas, especially in the study of highly structured scenes, such as forest canopies in rugged terrain.

Unlike composition, structural characteristics of a surface are scale-dependent. Consequently, the structural effects on satellite measurements may largely depend on the spatial resolution of the observational system. Large-scale structures that can be resolved on satellite images clearly provide useful information from their shape and context, in addition to spectral data, for identifying or differentiating various scene features. Small-scale structures that cannot be resolved, however, are invisible in measured images. Nevertheless, for image interpretation it is still necessary to consider

the unresolved, or subpixel-scale, surface structures because they have a strong influence on the observed spectral variation, especially the overall reflectance. Therefore, scale is an important factor to be considered in satellite image interpretation.

This research is focused on understanding structural effects on satellite measurements and developing methods to incorporate such knowledge into image interpretation. I have acquired Landsat Thematic Mapper images of forests to examine these ideas and to test the new methods. The complex canopy structure of forests fits the research interests well. In addition, forest ecosystems have been an important subject of remote-sensing studies. Therefore, the principles and algorithms developed here have significance for remote -sensing applications. Moreover, they are generally applicable to other structured surfaces with no or slight modifications. The work presented here includes:

1. understanding surface structure as a key parameter affecting surface reflection;
2. constructing a photometric function for forest canopies, based on subpixel-scale canopy structures;
3. understanding and constraining spectral mixture analysis for structured scenes;
4. using spatial contextual information in geometric normalization of satellite data; and
5. using spatial textural information in the classification of satellite images.

The goal of these studies is to establish the significance of incorporating structural information in understanding and interpretation of satellite images.

CHAPTER 1: SURFACE STRUCTURE, IMAGE RESOLUTION AND INTERPRETATION OF SATELLITE DATA

In this chapter, the structural effects on surface reflection and principles for interpreting images of structured surfaces will be discussed. Variations in spectral shape, reflectance, and directionality of forest canopies as functions of canopy structures will be addressed first, followed by a discussion of image characteristics at various scales of observation. Finally, the principles used to incorporate structural information into image interpretation will be examined.

1.1 SIMULATION OF FOREST CANOPIES

Because sufficient field data were not available, the structural effects on surface reflection were investigated here with computer-simulated data. The simulated data were generated from computer models of forest canopies which accounted for variability in tree shape, density, height and reflectance. These parameters were specified based on field observations.

The mesh surfaces of the simulated canopies were constructed with a ground resolution of 0.25m. This chosen resolution is arbitrary, even though there are some practical reasons as discussed later. For each surface element, its normal vector and area were estimated from the four corners constraining it. The position of the sun (illumination source) is at infinity and is specified by its elevation angle while its azimuth is taken to be constant for the purpose of the simulation.

The radiosity model (e.g., Li, 1997; Borel et al., 1991) was then employed to model the process of light interaction within the canopy, which was assumed to be Lambertian at the scale of the mesh. The radiosity, or radiant exitance, is defined as the total energy per unit area that leaves a surface. As a result of the Lambertian

assumption, the radiosity from any element is simply the product of irradiance and its reflectance, and the radiance is the radiosity divided by π . Because the irradiance on any one of the elements, say, the i th element, consists of the direct irradiance from the sun and the indirect irradiance from other elements of the surface (Fig. 1.1), the radiosity from this element, B_i , is

$$B_i = \rho_i (E_i + \sum_{j=1}^N F_{ij} B_j) \quad (1.1)$$

where ρ_i is the reflectance of the element, E_i is the direct irradiance, the ‘‘form factor’’ F_{ij} measures the relative distance and geometry between elements i and j , and N is the total number of surface elements. As a first-order approximation,

$$F_{ij} = \begin{cases} \frac{A_j \langle \bar{n}_i \cdot \bar{r}_{ij} \rangle \langle \bar{n}_j \cdot \bar{r}_{ij} \rangle}{\pi |\bar{r}_{ij}|^4} & \text{if } \bar{n}_i \cdot \bar{r}_{ij} > 0, \bar{n}_j \cdot \bar{r}_{ij} > 0 \\ 0 & \text{otherwise} \end{cases} \quad (1.2)$$

where A_j is the area of element j , \bar{r}_{ij} represents the direction and distance from element i to element j , and \bar{n}_i and \bar{n}_j are the normal of elements i and j respectively.

Once the form factors are estimated, the linear system can be solved by standard methods (Borel et al., 1991). The iterative approach is adopted here to solve the problem since the multiple bouncing between elements is weak in intensity relative to the direct illumination. In practice, it is found that convergence is fast and the solution becomes stable after usually less than 5 iterations.

The total radiance from the structured surface at viewing direction \bar{n}_v , $L(\bar{n}_v)$, is the sum of the radiosity at individual elements weighted by their areas and orientations relative to the sensor,

$$L(\bar{n}_v) = \sum_{i=1}^N \frac{B_i A_i \max\{0, \langle \bar{n}_i \cdot \bar{n}_v \rangle\}}{\pi} \quad (1.3)$$

where $\langle \bar{n}_i \cdot \bar{n}_v \rangle$ is the inner product of \bar{n}_i and \bar{n}_v . The radiance may be normalized by the mean radiance to get the anisotropic reflectance function, χ ,

$$\chi(\bar{n}_v) = L(\bar{n}_v) / \bar{L}, \quad (1.4)$$

where \bar{L} represents the mean radiance averaged over all directions. The anisotropic reflectance function is similar to BRDF, bidirectional reflectance distribution function, and describes the directional distribution of reflected radiance (e.g., Taylor and Stowe, 1984 a, b). If a surface is Lambertian, $\chi=1$, independent of illumination and viewing geometry.

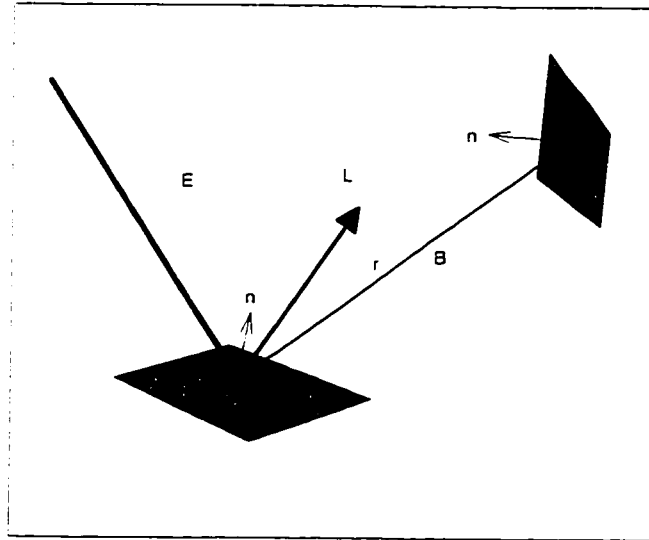


Figure 1.1 Radiance leaving a surface element depends on both direct illumination and secondary illumination from nearby surface elements.

Another important parameter, the hemispherical reflectance (ρ), is defined as the ratio of the integral of the outward radiance in all directions to the total incident irradiance, i.e.,

$$\rho = \sum_{\bar{n}_v} L(\bar{n}_v) \langle \bar{n}_v \cdot \bar{z} \rangle / \sum_i E_i, \quad (1.5)$$

where \bar{z} is the unit vector representing the zenith.

It should be pointed out that individual surface elements have been treated as infinitesimal elements to estimate the form factors in equation (1.2), although they actually have finite areas. There are several reasons for making such simplifications instead of using more complicated approaches. First, it greatly reduces the amount of computation (Li, 1997). Second, the Lambertian assumption can be badly violated at small scales. For example, the forest canopy may be treated as Lambertian at scales of trees or branches, but may not be so at scales of leaves where specular reflection is a large component of the total reflection. Third, vegetated surfaces are not solid: i.e., there are holes and gaps within vegetation canopies, and it is less meaningful to represent them with smooth surface elements at smaller scales than at larger scales. The last two reasons have prevented one from dividing the surface into infinitely small elements and are major concerns in determining the element scale. Finally, computer simulations can give one some quantitative insights about the reflection of natural surfaces, but the variation in structure and composition of actual scenes prevents such results from being predictive for specific cases.

The simulation results, however, do appear to be consistent with the field data (e.g., Deering et al., 1994; Ranson et al., 1994) in a qualitative sense. They are thus useful in investigating the general characteristics of the interaction of light with structurally complicated surfaces. Therefore, the simulated data are used here to demonstrate the effects of canopy structure on the reflectance spectrum, hemispheric reflectance and anisotropic reflectance function of forest canopies.

1.2 EFFECTS OF SURFACE STRUCTURE ON ITS REFLECTION

1.2.1 Spectrum

The structure of simulated canopies has an impact on their reflectance spectra. Six spectral bands in visible, near infrared (NIR) and short wave infrared (SWIR) range were chosen to simulate the Landsat Thematic Mapper (TM) data. The reflectance spectra of the tree crown and substrate are taken to mimic those of green vegetation and soil, respectively. Canopy structures in the model were altered by varying the ratio of the vertical diameter, a , to the horizontal diameter, b , of the ellipsoid-shaped tree crowns. The larger ratios correspond to rougher canopies. The packing density was not changed.

The modeling results (Fig. 1.2) demonstrate that reflectance spectra of the simulated canopies depend on canopy structures, particularly in NIR (TM 4) and SWIR (TM-5) bands. As the canopy roughness changes, the illumination geometry on individual canopy elements changes, too. Since the overall spectrum of the canopy is a mixture of the spectra of the tree crowns and the substrate, it changes according to the shadowing and shading pattern within the canopy.

The computer simulations have not taken account the light interaction with individual tree leaves. Reflection and transmission of light at the scales of tree leaves lead to volume scattering, which may results significant spectral variations (e.g., Roberts et al., 1990).

However, careful examination of the results shows that there is no predictable correlation between canopy structure and its spectrum. It is largely because other factors, such as tree species, leaf and tree ages, water content, also have a considerable influence (Koch et al., 1990). It is clear, however, that the canopy spectrum is to some degree dependent on canopy structure. This result has important implications for spectral mixture analysis, widely used as a tool to study subpixel-scale features (e.g., Smith et al., 1990; Adams et al., 1989; Sabol et al., 1992).

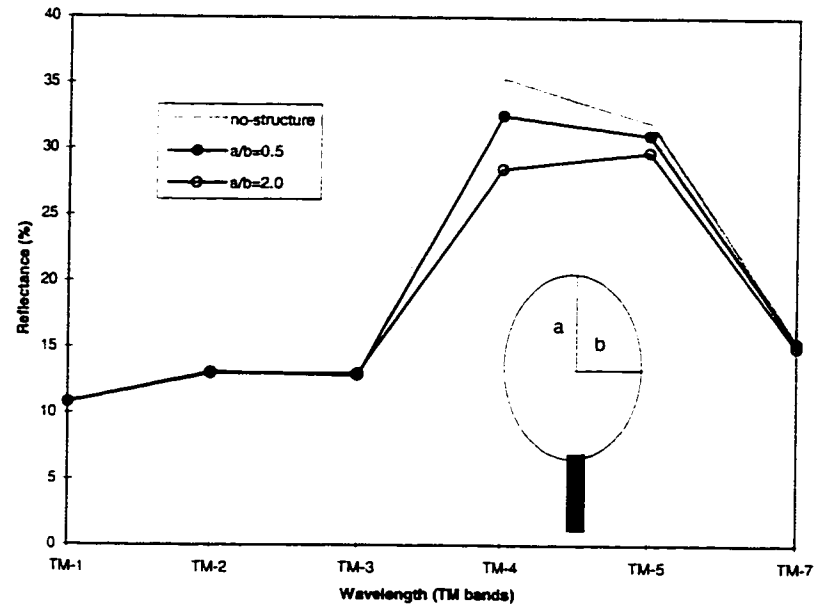


Figure 1.2 Surface structure is a factor affecting the shape of reflectance spectrum.

1.2.2 Hemispherical reflectance

There is an obvious correlation between hemispheric reflectance and canopy roughness (Fig. 1.3). This correlation is related to the change of shading and shadowing patterns within the canopy. As the shape of tree crowns changes, the local incidence angles at sunlit canopy elements change also, and so do the amount and pattern of shadows within the canopy. Consequently, the apparent brightness of the canopy changes. Specifically for the simulated canopies, the hemispheric reflectance decreases when the canopy gets rougher (Fig. 1.3). This is generally true for opaque materials, since a portion of the reflected light is trapped by the rough surfaces (Stephen Warren, pers. Comm., 1998). The correlation between surface roughness and reflectance has motivated studies on the estimation of surface roughness information from satellite images (Weeks et al., 1996, 1997; Shoshany, 1993).

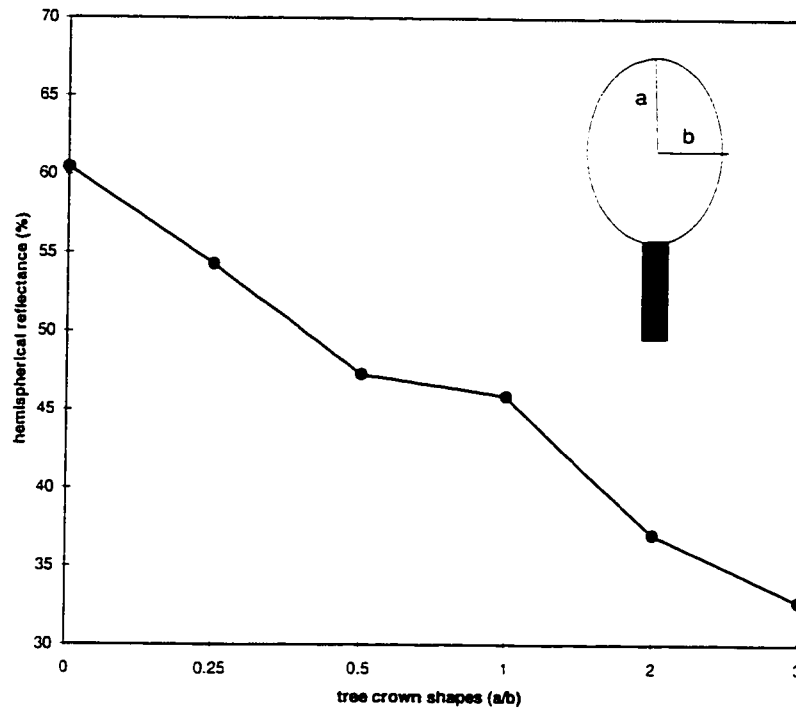


Figure 1.3 The hemispheric reflectance is largely dependent of surface structure. The rougher the surface, the darker it appears.

1.2.3 Anisotropic reflectance function

The anisotropic reflectance functions estimated for a simulated canopy surface are shown in Figure 1.4. The large variation of reflectance with both viewing and illumination angles indicates that the canopy surface is not Lambertian at all. Specifically, the reflection is stronger backward than forward, and the lower the sun, the stronger the directionality. Particularly, the peak reflectances happen around the sun directions. Since the canopy elements themselves are assumed to be Lambertian, the structure of the elements to form the canopy is the only factor accounting for the directional reflection. Indeed, the above results are not surprising but expected, as explained below, due to subpixel-scale canopy structures.

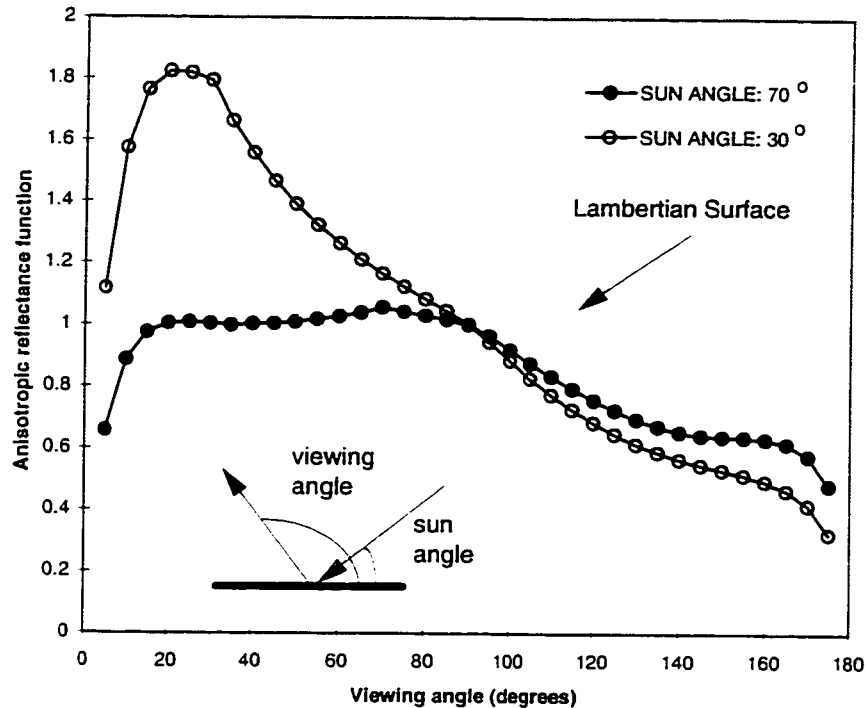


Figure 1.4 Surface structure is an important factor controlling the directional distribution of reflected radiance. The directionality is stronger when the sun is lower than when it is higher.

When observing from the same side of the sun (viewing angle $< 90^\circ$), more illuminated canopy elements will fill the sensor's instantaneous field of view (IFOV) and thus the canopy will appear lighter. However, when observing from the other side (viewing angle $> 90^\circ$), more shadows are present in the sensor's IFOV and cause the canopy to appear darker. The reflectance peaks are consistent with the observed "hot spots" for forest canopies and are directly related to the tree crown shapes (e.g., Deering et al., 1994).

For the same canopy, the sun at a lower elevation angle casts more shadows within the canopy than at a higher elevation angle. Since a larger amount of shadows corresponds to a rougher surface (Shoshany, 1993), the canopy appears "rougher" to

the sun at a lower elevation than at a higher elevation angle. Because canopy elements are assumed Lambertian, the smoother canopy results in more Lambertian reflection. Therefore, the reflection off the canopy is more uniform when the sun is at the higher elevation angle.

1.3 SCALE EFFECTS ON IMAGE CHARACTERISTICS

The structures of natural surfaces are usually linked with various spatial scales (e.g., Milne, 1992; Townshend and Justice, 1992, 1990; Hall et al., 1991). In the example of a forested surface, distinct spatial scales are related to stands, trees, branches, leaves, and so on. When the scale of observation (image spatial resolution) changes, very often we will observe different features even on the same surface (e.g., Happanen, 1996; Marceau et al., 1994; Woodcock and Strahler, 1987). Figure 1.5 shows three simulated images of a forested surface consisting of two types of canopies, one smoother ($a/b=0.5$) and the other rougher ($a/b=2$). The resolutions of these images are 0.25m (Fig. 1.5a), 1m (Fig. 1.5b) and 32 m (Fig1.5c), respectively.

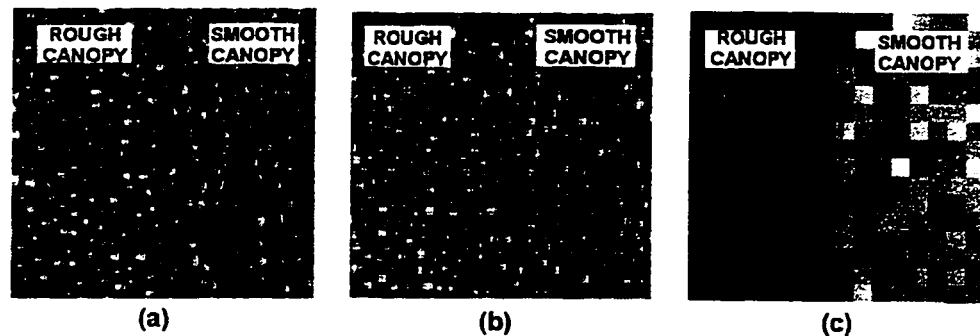


Figure 1.5 Low- and high-resolution images of a simulated surface covered with a rough forest canopy and a smooth forest canopy. (a) The ultra-high-resolution image (0.25m) clearly shows the shapes, distributions, and brightness of individual trees. (b) The high-resolution image (1m) shows vague but still detailed structures within the canopies. (c) The low-resolution image (32m) shows strong contrast between the two types of canopies. In (a) and (b) only a portion of the simulated canopy surface is shown.

Fig. 1.5a reveals detailed structures of canopies. It may immediately be interpreted by viewers as two type of canopies, composed of different type of trees with distinct shapes and reflectances.

For the low-resolution image (Fig. 1.5c), it is clear that there are two distinctive features in the image, one lighter (corresponding to the smoother canopy) and the other darker (corresponding to the rougher canopy). Other than that, the image does not explicitly reveal any information on the structure within each canopy. In this situation, we have to invert the observed spectra to find such information. This inversion may or may not work, depending on how much knowledge we have and how many constraints we can put on the possible solutions to the problem.

In contrast, the high-resolution image (Fig. 1.5b) reveals much more variability of the scene. The dominant feature in this image is no longer the distinct difference in brightness between the two canopy types. Instead, the image reveals some information on the size, reflectance, and shape of individual trees within each canopy. The highest contrast is now related to variations in illumination geometry, which cause highlights and shadows on individual trees and the substrate, rather than to variations in canopy type. Apparently, the brightness variations in this image are not directly useful for the purpose of mapping canopy types.

Figure 1.6 quantitatively describes the dramatic change in image characteristics with image resolution for this simulated scene. In this figure, the within-class variability is defined as the variance of brightness for each canopy type, while the inter-class variability is the variance of average brightness of individual canopies. Similarly, the total variability of the image is defined as the total variance of the brightness over the whole image. The within-class and inter-class variabilities are calculated for each image and then their ratios to the total variability of the corresponding images are plotted as a function of image resolution. Consistent with the above qualitative discussion, as the resolution increases, the within-class variability becomes dominant but the inter-class variability rapidly decreases. Since

the inter-class variability is an indicator of scene separability, its decrease with increasing resolution simply means that the two canopies are getting more and more difficult to differentiate. In particular, the canopies are spectrally almost unseparable at very high resolution ($\leq 4\text{m}$). In low-resolution images ($\geq 8\text{m}$), on the other hand, the inter-class variance dominates and two spectral classes are clearly defined, corresponding to the rough and smooth canopies.

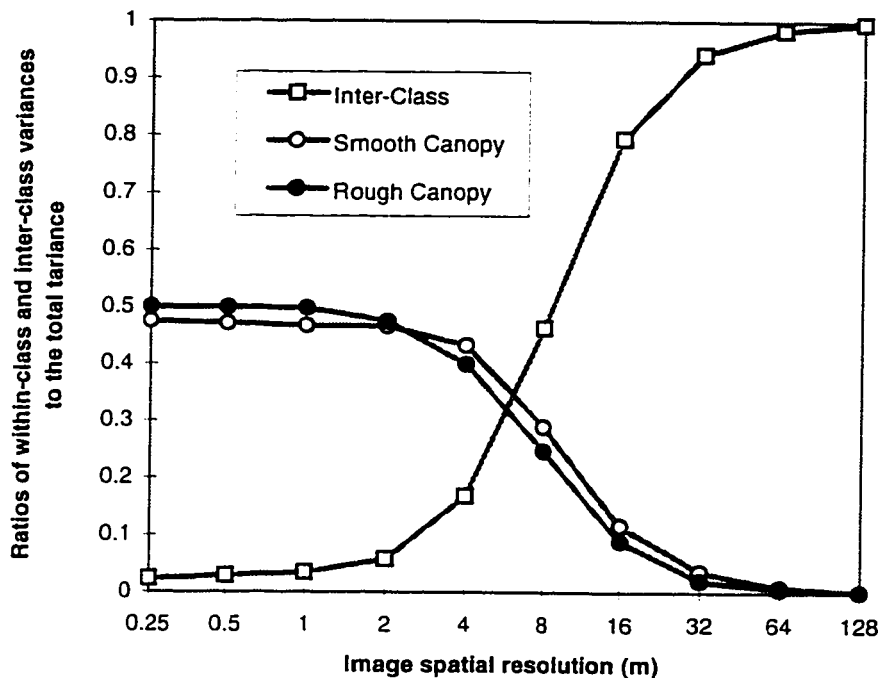


Figure 1.6 Image characteristics vary with image resolution. Brightness variation in low-resolution images is largely related to the difference in canopy types. In high resolution images, brightness variation is dominated by the differences in illumination geometry and reflectance between individual canopy elements within each canopy type.

1.4 SCALE EFFECTS ON IMAGE INTERPRETATION

Due to the resolution dependency of image characteristics discussed in the previous section, which itself is associated to the inherent surface structures, the

interpretation of satellite images needs to be rooted on the knowledge about surface structure and its effects on satellite measurements. Depending on the image resolution, surface structures may or may not be resolved in satellite measurements. Nevertheless, these structures at different scales, resolved or not, will affect satellite measurements. Therefore, it is expected that the knowledge about surface structures will improve the reliability of extracted information about ground features.

For example, the resolved surface structures provide important information, in addition to the spectral variability, to characterize different types of surfaces. The textures, or spatial patterns of brightness/color variation, associated to these structures can be extracted from the images and used to improve the accuracy of image classification (e.g., Nel et al., 1994; Lee and Philpot, 1991; Stromberg and Farr, 1986; Irons and Petersen, 1981). Even in case without obvious patterns, the spatial continuity of large scale structures also provides powerful constraints on image interpretation. Contextual image classification algorithms, which usually use statistical models to simulate the local spatial correlation within individual scene components, have proven helpful in many remote-sensing applications, including forest mapping, cloud mapping, and land-cover and land-use classification (e.g., Moffet and Besag, 1996; Kittler and Pairman, 1985; Zenzo et al., 1987).

The importance of using the structural information in this way is illustrated in Figure 1.6. Although the high-resolution canopy images contain more information than the low-resolution images, the canopies are not spectrally differentiable. Instead, their differences are revealed in other forms, in this case the high within-class variability due to resolved canopy structures at the tree scale. Careful examination of Figure 1.5b shows that shadows and highlights within the smooth canopy are very different in both distribution and amount from those within the rough canopy. Such differences are directly related to the characteristics of the canopy structures. For these high-resolution images, the spatial information is not only useful, but critical in both characterization

and differentiation of the canopies. Of course, we need to have appropriate algorithms to extract and use such textural information.

The unresolved structures also provide important information for understanding and interpreting satellite images. As mentioned above, the interpretation of satellite images is fundamentally an inversion problem and prone to instability and non-uniqueness. The background knowledge about the possible structures in the scene helps to constrain the solutions. For example, surface structures cause mutual shadowing within the surface and cause it appear to be darker (Fig. 1.3). Topography causes shading and also makes the surface darker. However, the effect of structural shadowing is different from that of topographic shading in that the former is dependent of viewing direction (Fig. 1.4) but the latter is not. Therefore, the topographic effects, as the combined results of structural shadowing and topographic shading, should be corrected based on the knowledge about surface structures (e.g., Gu and Gillespie, 1998; Hugli and Feri, 1983).

One of the key issues regarding to the interpretation of satellite images of structured surfaces is the relation between the scale of measurement and the scale of features of interest (e.g., Pax-Lenney and Woodcock, 1997; Happanen, 1996; Marceau et al., 1994; Woodcock and Strahler, 1987; Markham and Townshend, 1981). The former determines what will, and what will not, be resolved, and thus affects the characteristics of the spectral images. The latter, on the other hand, determines the information we need to extract from the measurements. These two scales basically have determined the nature of the interpretation of a specific image: either to identify large, resolved features (image classification), or to discover the abundance of small, unresolved features (sub-pixel scale analysis). In either case, we need information on surface structure in order to achieve a better understanding and interpretation. Specifically, the knowledge on subpixel-scale structures is useful in interpreting the observed reflectance spectra, and the knowledge on large-scale structures provides extra constraints in inverting the measurements into geophysical parameters.

1.5 SUMMARY

We have seen that surface structure plays an important role in the satellite measurements of surface reflectance. Interpretation of satellite images should therefore be based on generalized background knowledge about surface structures on the ground.

Scale-dependency of surface structures and image characteristics adds difficulties in incorporating such knowledge into image interpretation. There are at least four scales involved in satellite image observation and interpretation:

1. scale of the scene, which characterizes structures of a surface;
2. scale of the interaction, at which light interacts with a surface;
3. scale of the interest, which determines the scale of extracted information;
4. scale of the image, which determines image characteristics.

The first two scales are independent of observation and interpretation, but provide the fundamental background knowledge required to interpret satellite images. The last two scales are particularly important in implementing image interpretation algorithms. If the scale of interest is smaller than image resolution, the spectral images need to be inverted to identify the unseeable subpixel-scale features on the ground (unmixing). On the other hand, if the scale of interest is larger than image resolution, the task is to study the pattern of spatial correlation in the image in order to identify the resolved features on the ground (feature extraction).

In the following chapters, I will examine several practical remote-sensing applications in which we may test the image interpretation principles rooted in spatial scales. I will study the impacts of subpixel-scale canopy structures on understanding and thus interpreting forest images. Spatial continuity in high-resolution images is also used as a constraint to improve image processing accuracy. Specifically, a multi-layer spectral mixture model (Chapter 2) is developed to incorporate canopy structural information for the extraction of subpixel compositional information and for the

inversion of canopy closure parameters. Based on the characteristic structure of forest canopies, a photometric function is constructed for correction of topographic effects in forest images (Chapter 3). In Chapter 4, I present a contextual topographic correction approach based on spatial continuity in high-resolution images. In Chapter 5 is a multi-scale textual classification algorithm suitable for classifying high-resolution satellite images. These case studies are chosen to increase our understanding of the problems related to spatial scales in image analysis, thereby increasing the applicability of remote-sensing data to solve practical problems.

CHAPTER 2: SUBPIXEL-SCALE STRUCTURES AND SPECTRAL MIXTURE ANALYSIS

2.1 INTRODUCTION

Spectral mixture analysis (SMA) models have been widely applied to analyze the subpixel-scale composition, target identification and image classification. For example, Smith et al. (1990) applied SMA to Landsat TM images to study vegetation abundance in semiarid Owens Valley, California. Gillespie (1992) applied SMA to thermal infrared images for geological mapping of Death Valley. Adams et al. (1995) used SMA to classify forest communities in Amazon Basin.

Although it has been successful in general, SMA has some drawbacks which has limited its applications. One of them is related to the interpretation of SMA results, i.e., the endmember fractions, particularly the “shade” endmember (Smith et al., 1990). Although topographic shading and structural shadowing occurs at all scales within a pixel, shade itself is NOT a compositional member in the scene; that is, shade is not an intrinsic property of the scene, but depends on and varies with extrinsic factors such as the illumination and viewing directions. When the interest is on scene composition, such as in soil, rock or green vegetation mapping, the shade endmember fraction needs to be partitioned among other compositional endmembers in order to estimate their actual abundance in the scene (e.g., Smith et al., 1990). There are difficulties in doing this because the distribution of shade evidently depends on scene structure, illumination conditions and image resolution.

Another often-encountered problem with SMA is that observed spectra sometimes deviate significantly from linear mixtures of endmember spectra (e.g., Sabol et al., 1992; Mustard and Pieters, 1987; Johnson et al., 1983; Hapke, 1981). Due to the difficulties in solving non-linear mixing problems, non-linear models are rarely used in SMA. To employ linear SMA, either by “linearization” (e.g., Johnson et al.,

1983) or simply neglecting the non-linearity, will cause large root-mean-squared (RMS) errors, which may also be a result of the incompleteness of endmember spectra (Roberts et al., 1990; Gillespie et al., 1990). Therefore, the non-linearity of spectral mixing causes ambiguity in interpretation of residual images.

What has been overlooked sometimes in spectral mixture analysis is the structure of natural surfaces, which has proved to have a strong influence on surface reflectance. Therefore, this chapter will focus on the impacts of surface structure on spectral mixing, and develop a model to incorporate structural information into spectral mixture analysis to estimate the abundance and distribution of subpixel-scale scene components.

2.2 SPECTRUM, COMPOSITION AND STRUCTURE OF NATURAL SURFACE

The basic assumption in SMA is that a small number of materials or components, of different reflectance spectra, mix in different proportions to cause the majority of the spectral variation in multispectral images of natural scenes (e.g., Adams et al., 1986; Smith et al. 1990). These components or materials are called endmembers. Whether the spectral mixing model is appropriate to describe the actual mixing in the scene is usually evaluated by examining the model's fit to the observed spectra (e.g., Adams et al., 1989; Gillespie et al., 1990).

Fundamentally, there are two types of mixing: spectral and compositional. In spectral mixing, the spectra of the endmembers are mixed to produce the observed spectra, whereas in compositional mixing, the actual scene is a mixture of different materials. With SMA, one expects to extract quantitative information on the composition of the scene through unmixing the observed spectra. Such a scenario does not always work, or work equally well in different circumstances, however, because the observed spectra are not always highly correlated with the composition of the scene. As an example, an open-canopy forest may appear to be significantly different in brightness when the sun is at different elevations even after photometric shading is

corrected (Fig. 1.3). As discussed in Chapter 1, this results from the changes of the shadowing pattern within the canopy with the sun position, rather than from any changes in the canopy composition itself. Besides composition, scene structure also has a strong, even dominant, effect on reflectance. This conclusion is supported by laboratory and field measurements (e.g., Gong et al., 1997; Roberts et al., 1990). Consequently, compositionally identical mixtures may produce different spectra, and compositionally different mixtures may produce exactly the same spectrum, simply due to structural variations. Therefore, we need to know the surface structure in order to relate the spectral mixing to the compositional mixing, which is the interest of most SMA applications.

Even the endmembers themselves are not uniquely definable. Since natural surfaces are mixed continuously from micro- to macro-scale, they can be viewed as mixtures of a certain set of endmembers at one scale, yet another set of endmembers at another scale (Adams et al., 1993). Therefore, the observed spectra can be modeled equally well as the spectral mixtures of a number of sets of endmembers. Selecting image endmembers, which is usually based on field observation, is thus an important step in SMA. Ideally, the endmembers should be chosen to reflect both the compositional and structural characteristics because they together have determined the spectra in the actual scene.

It is well known that back scattering, multiple scattering, volume scattering, shading and shadowing are largely related to the scene structures at all scales (e.g., Li, 1997; Gong et al., 1997; Roberts et al., 1990; Hapke, 1981). These structural effects have altered the spectrum and directionality of the illumination, and thus changed the reflected radiance, for individual scene components. As a direct consequence, the observed scene spectrum is not linearly mixed from the endmember spectra, and the non-linearity is dependent on the structural complexity of the scene. If the endmembers are defined at smaller scales, the scene will be highly structured in terms of the endmembers and thus the spectral mixing is more non-linear. If we define

endmembers at larger scales, although the endmembers themselves are highly structured, the scene will be less structured and thus the spectral mixing is more linear. From another view point, since larger scale endmembers themselves are actually non-linear mixtures of the smaller scale endmembers, the mixing of their spectra at the scale of the observation must be less non-linear than the mixing of the smaller-scale endmember spectra.

The scale at which the endmembers are defined has impacts on not only the characteristics of the mixing model, but also the interpretation of the SMA results. While small-scale endmembers tend to address the biochemical or geochemical composition (e.g., green vegetation, woody material), the large-scale, structured endmembers can be directly related to the physical features (e. g., trees) in the field. Particularly, when “shade” is added as an endmember to account for the structural effects (e.g., Smith et al., 1990), its interpretation apparently depends on the scale the other endmembers are defined. With scale-independent endmembers, there are likely significant uncertainties in interpreting shade fraction in images of highly structured scenes (e.g., Smith et al., 1990).

To illustrate the structural effect, Figure 2.1 shows the simulated spectra of scenes containing two spectrally distinct components, the average spectra of which are represented by the large open squares. If both scene components are assumed of structureless, the resulted spectra (solid circles) distribute along a line connecting the spectra of the scene components. In this situation, the spectra are exactly the mixtures of the spectra of two scene components, and the endmember fractions correspond to the fractional abundance of scene components. Such correlations no longer exist when the scene is structured, with one component ball-shaped and lying on top of the other (Fig. 2.2a). The distribution of the simulated spectra (open circles in Fig. 2.1) of the structured scenes largely deviates from the spectra mixed with the spectra of the scene components. The structure is the key factor here causing the deviation since the spectra of scene components are same in both simulations. Due to the structure, the flat layer

is partly shadowed and the amount of shadows depend on the number and size of the balls (Fig. 2.2b). the proportion of the flat layer being shadowed increases with the coverage of the “ball” components. As a result of the shadows, the observed spectra are darker than the linearly mixed spectra of the two scene components at corresponding proportions. Therefore, structure is an important factor in relating the spectral mixing to scene compositional mixing.

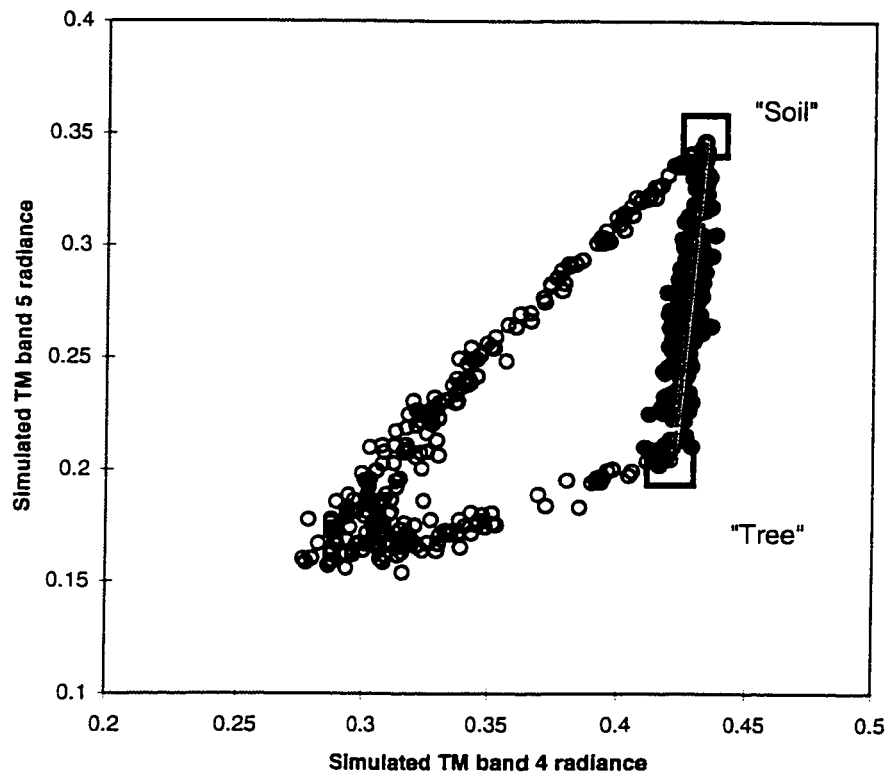


Figure 2.1 Surface structure affects the linearity of spectral mixing. The scene consists of two endmembers, “soil” and “tree.” If the surface is assumed to be unstructured, its spectra (solid circles) can be presented as linear mixtures of the endmember spectra (squares). When surface structure is assumed, the actual spectra (open circles) significantly deviate from the linear spectral mixing line (gray line).

Although the shadow itself is not a compositional component in the scene, it is an image endmember in the spectral mixing due to the structural effects. As shown in Figure 2.2a, there are only two compositional components, the ball and the flat layer, in the scene. In the image (Fig. 2.2b), however, there are three distinct spectra, of ball, shadowed flat layer, and sunlit flat layer, respectively. When shade is added as an image endmember, the simulated spectra can be fairly well treated as linear mixtures of the spectra of these three endmembers. This is the usual approach in SMA (e.g., Smith et al., 1990). However, the problem arises as how to interpret the shade: is it cast by the “ball,” the flat layer, or both of them? Obviously, to answer this question requires us to examine the surface structure at the scale of the chosen endmembers.

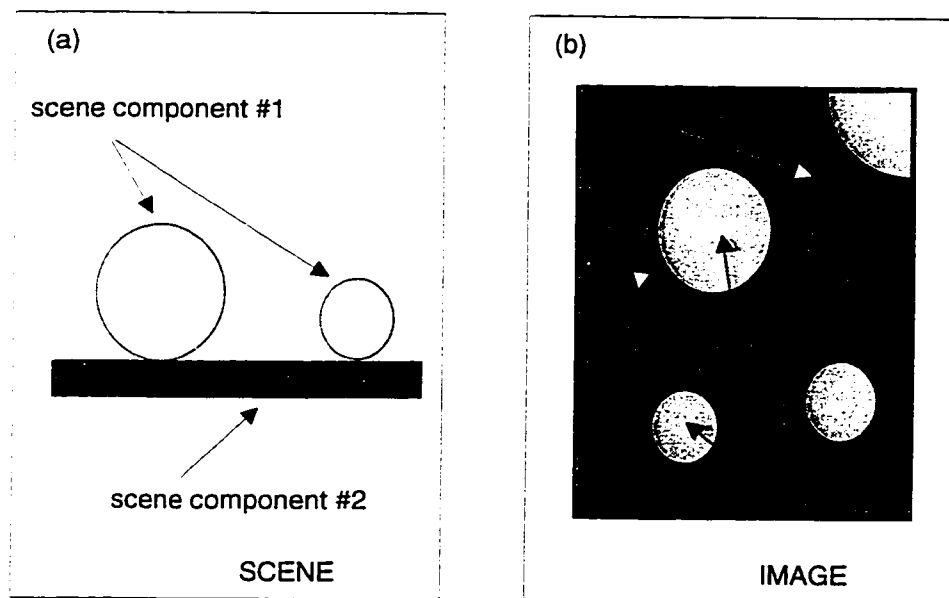


Figure 2.2 Sketch illustrating the difference between spectral mixing in image and compositional mixing in the scene. (a) Two components are present in the scene, “ball” and “flat layer.” (b) Three image endmembers are shown in the spectral image: “ball,” sunlit “flat layer” and shadowed “flat layer.”

2.3 LINEAR SPECTRAL MIXTURE MODEL

Typically, spectral mixture analysis is done with linear models. For the linear mixing model, it is assumed that the spectra in images are linear combinations of the endmember spectra, with coefficients linked to their fractional abundance in the scene. Therefore, if the spectra for the endmembers are known, either through laboratory or field measurements, then it is possible to extract the fractional abundance of each endmember by unmixing the spectra, pixel by pixel, to get the distribution map of each scene component.

2.3.1 SMA Model

Suppose the reflectance spectra of N endmembers are $\{\rho_i, i = 1, 2, \dots, N\}$, where each ρ_i is a vector representing the reflectance spectrum of the i th endmember, then the linear model gives the mixed spectrum, ρ , of the endmembers according to fractions $\{f_i, i = 1, 2, \dots, N\}$ as

$$\rho = f_1\rho_1 + f_2\rho_2 + \dots + f_N\rho_N = \sum_{i=1}^N f_i\rho_i, \quad (2.1)$$

or in a matrix form

$$\rho = \mathfrak{R}F, \quad (2.2)$$

where $\mathfrak{R} = (\rho_1, \rho_2, \dots, \rho_N)$ and $F = (f_1, f_2, \dots, f_N)'$, and \mathfrak{R} and F are the endmember spectrum matrix and fraction vector, respectively. The goodness of the linear model is measured by the RMS error of the fit, which is

$$RMS = \sqrt{(\rho - \mathfrak{R}F)'(\rho - \mathfrak{R}F) / (N_b - 1)}. \quad (2.3)$$

where N_b is the number of bands. Since the fraction of each endmember needs to be positive and less than one, and their summation needs to be unity, to find the fractional abundance of each endmember is equivalent to solving the linear inverse problem (2.2) with constraints,

$$\begin{cases} \sum_{i=1}^N f_i = 1 \\ 0 \leq f_i \leq 1, \quad \forall i = 1, 2, \dots, N \end{cases} \quad (2.4)$$

In practice, it is usually solved as an unconstrained linear inverse problem to get

$$F = (\mathcal{R}'\mathcal{R})^{-1} \mathcal{R}'\rho. \quad (2.5)$$

This solution is then back-checked to see if it satisfies the constraints (2.4), considering the variation in endmember spectra and measurement errors. If both constraints in (2.4) are met, the solution (2.5) is accepted. Otherwise, we need either to search again for the solution to the problem or to treat it as an anomaly (e.g., Gillespie et al., 1990).

2.3.2 Endmember selection

The endmembers are the basic components in the scene. Green vegetation, non-photosynthetic vegetation, soil, and shade are chosen as endmembers in a variety of SMA applications (e.g., Roberts et al., 1993; Smith et al., 1990; Adams et al., 1995). They themselves may be mixtures of smaller-scale components. For example, soil is usually a mixture of many different kinds of materials, including minerals, dry grass, and litter.

2.3.3 Shade as an endmember

Since the structure of the scene has not been considered in the linear spectral mixture analysis, the spectra obtained by mixing the endmember spectra are usually not comparable to observed image spectra. Due to shading (local incidence angle variation) and shadowing (blocking of illumination), the actual scene is always darker than predicted. The “shade” endmember is then introduced in addition to the materials existing in the scene to account for the structural effects.

2.3.4 Interpretation of endmember fractions

Although it is implied in linear spectral mixture analysis that the fractions in equation (2.1) are directly corresponding to the actual abundance of endmembers, it is not always correct in a strict sense. Based on the radiation theory, the actual radiance, L , of a surface composed of N components can be expressed as

$$\begin{aligned} L &= \frac{1}{\pi} \iint_A E(\bar{x}) \rho(\bar{x}) dS = \frac{1}{\pi} \sum_{i=1}^N \rho_i \iint_{A_i} E(\bar{x}) dS \\ &= \frac{1}{\pi} \sum_{i=1}^N A_i \rho_i \bar{E}_i \end{aligned} \quad (2.6)$$

where A_i and \bar{E}_i are respectively the areal abundance and average irradiance onto the i th component. Therefore the reflectance of the surface is

$$\rho = \frac{2L\pi}{\sum_{i=1}^N A_i \bar{E}_i} = \sum_{i=1}^N \frac{A_i \bar{E}_i}{\sum_{j=1}^N A_j \bar{E}_j} \rho_i. \quad (2.7)$$

Comparing it with equation (2.1), we find that

$$f_i = A_i \bar{E}_i / \sum_{j=1}^N A_j \bar{E}_j. \quad (2.8)$$

Therefore, the endmember fractions in linear spectral mixture analysis are usually different from their areal abundance. Only when all endmembers are, on average, under the same illumination conditions are the SMA-estimated endmember fractions directly related to their areal abundance. In this situation, the areal abundance of endmembers estimated by the simple spectral analysis is

$$f_i = A_i \bar{E}_i / \sum_{j=1}^N A_j \bar{E}_j = A_i / \sum_{j=1}^N A_j = \frac{A_i}{A}. \quad (2.9)$$

However, as the shading and shadows are usually non-uniformly distributed in the scene and different components receive different irradiance, the linear spectral mixture model will not give accurate information on the abundance of endmembers. This is one of the major drawbacks of the linear mixing model.

2.4 LAYERED SPECTRAL MIXTURE ANALYSIS (LSMA) MODEL

As discussed in Chapter 1, many natural surfaces are highly structured at certain spatial scales. These structures, even if unresolved, play important roles in controlling the bidirectional reflection of natural surfaces. Here is presented a layered spectral mixture analysis (LSMA) model for the purpose of investigating structural effects on spectral mixing. For simplicity, the scene is assumed to consist of two layers.

2.4.1 Layered spectral mixture model

Suppose that the scene is stratified as two layers of different reflectance, say, the higher layer as layer T with reflectance ρ^T and the lower layer B with reflectance ρ^B , respectively. Also suppose that the scene is mixed by the two layers at proportions of f^T and f^B respectively. Based on radiance equation (2.6), the observed radiance will be

$$\begin{aligned} L &= \frac{1}{\pi} \iint_A E(\bar{x}) \rho(\bar{x}) dS = \frac{1}{\pi} [\rho^T \iint_{A^T} E(\bar{x}) dS + \rho^B \iint_{A^B} E(\bar{x}) dS] \\ &= \frac{1}{\pi} (f^T \rho^T \bar{E}^T + f^B \rho^B \bar{E}^B) \end{aligned} \quad (2.10)$$

where \bar{E}^T and \bar{E}^B respectively represent the average irradiance on the top and bottom layers, A^T and A^B respectively represent the fractional area of the top and bottom layers.

The top layer, however, casts shadows on the bottom layer, the amount of which depends on the coverage of the top layer. Because the average irradiance on the bottom layer depends on the fractional abundance of the top layer, the spectral mixing is intrinsically non-linear. However, the illuminated and the shadowed portions on the bottom layer each have irradiance independent of the coverage of the top layer. Therefore, if the bottom layer is divided into sunlit and shadowed portions, then the

original non-linear two-layer mixing problem becomes a three-endmember linear mixing problem

$$L = \frac{1}{\pi} (f^T \rho^T \bar{E}^T + f^L \rho^B \bar{E}^L + f^S \rho^B \bar{E}^S), \quad (2.11)$$

where \bar{E}^L and \bar{E}^S , f^L and f^S represent the average irradiance and the fraction of the sunlit and shadowed bottom layer, respectively. When written in terms of radiance, the two-layer, three-endmember spectral mixing model is

$$L = f^T L^T + f^L L^L + f^S L^S, \quad (2.12)$$

where L^T , L^L , and L^S are respectively the radiance of the top layer, sunlit bottom layer and shadowed bottom layer.

Now the areal proposition of the top layer and bottom layer can be estimated by inverting equation (2.12) under constraints

$$\begin{cases} f^T + f^L + f^S = 1 \\ 0 \leq f^T, f^L, f^S \leq 1 \end{cases}, \quad (2.13)$$

in a similar way as in the linear spectral mixing model.

2.4.2 Endmember Spectra

Unlike in linear spectral mixture analysis, in which the endmember spectra are defined as their reflectance spectra, endmember spectra in the layered model are defined as radiance spectra (2.12). Such a choice is not only for the convenience of linking the endmember fractions directly to their areal abundance in the scene, but quite natural if the complexity of lighting is considered at the sub-pixel scales. Due to shading, shadowing, and multiple scattering within a structured surface, the variation in the illumination onto the scene components is likely larger than the variation in the reflectivities of these components. Therefore, the observed spectrum is not only related to the compositional variation of the surface, but even more so to its structural variation. Unlike the limited number of components in the scene, however, the variation in illumination is continuous from complete shadows to bright highlights,

causing the non-uniqueness in both selection and interpretation of the endmembers. If the endmembers are not defined at specific scales so that they all have certain structures and thus corresponding illumination distributions, the variation in illumination condition in different components will cause ambiguity in interpreting the spectral mixtures. It will be difficult to identify structural or compositional variations. To treat the observed spectra as mixtures of the radiance of structured endmembers reduces such ambiguities.

In particular, it is the irradiance, not the reflectance, that differentiates the shadowed from the illuminated bottom layer. Their reflectances are exactly the same, but not so the irradiance and the radiance. Therefore, to choose radiance over the reflectance as endmember spectra is more reasonable, considering the structures of natural surfaces.

Endmember spectra can be measured in the field, under the same illumination conditions as the image was taken. Although it may seem to be a rather difficult requirement, actually it takes no extra work than acquiring reflectance spectra for simple SMA. In interpreting the results of simple SMA such information is also required as shading changes with sun position. Obviously, the endmember spectra can be significantly different even when they are defined at the same scale in layered and simple SMA models because intrinsic and inter-layer shades are differentiated in the former (see discussion below).

A library storing the spectra of structured endmembers can be established in the same way as that for simple materials. In addition, computer-simulated structures can also be used to obtain approximations for the endmember spectra in the scene.

2.4.3 Intrinsic Shade and Inter-Layer Shade

Intrinsic shading and shadowing are caused by the variation of local incidence angle and mutual shadowing within each layer. This class of “shade” has been included in the spectra of each layer and has no contribution to the shade fraction

estimated from equation (2.12). The inter-layer shade exists as the results of shadows cast by the top layer on the bottom one. The shade fraction estimated from the layered model is the amount of the inter-layer shade. This is in contrast to the simple SMA, which includes all shading and shadowing in the shade endmember.

2.4.4 Advantages of the layered model

The consideration of scene structure has given the LSMA model two advantages over the simple SMA. Because of the scale to define the endmembers, the non-linearity of spectral mixing is reduced in LSMA. It has particular importance in interpreting residual spectra which contain the information about the appropriateness of the mixture model. If the non-linearity is not the major source of the residual, then it is very likely that large residuals are corresponding to compositional anomalies in the scene. With simple SMA, however, it is usually difficult to differentiate whether the misfit is caused by non-linear mixing or compositional variation.

The other advantage with the layered model is that the results are ready to relate to the scene compositional components. Distinguishing the inter-layer shade from intrinsic shade makes it possible to convert the shade fraction more accurately into other endmembers associated to scene composition than in simple SMA. Associating endmembers to scene compositional elements at certain spatial scales also contributes to the easy interpretation of LSMA results. There is no late-stage work necessary for correlating the unmixing results to scene characteristic features. For example, applying simple SMA to a scene may yield the result like: 40% vegetation, 25% woody materials, 10% soil and 25% shade. These numbers, however, do not tell us much about the actual characteristics of the scene. In comparison, the LSMA may yield the results such as: 70% trees, 10% sunlit soil, and 20% shadowed soil. Immediately, we know some important compositional and structural features of the scene.

2.4.5 Mixed Layers

For natural surfaces, each layer is composed of different components and we may be interested in particular components in each layer. For example, a canopy layer may consist of many tree crowns of different reflectance due to variations in shape, species, age, and other factors. Similarly, the substrate may also be mixtures of several soil types, green vegetation, litters and so on. Such compositional variations in each layer will cause variations in their spectra. If the variation is not large, using the mean spectrum for each layer may still be adequate to obtain good estimates of each layer's coverage. In case the spectra vary largely, or we need information on the components in each layer, however, the second level unmixing needs to be conducted. This mixture analysis can be done similarly to the simple spectral mixture model since it is assumed there are no significant structure within each layer. The second-level spectral mixing equations are

$$L^T = \frac{1}{\pi} \sum_{i=1}^{N^T} f_i^T \rho_i^T E_i^T, \quad L^L = \frac{1}{\pi} \sum_{i=1}^{N^L} f_i^L \rho_i^L E_i^L, \quad L^S = \frac{1}{\pi} \sum_{i=1}^{N^S} f_i^S \rho_i^S E_i^S. \quad (2.14)$$

Or combining it with the first-level mixture model, we have the hierarchical spectral mixing model

$$L = \frac{1}{\pi} \left(\sum_{i=1}^{N^T} f_i^T \rho_i^T E_i^T + \sum_{i=1}^{N^L} f_i^L \rho_i^L E_i^L + \sum_{i=1}^{N^S} f_i^S \rho_i^S E_i^S \right), \quad (2.15)$$

with the constraints

$$1 = \sum_{i=1}^{N^T} f_i^T + \sum_{i=1}^{N^L} f_i^L + \sum_{i=1}^{N^S} f_i^S \quad (2.16)$$

In a similar way as in SMA, the above constrained equation can be solved as a linear system, except that extra attention should be given to the stability of its solutions. If the radiance spectra of two or more endmembers (either in same layer or in different layers) are similar to each other, the solution will become unstable. In this situation, the spectrum and composition of the scene are not one-to-one correlated, and any inversion algorithm will fail.

2.5 INVERSION OF CANOPY PARAMETERS

Applying spectral mixture models to extract information directly related to the features of forest canopies, such as coverage, composition, and roughness, is necessary in order to map forest communities accurately. Due to the transmissivity of trees and gaps between tree crowns, the exposed substrate causes variability in the spectra of forest canopies, resulting difficulties in identifying and differentiating forest communities, particularly in case the substrate varies significantly from one location to another. With this regard, the spectral mixture analysis can be a powerful tool to separate the canopy layer from the substrate layer, and to differentiate among the compositional varieties within the canopy layer.

In the past, the endmembers in studying forest have been taken as green vegetation, woody material, soil, and shade (e.g., Adams et al., 1995). The endmember spectra measured away from the actual canopy structure, however, are not representative of their spectra in the scene because the structure by which these materials are organized has changed the lighting environment (e.g., Roberts et al., 1990). The non-linearity is expected to be large. On the other hand, tree, substrate and shaded substrate together make good endmembers because they are the largest-scale structures within the IFOV of the sensors. As mixtures of the above more fundamental materials in certain structures, these endmembers are more closely related to the spectral mixing of the observed forest spectra. In this section, the simple and layered SMA models, based on the above two scenarios of defining endmembers, are applied to a series of canopies to investigate the significance of canopy structure in spectral mixing analysis.

2.5.1 Canopy Simulation

Two canopies were constructed, one with trees of sphere-shaped crowns and the other ellipsoid-shaped crowns, to study the impacts of canopy roughness. The sun

(illumination source) elevation angle was set at 30° and 60° to account for the variation in illumination geometry in different seasons. Therefore, there are a total of four simulations for different combination of canopy roughness and sun position (Fig. 2.3). For each simulation, 250 canopies were constructed with randomly distributed canopy closures between zero and one. To allow some natural variability in the scene, 20% random noise is added to the reflectance of both trees and the substrate. The reflectance values of the canopy element and the substrate are taken from spectral library as representatives of green vegetation and soil.

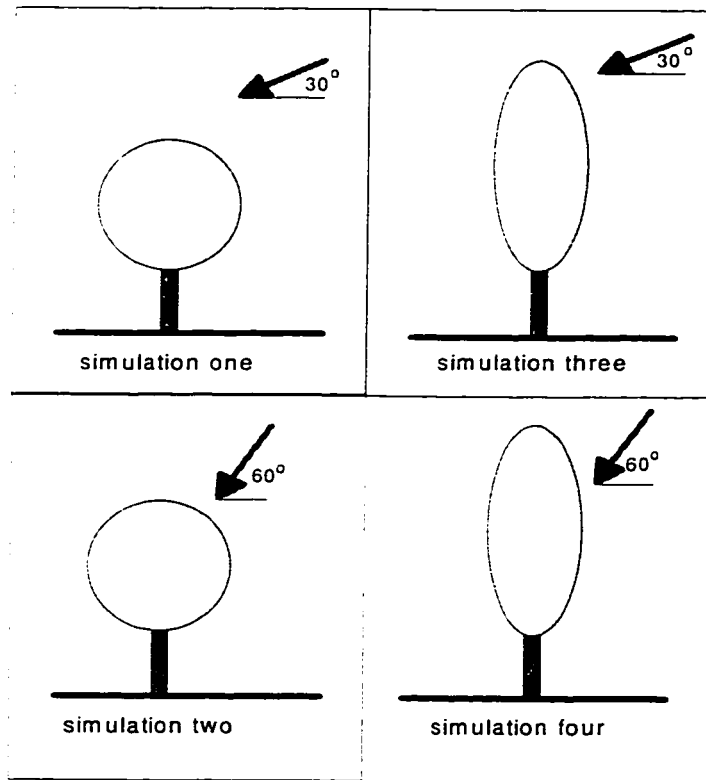


Figure 2.3 Structure and illumination geometry of simulated forest canopy data. Simulation 1: ball-shaped tree crown, sun elevation 30° ; Simulation 2: ball-shaped tree crown, sun elevation 60° ; Simulation 3: ellipsoid-shaped tree crown, sun elevation 30° ; Simulation 4: ellipsoid-shaped tree crown, sun elevation 60° .

2.5.2 Results of simple spectral mixture analysis

The SMA was then applied to the simulated data with three endmembers: the tree element, the substrate element, and the shade. Without assuming any knowledge on the source of the shade endmember, the shade fraction was proportionally partitioned among the other two endmembers. In this way the fraction of endmember tree was converted to the canopy coverage:

$$f_c = \frac{f_t}{1 - f_{sh}}. \quad (2.17)$$

The results of SMA, shown in Figure 2.4, indicate that the canopy closures estimated with the SMA are always higher than their actual values, particularly for low sun illumination. The maximum deviation usually occurs at intermediate canopy closure, 45% for low-sun and 60-70% for high-sun images. Such results are easy to explain, considering the canopy closures are estimated by uniformly partitioning the shade fraction. This assumption is not justified for forests because the shadows are dominantly distributed on the substrate although both tree crowns and the substrates are shaded. Consequently, the shade endmember compositionally corresponds to more substrate than the tree crowns. Therefore, partitioning the shade fraction proportionally among tree crown and substrate will over estimate the abundance of tree crowns but under estimates the proportion of substrate.

Results produced by SMA are largely dependent of illumination geometry (Table 2.1). The overestimate is much larger in the low-sun images (simulations 1 and 3) than in the corresponding high-sun images (simulation 2 and 4). When the sun elevation is 30°, average errors of the model's prediction are 28% and 34%, respectively, for the sphere (simulation 1) and ellipsoid-shaped (simulation 3) tree canopies. In comparison, the corresponding errors are 13% and 17% when the sun is at 60°. Such behavior is predictable because in lower-angle illumination, more substrate is shadowed and thus more shadowed substrate is interpreted as canopy, causing larger overestimate of the canopy coverage.

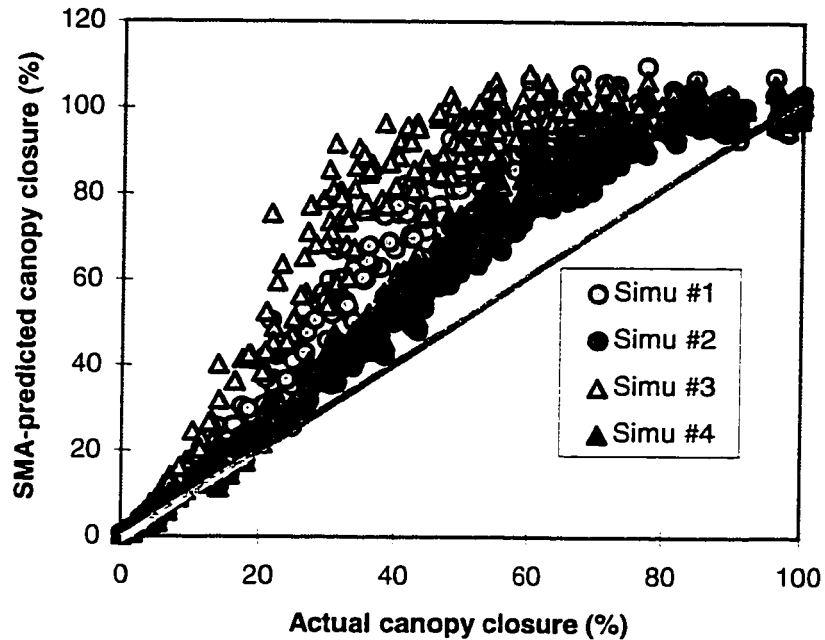


Figure 2.4 Correlation between actual and estimated forest canopy coverage. Linear SMA model generally overestimates canopy closure for the simulated canopy data. The prediction errors are larger when the sun is lower (simulations 1 and 3) than when it is higher (simulations 2 and 4).

Canopy roughness affects, but less than the illumination, the accuracy of the estimated canopy coverage. In average, the canopy coverage is overestimated by 13% (high-sun) and 28% (low-sun) for the ball-shaped tree canopy (simulations 1 and 2), in comparison to the corresponding overestimates of 17% (high-sun) and 34% (low-sun) for the ellipsoid-shade canopy (simulations 3 and 4). For the simulated data, the simple SMA appears more accurate when applied to smoother canopies than rougher canopies. However, there is not enough evidence to make such an observation conclusive because it is not clear how canopy roughness will quantitatively affect the amount and distribution of inner-layer and inter-layer shades. When canopy structure changes, both the shading and shadowing within the canopy layer will change. Also changed is the proportion of shadowed substrate. Therefore, it is hard to predict

whether the variation of canopy roughness will strongly cause more shade for one particular endmember.

Table 2.1. Accuracy of canopy closure estimated with SMA and LSMA

	Sun	Crown	SMA		LSMA	
	Elevation	Shape	Error	r^2	Error	r^2
simulation 1	30°	ball	27.8%	0.723	5.2%	0.974
simulation 2	60°	ball	13.1%	0.950	4.0%	0.984
simulation 3	30°	ellipsoid	34.3%	0.497	7.0%	0.941
simulation 4	60°	ellipsoid	17.3%	0.914	4.3%	0.977

The prediction errors are also reflected in the correlation between the predicted and the true canopy closure. As shown in Table 2.1, the relatively low correlation coefficients (r^2) indicate that the SMA model is not particularly accurate in predicting forest canopy closure, particularly in low-sun images.

2.5.3 Results of the Layered Spectral Mixture Model

The same canopy data were analyzed with the layered spectral mixing model (LSMA). The radiance spectra of the two endmembers, the canopy layer and the substrate layer, are calculated from the simulation data. Different from SMA, which takes the element of tree crown as an endmember, in LSMA the canopy itself is an endmember and thus its fractional abundance is directly corresponding to the canopy coverage. Figure 2.5 shows the results of the LSMA. Clearly, the canopy closures predicted with the LSMA are highly correlated to the actual canopy closure in general. Most of the variation (>94%) of the estimated canopy is due to the actual variations in canopy coverage (Table 2.1). As expected, the LSMA yields more accurate results and

smaller prediction errors (4-7%), than the simple SMA which causes errors between 13-34% in four simulations (Table 2.1).

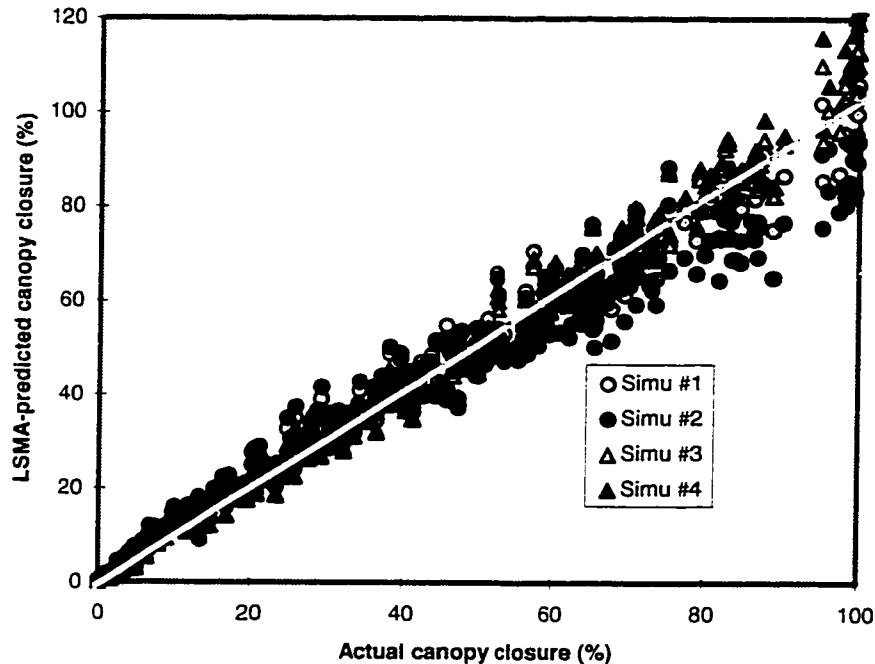


Figure 2.5 Correlation between actual and estimated forest canopy coverage. The LSMA model yields much better predictions than the linear SMA model in all simulations. Slight underestimates in the high canopy-closure end are evident for simulation 3, which is related to the significant structures within the canopy layer.

Tree shape and sun position have little impact on the performance of LSMA. As in the SMA, it is generally true that the rougher the canopy and the lower the sun, the poorer the model's performance. However, these factors have only very small impacts in comparison to the simple SMA.

2.5.4 Non-Linear LSMA

Nevertheless, careful examination at the closed canopy end in Figure 2.5 reveals that the model-predicted canopy coverage is lower than the actual coverage for

the ellipsoid-shade tree canopies when the sun is low. To understand why the model breaks down, the spectral variations of the average radiance of tree crowns (spectra of endmember “canopy”) are displayed (Fig. 2.6). As canopy closure increases, the tree crowns’ radiance decreases, as a result of more shadows being cast within the canopy. Therefore, the spectrum of the canopy layer is not invariant but changes with the degree of canopy closure. This result is due to the violation of the assumption in the layered model that each layer is structureless. At high sun or for smooth canopies, the structure within the canopy layer is not significant. As canopy gets rougher and the sun is lower, however, this structure becomes significant and causes a large difference in pattern and amount of shadows within the open and closed canopies. In this situation, the structure within the canopy layer causes non-linear mixing in exactly the same way as the inter-layer structure does.

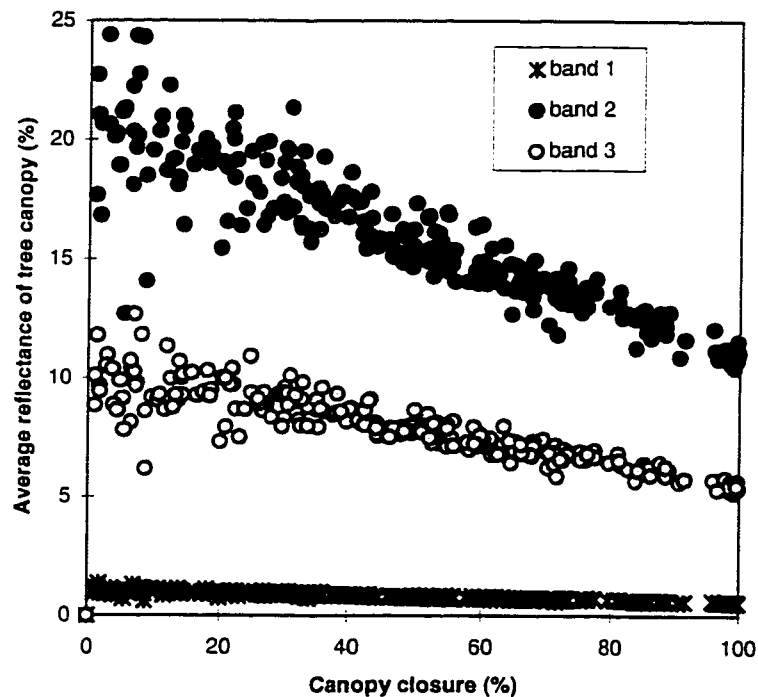


Figure 2.6 Average reflectance of the canopy layer varies with canopy closure in simulation 3. As canopy closure increases, the amount of shadows within the canopy layer increases and the canopy layer appears darker.

If the correlation between endmember fraction and its spectrum, $L(f)$, is known, then it is possible to solve the nonlinear mixing problem with a simple iterative method. As shown in Figure 2.6, for example, the canopy radiance spectra are approximately correlated to canopy closure:

$$L^T = 0.25 f^T L_0^T. \quad (2.18)$$

where L_0^T is the canopy radiance at 100% coverage. Therefore, we can first estimate canopy fraction under the assumption of constant canopy radiance. The canopy closure estimated this way is then plugged into equation (2.18) to find the canopy radiance at various canopy closures. Such obtained results are shown in Figure 2.7. Unlike the results (open circles) given by the linear model, which are lower than the actual numbers in the high canopy-closure end, the non-linear model yields a slightly more accurate prediction (solid circles) of the canopy coverage, with an average error of 5.8%, compared to 7.0% with the linear model.

2.6 SUMMARY

Two important factors have determined the observed spectra of a natural surface: composition and structure. A number of studies have shown that the structural characteristics of natural surfaces are probably the most important factor in controlling their bidirectional reflection and back-scattering at large scales.

Because of the structural variations, there is no one-to-one correlation between the spectral mixing and the compositional mixing for natural surfaces. With the knowledge of the structural characteristics of a specific scene, however, we can effectively relate the compositional and spectral mixing to each other so that compositional information of the scene can be extracted through unmixing the observed spectra.

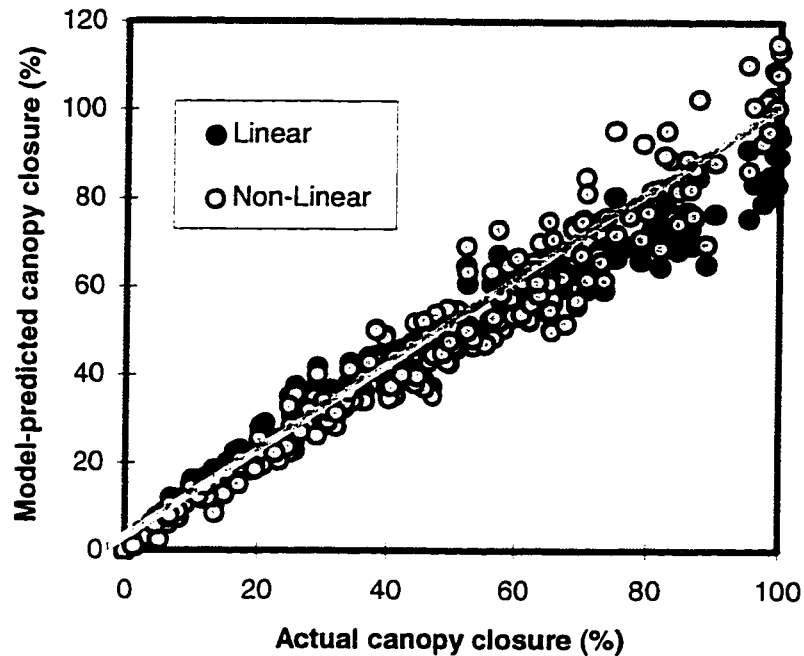


Figure 2.7 The non-linear spectral mixing model slightly improves the accuracy of LSMA. The average prediction error is reduced from 7% in linear LSMA to 5.8% with the non-linear LSMA model.

There are several reasons for the consideration of surface structure in spectral mixture analysis. First, surface structure controls the amount and pattern of shading and shadowing and thus changes the reflection spectra at sub-pixel-scale scene elements. Second, surface structure causes non-linearity in spectral mixing, which can be minimized by selecting structured endmembers. Finally, surface structure contains the information necessary for appropriate interpretation of SMA results.

A layered spectral mixture analysis (LSMA) model is then proposed to account for the structural effects on spectral mixing. Differing from the simple SMA, each endmember in LSMA is structured so that the scene itself is constructed with the endmembers in a simple structure. In this way, the spectral mixing in the image is

better correlated to the compositional mixing in the scene than in SMA. In addition, the differentiation between inner-layer and inter-layer shades help to interpret shade endmember more accurately.

The spectra of forest canopies composed of ball-shaped and ellipsoid-shaped trees under different illumination conditions are simulated and unmixed to invert canopy closures. The simple SMA overestimates the canopy closure largely due to its misinterpretation of the shadowed substrate as canopies. The applicability of simple SMA is also affected by canopy roughness, and especially sun position. The simple SMA yields poorer results on rougher canopies under illumination of a lower sun than on smoother, higher-sun-illuminated canopies.

The LSMA model gives more accurate estimates of canopy closure than the simple SMA. The estimated canopy closure is highly correlated to the actual canopy closure, with average errors of 4-7%, considerably smaller than the errors of 13-34% with the simple SMA. The canopy roughness and sun position in a similar way, but with lesser amount, affect the accuracy of the layered model.

The layered model works poorly for rough, closed canopies under low-sun illumination. The reason is that the smaller-scale structures within the canopy layer, which can be ignored under optimal conditions, are significant enough to cause the canopy layer's radiance to vary with the degree of canopy closure. As a result, the spectral mixing is non-linear. An iterative method may be used to solve the non-linear mixing problem, and the results appear to be improved comparing to the linear layered model.

It should be pointed out that the proposed layered spectral mixing model is still in its infancy, and more efforts are needed to make it applicable to natural surfaces that usually show very complicated structures. The purpose that it is presented here is to demonstrate the significant importance of surface structure and spatial scale in developing, understanding, and applying spectral mixture models to analyze the abundance and distribution of subpixel-scale components in the natural surfaces.

Further work will include extensive tests and refinements of the LSMA model for various circumstances. Besides vegetated surfaces, this model is anticipated to be useful in processing cloud-contaminated images, which are particularly common in tropical regions.

CHAPTER 3: TOPOGRAPHIC NORMALIZATION OF LANDSAT TM IMAGES OF FOREST BASED ON SUBPIXEL SUN- CANOPY-SENSOR GEOMETRY

3.1 INTRODUCTION

Forest mapping is an important application of remote sensing. Whereas images of low-resolution (1 km or more) are often used in large-scale tropical rain-forest studies for continental or global climate and environmental monitoring, high-resolution images such as obtained by the Landsat Thematic Mapper (TM) (~30 m) are useful for regional and local mapping and inventorying of forests and forest changes due to fire, disease and logging (e.g., Collins and Woodcock 1996; Olsson, 1995; Meyer et al., 1993).

The dominant source of variance in visible/near-infrared (NIR) TM forest images is topographic shading and shadowing because many topographic slope elements are resolved, particularly in mountainous areas. Topographic shading creates an ambiguity among scene components having similar hues and saturation but different intensities, leading to a reduction in classification accuracy (e.g., Itten and Meyer, 1993; Franklin et al., 1986). Topographic shading also makes it difficult to characterize unresolved sub-pixel-scale shadowing that could reveal information on forest canopy structure or surface roughness. Uncorrected topographic shading has hindered the attempt to use forest canopy roughness as a parameter to differentiate forest stands of different species and ages. In time-series analysis, terrain effects limit the recognition of the usually weak trends associated with seasonal variations, occasional drought or insect damage, and growth, especially because the individual images are typically obtained at various illumination conditions (Hill and Sturm, 1991). Therefore, recovery of true surface reflectance by removing topographic effects

(“topographic correction”) is an important task in successful forest studies (e.g., Conese et al., 1993; Proy et al., 1989).

Several topographic correction methods, using high-resolution digital terrain models (DTM) and photometric models, have been developed to remove the effects caused by terrain variations. The fundamental assumption in all these methods is same: the sun-terrain-sensor geometry changes with topography and contributes to variations in the scene radiance. Accordingly, these models normalize the sun-terrain-sensor geometry to remove or reduce variance due to pixel-scale topographic shading. Among the most often used models are the Lambert cosine correction (e.g., Meyer et al., 1993), Minnaert correction (Smith et al., 1980) and the c-correction (Teillet et al., 1982) models, all of which have been applied to forest images with some degree of success (e.g., Meyer et al., 1993). However, some topographic effects commonly remain in corrected images, either as residual topography (under-correction) or “negative” topography (over-correction) (Civco, 1989). These residual effects have been attributed to over-simplification by the photometric model, neglect of diffusive illumination (from sky and/or environment), and inaccuracy of digital terrain models (Civco, 1989). It is particularly expected that a more realistic forest canopy photometric or bidirectional reflectance function will remove the terrain effects significantly better than the simple models.

However, there are practical limitations on such efforts. First, complete bi-directional reflection distribution functions (BRDFs) for forest canopies are not available, although many in-situ measurements have been made (e.g., Deering et al., 1994; Ranson et al., 1994). Second, the in-situ measurements may not be representative of satellite measurements, which usually have lower spatial resolution, because the reflection property of many natural surfaces is scale-dependent (Gu et al., 1992). Third, forest-canopy BRDFs vary with stand age (Syren, 1994), species (Abuelgasim and Strahler, 1994), tree density, and season of the year (Kleman, 1987). Therefore, for different scene components, different BRDFs should be applied

correspondingly. Of course, this requires that the goal of the image analysis - scene characterization - has already been attained. Fourth, the BRDF, a measure of the forest canopy directional reflection, is likely affected by topography as well as canopy characteristics. Simulation studies by Schaaf et al. (1994) have shown that similarly vegetated sloping and flat surfaces have different BRDF shapes as well as different apparent albedos.

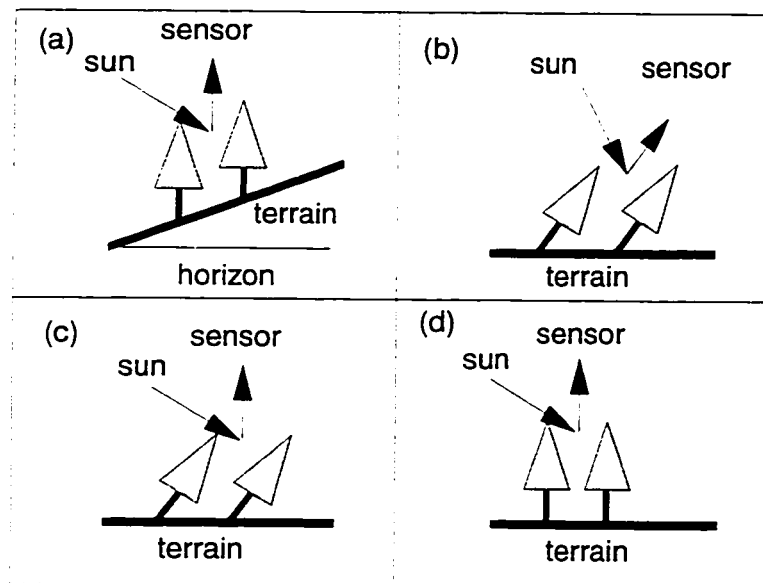


Figure 3.1 Geometrical presentation of sun-terrain-sensor geometry correction models: (a) forest canopy on the sloped terrain; (b) terrain rotated to horizontal; (c) after light compensation based on photometric functions; and (d) forest canopy on the flat terrain. Notice the sun-canopy-sensor geometry being changed from (a) through (c), and canopy structure in (c) no longer the same as in (d).

For simple photometric models, the sun-terrain-sensor geometry can be changed equivalently by choosing a different slope or by moving the sun. Because of the organized structure of the forest, however, this assumed relationship is simplistic: the interaction of light and the forest canopy is with individual leaves, branches and

trunks, all oriented with respect to the gravitational field, not the hill-slope. Therefore, at the scale of the remote-sensing measurement, it is reasonable to expect different changes in radiance for equivalent changes in sun-terrain-sensor geometry by variations of slope or sun elevation. As shown in Figure 3.1, the radiance for forest canopies on slopes (Fig. 3.1c) corrected using sun-terrain-sensor models is not the same as for that on flat terrain (Fig. 3.1d), because their structures are different with regard to the sun position. Therefore, the sun-terrain-sensor geometry normalization is not a proper approach to remove topographic effects on images of highly structured forest canopies.

It is necessary to develop a new topographic correction model for forests if remote sensing is to be of wide use in forest management and change studies. Because any single model is unlikely to be equally effective for all forest communities which show considerable amount of variabilities, a good model should be mathematically as simple as possible while accounting for the most important, general effects. The more parameters to be estimated and/or measured there are in a model, the less generally applicable it will be, although it may be more accurate for specific instances. As inferred from the results of Schaaf et al. (1994), five variables (sun zenith angle, sensor zenith angle, their relative azimuth angle, and terrain slope and aspect angles) are needed to characterize forest-canopy BRDFs, together with at least three additional parameters describing canopy structure (tree density, tree height, and crown shape). The estimation of these scene-dependent canopy parameters and the quantitative formulation of five-dimensional BRDFs is a challenge to those analysts needing terrain correction.

Presented here is a new terrain-correction model suitable for TM and other images of forests. The model is based on the interaction between solar radiation and canopy elements as affected by the variation of terrain slopes and aspects. It is first validated in a simulated Douglas fir canopy and then examined for its applicability to different canopy coverage conditions. The application of this model to the TM images

of a mature Douglas fir community confirms that it describes terrain effects for forests better than other models having the same number of model parameters, or more.

3.2 SUN-TERRAIN-SENSOR GEOMETRY CORRECTION MODELS

Given the hemispheric reflectance ρ of a forested surface that is characterized by surface-reflection model $f(G)$, where G represents the sun-terrain-sensor geometry, the reflected radiance is

$$L = \rho E_s f(G) \cos \theta / \pi, \quad (3.1)$$

where E_s is the solar irradiance at earth surface (nomenclature is summarized in Table 3.1), and the second-order illumination such as sky light and secondary reflection from neighboring hill slopes has been neglected. Variable θ is the solar radiance incidence angle relative to the local terrain surface and can be calculated from

$$\cos \theta = \cos \theta_s \cos \alpha + \sin \theta_s \sin \alpha \cos(\phi), \quad (3.2)$$

where θ_s is the sun zenith angle, α is the slope of the surface, and ϕ is the relative azimuth between the sun and the slope. Equation (3.1) describes the sun-terrain-sensor (STS) geometry correction model, the basis of current topographic normalization methods.

3.2.1 Cosine correction model

If the surface is Lambertian ($f(G) \equiv 1$), then we get the familiar cosine correction model:

$$\rho = \frac{\pi L}{E_s \cos \theta}. \quad (3.3)$$

The cosine correction model usually under-estimates the reflectance of sun-facing slopes and over-estimates the reflectance of slopes facing away from the sun, resulting in the appearance of “negative” or “inverted” topography in corrected images. This effect may be reduced by subtraction of the down-welling atmospheric irradiance,

which may contribute up to 10% of total irradiance in NIR and up to about 20% in visible bands from field measurements (e.g., Deering et al., 1994; Shoshany, 1993). Down-welling atmospheric irradiance is especially important on slopes facing away from the sun where topographic shading is stronger.

Table 3.1. Symbols used in terrain correction models

Symbol*	Explanation
θ_s	sun zenith angle (degrees)
θ	incidence angle (degrees)
α	terrain slope angle (degrees)
ϕ	terrain azimuth relative to the sun (degrees)
e	exitance angle (degrees)
ρ	surface reflectance (dimensionless)
E_s	solar terrestrial irradiance at earth surface (Wm^{-2})
\bar{I}	average irradiance on sunlit canopy (Wm^{-2})
ϵ	energy falling on a scene element (pixel) per unit time (W)
A	sunlit canopy area within a pixel (m^2)
L	radiance from a pixel on sloped terrain ($Wm^{-2}sr^{-1}$)
\hat{L}	model-predicted radiance from a pixel on sloped terrain ($Wm^{-2}sr^{-1}$)
S	surface area of a pixel (m^2)
c	empirical constant in c-correction model (dimensionless)
k	empirical constant in Minnaert model (dimensionless)
r	linear correlation coefficient (dimensionless)
δ_L	relative error of model-predicted radiance (dimensionless)

* subscript ₀ specifies corresponding quantities on horizontal terrain.

3.2.2 C-correction model

Examination of image data for rugged terrain shows that there is a linear correlation between L and $\cos\theta$ and the regression line commonly intercepts the L axis (where $\cos\theta = 0$) at a positive value (e.g., Teillet et al., 1982). To avoid over-correction, particularly for slopes facing away from the sun, Teillet et al. (1982)

proposed a c-correction model based on the observed empirical linear correlation between L and $\cos\theta$, described by regression slope m and offset a ,

$$\rho = \frac{\pi L}{E_s(\cos\theta + c)} \quad ; \quad c = \frac{a}{m}, \quad (3.4)$$

where c is assumed constant for a given band and scene. Although c must include skylight effects, its value is so large in some images that the c-correction method clearly lacks an exact physical explanation.

3.2.3 Minnaert correction model

Another well known approach employs the Minnaert Law (Minnaert, 1941) for terrain correction: $f(G) = \cos^{k-1}\theta \cos^{k-1}e$, where e is the exitance angle, which approximately equals to the slope of the surface for TM images, and parameter k , the Minnaert constant, is a measure of how close a surface is to the ideal diffuse reflector, for which $k=1$. For example, Smith et al. (1980) related surface reflectance to observed radiance for TM images through:

$$\rho = \frac{\pi L \cos e}{E_s(\cos\theta \cos e)^k}. \quad (3.5)$$

Because the parameter $k < 1$ for most natural surfaces, equation (3.5) reduces the terrain over-correction from the cosine correction.

When applied to TM forest images, the c-correction and Minnaert models produce comparable results. Both produce fewer topographic residuals than the Lambert cosine correction (e.g., Meyer et al., 1993).

3.2.4 Other models

More complicated photometric functions and BRDFs, such as those proposed by Walthall et al. (1985) and Liang and Strahler (1994), could be employed in the STS topographic correction model. However, any such efforts do not appear to have been published, probably because of the difficulties in verifying these empirical functions

for specific scenes or in estimating the parameters involved. On the other hand, the cosine correction, c-correction and Minnaert correction models have been widely used because they are relatively simple, with no or few scene-dependent parameters.

3.3 DERIVATION OF THE SCS TERRAIN CORRECTION MODEL

3.3.1 Scale of light interaction within a canopy

Hidden in the STS models is the assumption that the interaction of light with a natural surface is determined by the geometry of light source and underlying rock or soil slope. For forests, however, there are at least three distinct scales at which the interaction occurs. At the first scale (tree elements), light is scattered, transmitted and absorbed by leaves and branches, controlled by their biochemical constituents and structure. At the second scale (tree crown), the transmitted and scattered light after interacting with leaves and branches, is redistributed throughout the tree crown structure, as controlled by the biophysical parameters of the tree, such as density, orientation and distribution of leaves. At the third scale (canopy), mutual interaction of light among tree crowns further modifies the directional distribution as well as the intensity of the radiance observed by the sensor.

Since trees (like most plants) are geotropic, growing generally straight up, interactions at the first two scales are largely independent of topography. As a result, both the irradiance and exitance related to direct illumination are not affected by topography on sunlit portions of individual tree crowns. The indirect illumination from adjacent trees and slopes are affected by topography, but such effects are expected to be insignificant because indirect lights generally account for only a small proportion of the total illumination.

Topographic effects are introduced at the third scale because the relative positioning of trees is controlled by topography. As a result, more of each tree crown is exposed to the sun on sun-facing slopes and less on the slopes facing away from the

sun. In other words, the total area of the sunlit portions of the canopy largely depends on topography. Because the sensor is usually unable to resolve individual trees, it actually measures the collective radiance from all elements within its instantaneous field of view (IFOV). On sun-facing slopes, a larger proportion of sunlit tree crowns within the IFOV reflect significant amount of light back to the sensor, causing the canopy to appear brighter than on the slopes facing away from the sun. Therefore, topographic effects on forest images are largely related to the topography-controlled variation of canopy's sunlit area, which should be normalized in order to remove the topography.

With above understanding of the topographic effects on forest canopies, a new approach for correcting such effects was proposed. For convenience, it is named as the SCS model because it was derived from the sub-pixel sun-canopy-sensor geometry, the deterministic factor controlling forest canopy reflections.

3.3.2 Derivation of SCS model

To formulate the SCS model, we need to characterize quantitatively the canopy's sunlit area as a function of the geometry between the sun, sensor and terrain slopes. However, the complication caused by forest canopy parameters such as stand type, seral stage, as well as tree density makes the exact characterization intractable. Some approximate formulations have been achieved for several simplified models of tree crown shape, tree height and tree density (e.g., Abuelgasim and Strahler, 1994). Herein, a statistical approach is adopted to derive the function for different terrain slopes and aspects.

The total solar radiation energy, ε , intercepted by a surface element (i.e., an image pixel) on a terrain slope, is just the product of the solar irradiance E_s and the pixel's area projected in the direction of the sun radiation:

$$\varepsilon = E_s S \cos \theta, \quad (3.6)$$

where S is the area of the pixel on the slope (Fig. 3.2). If we let \bar{I} be the average irradiance on the sunlit part of the canopy, then the total area, A , of the sunlit part of the canopy within a pixel is

$$A = \frac{\varepsilon}{\bar{I}} = \frac{E_s S \cos \theta}{\bar{I}}, \quad (3.7)$$

by the definition of irradiance, i.e., energy per unit area. As defined in equation (3.7), A and \bar{I} are respectively the area and the average irradiance of the sunlit canopy within a pixel, different from S and $E_s \cos \theta$, the area and the average irradiance of the pixel, respectively. Apparently, A is always smaller than S , but \bar{I} larger than $E_s \cos \theta$ because there exist shadows as well in that pixel. Equation (3.7) holds for any terrain, therefore the sunlit canopy areas in pixels on the sloped terrain and the horizontal terrain are related to each other through

$$\frac{A}{A_0} = \frac{E_s S \cos \theta}{E_s S_0 \cos \theta_0} \frac{\bar{I}_0}{\bar{I}}, \quad (3.8)$$

where subscript $_0$ specifies the pixel on the horizontal terrain. However, as we have discussed above, the average irradiance on the sunlit portion of the canopy is largely independent of the terrain (i.e., $\bar{I} = \bar{I}_0$) and, in addition, we know from Fig. 3.2 that $\theta_0 = \theta_s$ and $S_0 = S \cos \alpha$. Therefore

$$\frac{A}{A_0} = \frac{\cos \theta}{\cos \alpha \cos \theta_s}, \quad (3.9)$$

The next step is to estimate the collective radiance from the sunlit part of the canopy, which is by definition the product of its average radiance and the total solid angle as viewed by the sensor. Since the TM sensors have approximately a nadir view, the solid angle extended to the sensor by the sunlit canopy is proportional to its area. Considering that the radiance from the sunlit part of the canopy is largely topography-independent, the total radiance from the sunlit part of the canopy must be approximately proportional to its area, too.

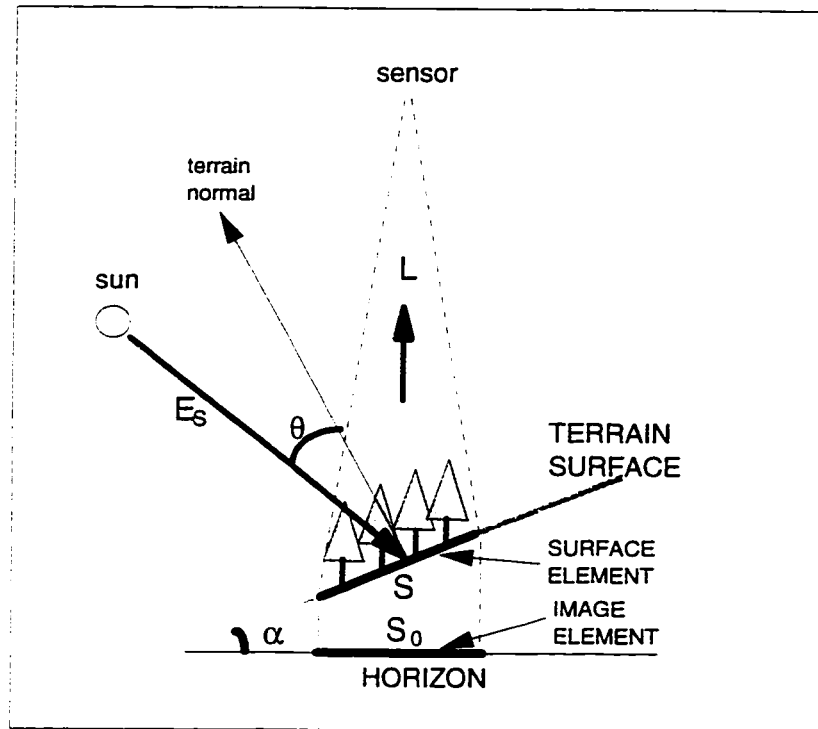


Figure 3.2 Geometry of light interaction with canopy on sloped terrain. The incidence angle of solar illumination on the terrain slope differs from the incidence angle on the sunlit part of tree canopy, which determines the irradiance on the sunlit parts of canopies.

Therefore, if we neglect the relatively small amount of radiance from the shadowed portion of the canopy, the total radiance arriving at the sensor from pixels on the sloped terrain, L , and the horizontal terrain, L_0 , are related to each other through

$$\frac{L}{L_0} = \frac{A}{A_0} = \frac{\cos \theta}{\cos \alpha \cos \theta_s}, \quad (3.10)$$

or

$$L = L_0 \frac{\cos \theta}{\cos \alpha \cos \theta_s}. \quad (3.11)$$

3.3.3. Comparison with STS model

It is interesting to compare SCS and STS terrain correction models from the geometric point of view. In STS model, the sloped surface (Fig. 3.1a) is effectively rotated by a coordinate system transformation so that all slopes are treated as horizontal (Fig. 3.1b). The photometric function is then applied to normalize the illumination, effectively returning the sun to its original position (Fig. 3.1c). With this procedure, however, the sun-crown geometry, which is actually independent of terrain slopes, has been changed. Therefore, the STS model normalizes the sun-terrain geometry at the cost of changing the sun-crown geometry, and hence the normalized pixels do not have equivalent canopy structure from the viewpoint of the sun (Fig. 3.1c, d). For this reason, the simple normalization of sun-terrain-sensor geometry is not adequate, at least for forests, for correcting terrain effects.

In contrast to the STS model, the SCS model changes neither the sun and sensor positions nor the canopy structure. What has been normalized is the sunlit area, while the irradiance on the sunlit canopies is kept invariant. This normalization is equivalent to projecting the sloped surface, in the sun direction, to horizontal. A larger effective solid viewing angle from the sensor is produced when the slope is facing toward the sun, and vice versa. The effective solid angle of projected “pixel” is determined by not only the incidence angle but also the slope angle through equation (3.9). Because the light-crown interaction geometry is preserved, the SCS model is more physically based than the STS model, and we anticipate that it should be superior for topographic normalization for forests.

3.4 MODEL VERIFICATION WITH SIMULATED FOREST CANOPIES

A computer-simulated canopy has been generated to verify the topographic correction models. Although the theoretical framework for the SCS model was developed for 100% closed canopy, in this simulation a more representative value of 70% canopy coverage was used. Tree parameters and distribution (Table 3.2) are

chosen based on field measurements at Bluff Creek, Six Rivers National Forest, California, described in the next section. With this model canopy, both the slope and azimuth of the substrate are simultaneously changed while the sun is fixed in east with the zenith angle of 30° , yielding a set of illumination conditions similar to that resulting from topographic variation in the actual scene. The radiance from the canopy under each illumination condition is calculated using a simplified version of the radiosity model of Borel et al. (1991).

Table 3.2. Tree parameters of the simulated forest canopies

Cone-shaped crown diameter	5 meters
Cone-shaped crown height	15 meters
Height of crown base to ground	6 meters
Reflectivity of tree crown	40%
Reflectivity of ground	40%
Distribution of trees	random

The radiance, normalized by flat-surface radiance, L_0 , is plotted against the cosine of the incidence angle in Figure 3.3. Each curve in Figure 3.3 represents a set of simulations with varying azimuth angles but fixed slope angle. The canopy radiance generally increases as $\cos\theta$ increases, but it also depends on the slope, with higher values on steeper slopes if θ is unchanged. Therefore, both slope and incidence angle are needed to quantify the radiance from forests in mountainous terrain.

The normalized radiance, multiplied by the cosine of slope angle, should be proportional to the cosine of incidence angle according to SCS model equation (3.10),

$$\frac{L}{L_0} \cos\alpha = \frac{1}{\cos\theta_s} \cos\theta. \quad (3.12)$$

Such linear correlation (with $r = 0.9967$) is confirmed in Figure 3.4 for the simulated forest canopy (Table 3.2). The scattering of radiance related to slope angle

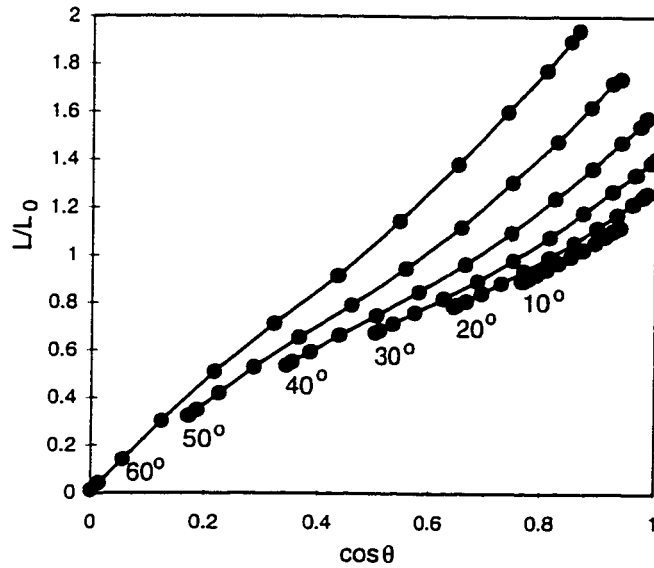


Figure 3.3 Radiance from the simulated canopy on various slopes. Radiance is affected not only by the solar incidence angle, but also by the slopes, which are given under each curve.

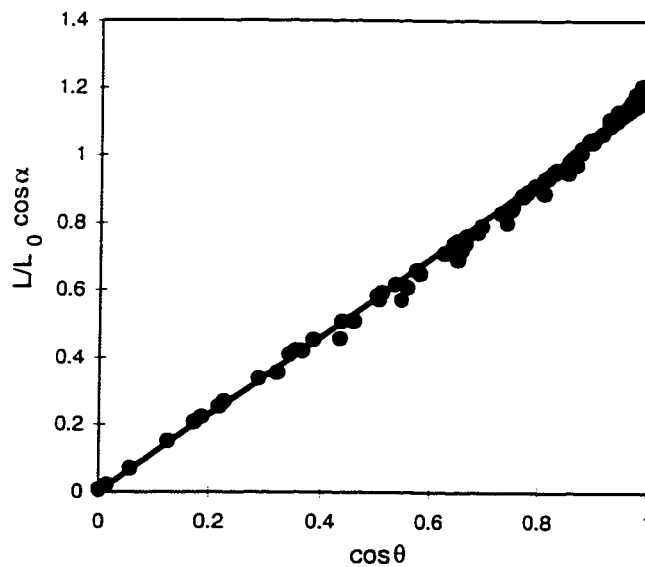


Figure 3.4 The SCS model fit to the simulated data. Most of the scattering in Figure 3.3 now disappears, indicating that the SCS model predicts terrain effects better than the Lambert model.

variation seen in Figure 3.3 has been significantly reduced in Figure 3.4. Not only is the fit improved, the slope of the fitted line, 1.159, is very close to the model-predicted slope, which is 1.154 for the sun zenith angle 30° . These results suggest that SCS model is accurate in predicting the topographic effects on the simulated canopy.

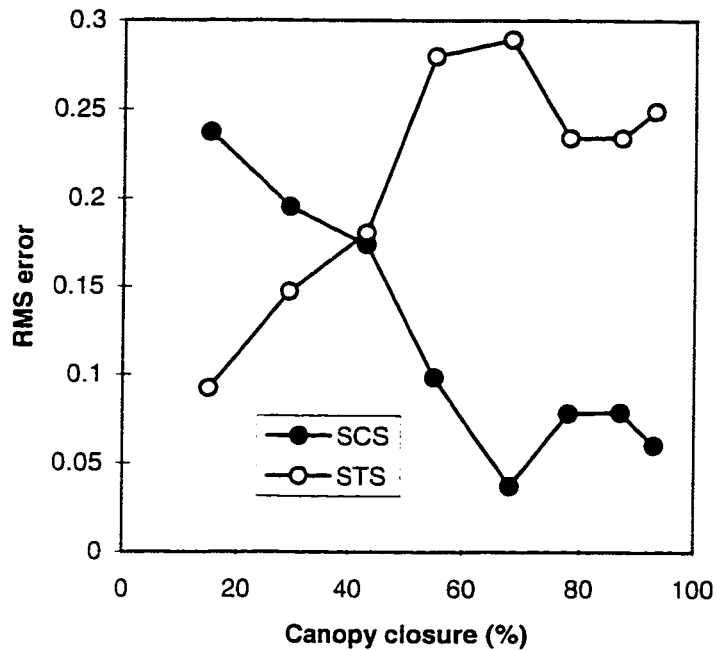


Figure 3.5 Applicability of the SCS model to surfaces with various degrees of canopy closure. The SCS model is more appropriate than the Lambert model for canopies of 50% or higher canopy-closure, and the Lambert model is good only when the canopy-closure is low (lower than 50%).

Terrain effects for sparsely vegetated slopes will be poorly characterized by the SCS model because its assumptions are violated. Therefore, it is important to examine the applicability of SCS model to forests with various degrees of canopy closure. Model surfaces that simulate canopies with 15%, 29%, 43%, 55%, 68%, 78%, 87% and 93% closure were constructed following the same procedures described above.

The exitance from each simulated canopy under various terrain conditions was calculated and normalized. The root-mean-squared (RMS) residual error of the SCS model's fit to the normalized radiance was estimated to assess the performance of SCS model (solid circles in Fig. 3.5). As expected, the RMS error is small for high canopy coverage of more than 50%, but generally increases with decreasing canopy closure, indicating that the SCS model is less applicable to low-closure, open-canopy forests (less than 50%). The second-order variations of RMS error for high-closure canopies are mostly related to the variability of tree distributions among different simulated canopies.

Conversely, the STS model works best for bare slopes for which the structured canopy is not a dominant scene component. Its accuracy decreases, however, as more trees are present on the scene. As the canopy closure exceeds 50%, the performance of the SCS model becomes markedly better than the STS model by a factor of about four as measured by RMS error (Fig. 3.5).

3.5 MODEL EVALUATION IN THE TEST SITE

3.5.1 Test site description

A forested, mountainous scene, imaged by Landsat TM was selected to test the SCS model. The test site is located in the northern part of Six Rivers National Forest, California, and comprises an area of 1.8×2.1 km, about 60×70 pixels in the TM image. Relatively uniform conifer stands and moderate to high terrain relief provide the necessary conditions for examining topographic effects and testing different correction methods. A ground survey conducted in late June, 1995, confirmed that the conifer stands are dominated by mature Douglas firs, with lesser numbers of pine trees, tan oaks, and hardwood trees. The canopy closure is around 80% in most of the test site. Slopes are commonly 20° and are locally as high as 40° .

3.5.2 TM image preprocessing

Landsat TM images of the test site, taken on 8 October 1990 and 9 July 1992 respectively, were selected to represent typical summer and fall imaging conditions at the temperate latitudes. The TM images were registered to a DTM having similar spatial resolution. Registration accuracy is typically better than 1 pixel; nevertheless local misregistration as great as 2 pixels may cause visible errors in topographic normalization, especially on ridges or streams. Approximate atmosphere path-radiance and instrument offsets were removed by using a nearby lake as a reference surface, assumed to have zero reflectance. The ratio of TM band 4 ($0.85 \mu m$) to band 5 ($1.65 \mu m$) was used as an index to remove hardwood-dominated pixels from the image subset. TM band 5, which is less affected by atmospheric scattering than the visible and near-infrared bands, was selected to examine the terrain effects.

Some flat pixels ($\alpha = 0$) were picked as control points and the radiance at these pixels were used to estimate the average radiance of the flat pixels, L_0 . The radiance at each pixel on the images were then divided by L_0 to get the normalized radiance for testing the topographic correction models.

3.5.3 Statistical evaluation of the SCS model

Figure 3.6 displays the strong topographic control of brightness for the test site. Although the data exhibit great variability, the normalized radiance clearly increases from shaded slopes to sunlit slopes.

The SCS model and three STS models (cosine correction, c-correction, and Minnaert correction) were applied to the test site. Three parameters were calculated to assess the performance of the correction models quantitatively:

1. The squared correlation coefficient (r^2) indicates the percentage of data variance explained by the terrain correction model. The higher the correlation, the better the model's fit to the data.

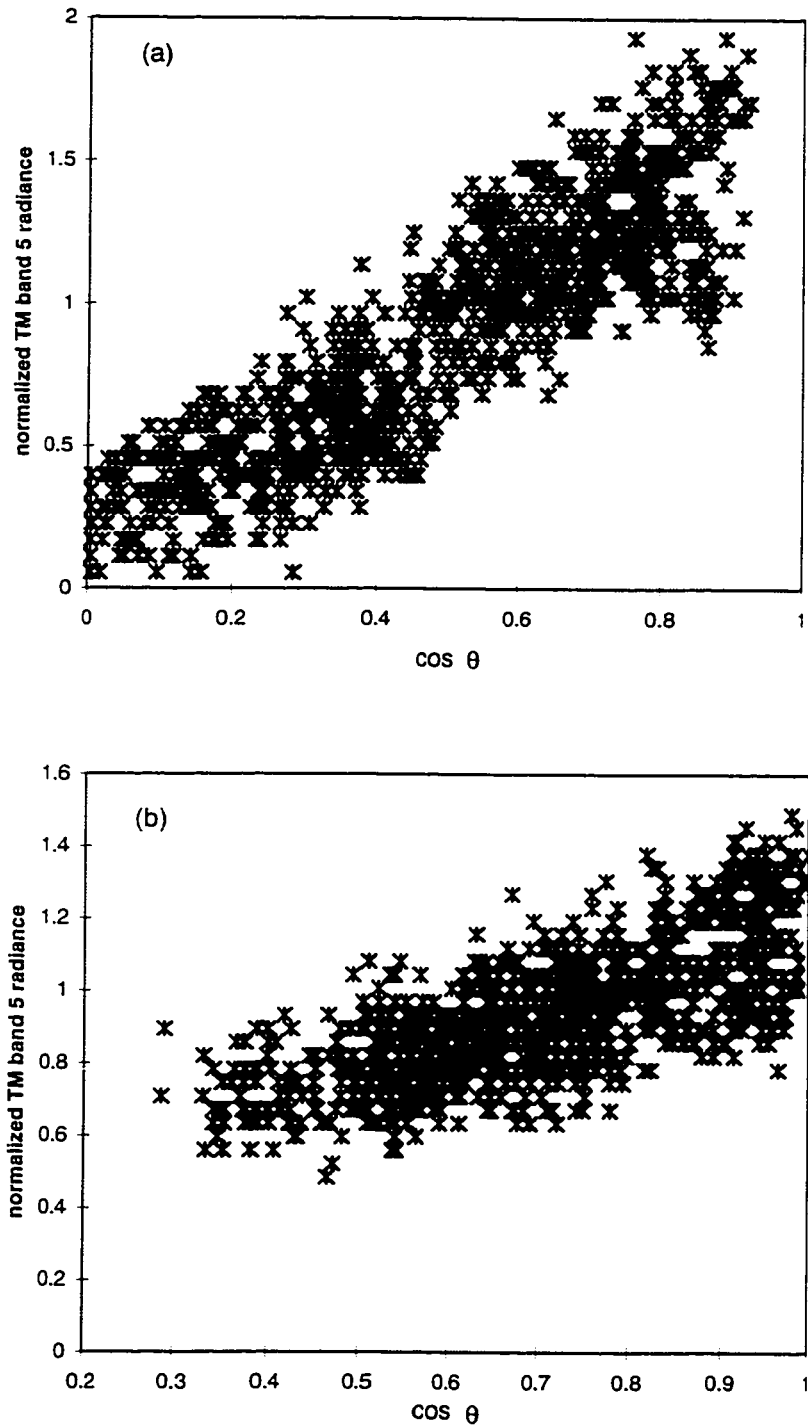


Figure 3.6 Scatter plots of TM band 5 normalized radiance vs. cosine of the solar incidence angle. (a) 8 October 1990 image; (b) 9 July 1992 image.

2. The RMS error measures the residual of the fit. The smaller the RMS, the better the fit. Moreover, comparing RMS error with the data noise level will help us understand whether the residual is caused by data noise or model's inaccuracy.

3. The relative error of model-predicted radiance on horizontal terrain, $\delta_L = (\hat{L}_0 - L_0) / L_0$, directly measures accuracy of the models, where L_0 is the observed radiance on horizontal terrain as estimated from the radiance of the selected flat pixels, and where \hat{L}_0 is calculated for each correction model with the model parameters estimated from the test data. If the difference is large, the correction model is not accurate even though it may fit the data well. On the other hand, smaller differences are likely related to more accurate models.

Table 3.3. Performance of terrain correction models on the test site

TM images	1990			1992		
Statistics	r^2	δ_L	RMS	r^2	δ_L	RMS
Cosine correction	0.77	8%	0.22	0.36	12%	0.18
C-correction	0.80	8%	0.20	0.53	7%	0.14
Minnaert correction	0.66	-9%	0.25	0.69	2%	0.13
SCS	0.80	-2%	0.20	0.66	1%	0.13
DATA		0%	0.20		0%	0.13

The test results listed in Table 3.3 suggest:

1. The SCS model consistently appears to characterize the topographic effects better than all three STS models for both 1990 and 1992 images, as shown by generally higher correlation coefficients, smaller δ_L and lower RMS errors.

2. The Minnaert correction is as good as the SCS model for the 1992 image, but fails for the 1990 image (lowest r^2 , highest RMS, and large δ_L).

3. On the other hand, the c-correction yields a relatively good fit to the 1990 image but poor fit to the 1992 image. In addition, it generally overestimates \hat{L}_0 (about 8%) for both images.

4. The cosine correction overestimates \hat{L}_0 (8% and 12% for the 1990 and 1992 images, respectively), in addition to fitting the data with lower r^2 and higher residual errors, particularly for the 1992 image.

5. The inconsistency of the c-correction and Minnaert correction models are also reflected in the model parameters, which are estimated from the test data in order to get the best fit. The empirical constant found for the c-correction model changed from 0.10 for the 1990 image to 0.42 for the 1992 image, and for the Minnaert model, it changed from 0.46 to 0.64.

It is important to compare the RMS error of these models to the data noise level. ("Noise" here restrictively refers to the satellite-observed within-class variability, which includes, but not limited to, the errors associated with image acquisition and processing. With such specification, the noise level is an important parameter for measuring the ability to distinguish different forest and/or non-forest communities in the scene). If RMS is higher than the data noise, the residuals still contain some useful information and the improvement of the models is probably necessary. However, if RMS is close to the data noise, the residuals may not contain much information useful for improvement of scene differentiation. In this situation, trying to fit the test data better does not necessarily lead to better results for many applications, such as forest mapping. Since there are no terrain effects on the flat pixels, the variation of the observed flat-terrain radiance is basically caused by noise as specified above and therefore the standard deviation of the normalized radiance for these flat pixels characterizes the level of data noise, independent of topographic effects. The noise levels estimated this way are 0.20 and 0.13 for 1990 and 1992 images, respectively. As shown in Table 3.3, the RMS errors for the cosine-corrected data are higher than the corresponding noise levels for both 1990 and 1992 images,

indicating that the cosine correction model will leave some significant amount of residual topographic effects. The Minnaert correction and the c-correction reduced RMS to the noise level only for the 1992 image and the 1990 image, respectively. Only the SCS model resulted the fit with RMS error matching the base noise levels on both images. Thus, for these examples, the performance of the SCS model was the best of all those tested.

3.6 DISCUSSION

Canopy structure has proven to be the most important factor causing the directional reflection of forest canopies (e.g., Koch et al., 1990). It is also important in the understanding of topographic effects on the satellite images of forested scenes. As pointed out earlier, the topography modifies canopy structure and causes terrain effects in the satellite observations. Such modification may occur at the sub-pixel scale as in the Landsat TM images, or at the pixel scale in images of higher spatial resolution in which individual trees are resolved. In the latter situation, topographic effects will not correlate to the sun-terrain-sensor geometry at all and the conventional STS model will not work. Instead, both the sun-canopy-sensor geometry at individual pixels and the mutual shadowing between neighboring pixels are the critical factors in normalizing the indirect topographic effects. Whether such a procedure is practically possible or not is beyond the scope of this paper, the point is that the topographic correction of forest images needs to be rooted in the consideration of canopy structures.

Some simplifications have been made in developing the SCS model in order to make it easy to use in practical remote-sensing studies. For example, only the radiance from the sunlit canopy is used in calculating the canopy brightness. Although darker than the sunlit part, the shadowed canopy may still have substantial contributions to the total reflectance because of the atmospheric down-welling radiation as well as the multiple scattering due to the canopy structure. In addition, the SCS model has not considered the viewing geometry effects when the sunlit canopy may be blocked from

the sensor, which can happen in the off-nadir-viewing systems. For this reason, the model at its present form is applicable only to the nadir-viewing systems, such as the Landsat TM. Future efforts will be focused on the development of analytical forms of the SCS model with improved accuracy and applicability.

We need to keep in mind that terrain effects are scene-dependent and that any single model will not describe such effects equally well for different scene components. The SCS model works better for forests, but the STS model, in any form, will be more appropriate for less-structured surfaces. How to correct terrain effects in a complicated scene is an important and interesting research topic. A possible strategy could be to apply different models to forested and non-forested areas, which usually have distinct spectra and are well separable. First, however, we need to assess whether such efforts are useful considering data errors and natural scene variability.

Other factors, such as the variation in terrain elevation, sky illumination, and secondary reflection from local environments, may all have significant impacts on the topographic corrections as well (e.g., Shoshany, 1989; Proy et al., 1989). In addition, data errors, particularly in DTM, and resolution mis-matches between image and DTM data, may sometimes dominate topographic normalization (e.g., Gu et al, 1998; Conese et al., 1993). Therefore, effort in considering these factors and reducing the data errors will help to maximize the potential of advanced topographic correction models.

3.7 SUMMARY

A terrain correction model, which preserves the sun-canopy-sensor (SCS) geometry, is proposed for removing the topographic effects on the TM images of forests. It normalizes the changes of sub-pixel-scale sunlit canopy area rather than the pixel-scale irradiance on various terrain slopes. The SCS model is as simple as the cosine correction model, but it has improved accuracy in removing topographic effects in forest images. It is comparable to or better than the c-correction and the Minnaert

correction models, which are also found to perform inconsistently from image to image.

CHAPTER 4: A STATISTICAL APPROACH FOR TOPOGRAPHIC CORRECTION OF SATELLITE IMAGES BY USING SPATIAL CONTEXT INFORMATION

4.1 INTRODUCTION

The brightness variation of visible, near-infrared (NIR), and short-wave-infrared (SWIR) satellite images in mountainous areas is dominated by topographic shading and shadowing. In many remote-sensing applications, these topographic effects are not desirable and need to be corrected before image interpretation. For high-resolution images, such as Systeme Pour l'Observation de la Terre (SPOT), Landsat Thematic Mapper (TM) and Multispectral Scanner System (MSS), removal of topographic effects requires a photometric function to characterize scene reflection and a co-registered digital terrain model (DTM) to calculate illumination geometry. General topographic correction models include the Lambert model (Smith et al., 1980) and the Minnaert model (Minnaert, 1941), which have found wide application (Meyer et al., 1993). Some specific models are also available for particular type of scenes, such as the SCS model (Gu and Gillespie, 1998), which was developed for topographic correction of forest images based on the sun-canopy-sensor (SCS) geometry. Other models are empirical or semi-empirical (e.g., Civco, 1989; Teillet et al., 1982). Although these models have different accuracy, they usually fit data well and remove most topographic effects, particularly for high-sun images of areas of low relief (Meyer et al., 1993). However, it is also observed that the brightness variation is not significantly reduced in many topographically corrected images (Meyer et al., 1993), particularly for low-sun images of rugged terrain. Since little residual topography is visible in the corrected images, the high contrast of brightness cannot be attributed to inaccuracy of the photometric function, and will probably not be reduced

by using more complicated scene reflection models, such as the BRDF's derived from either simulation or field data (e.g., Schaaf et al., 1994; Shoshany, 1993; Ranson et al., 1994).

It appears to have been overlooked that the failure of topographic correction may result from various simplifications and data errors involved in topographic correction (e.g., Conese et al., 1993; Civco, 1989; Proy et al., 1989). For example, the resolution and accuracy of DTM may have great impacts on topographic correction (Conese et al., 1993). It is reasonable to suspect that these errors will propagate into the corrected images, and may even be locally amplified, causing large brightness variations. Developing an approach to minimize the effects of these errors is thus a logical step to take in improving topographic correction.

Since topographic correction involves estimating reflectance from illumination geometry and radiance, both subject to errors, we must consider how these errors propagate into the estimate of reflectance. Conventionally, reflectance is estimated by using information at individual pixels only and thus prone to large errors due to the imperfect data. Such errors can be reduced if information in nearby pixels is also used, provided the scale of measurement is less than the scale of natural variability in the scene. Although we are not certain about the statistical properties of all the errors involved in topographic correction, we may assume that these errors are not strongly correlated spatially. If this is the case, the spatially averaged brightness and illumination geometry contain smaller errors, and the estimated average reflectance is more accurate than the estimate at a single pixel. Therefore, using spatial contextual information might reduce errors in topographically corrected images. Such an approach is called contextual topographic correction to distinguish it from the conventional, single-pixel method.

There are no published studies to justify a contextual approach to topographic correction, but successful applications of contextual information are common in other areas of image processing, for example, in cloud identification (Kittler and Pairman,

1985), agricultural classification (e.g., Zenzo et al., 1987) and forest mapping (e.g., Nel et al., 1994). These successes motivate the adoption of a contextual approach to topographic correction also.

In this chapter, a contextual topographic correction method is proposed and tested on a subset of the October 8, 1990, Landsat TM image of the Six Rivers National Forest in northern California. The errors associated with the satellite image, the DTM, and the registration of the data are evaluated and differentiated in 4.2. The method itself is formulated in section 4.3, which also contains a discussion of error propagation. Section 4.4 gives the results on the test image, including the magnitude and distribution of estimated reflectance variability, improvement of separability between different cover types, and the visual comparison of the corrected images. In section 4.5, discussions are focused on advantages and disadvantages of the contextual topographic correction. Finally, conclusions are made in section 4.6.

4.2 ERRORS RELATED TO TOPOGRAPHIC CORRECTION

Although local illumination geometry influences the basic pattern of radiance variation in satellite images, other factors also influence the apparent correlation between radiance and illumination geometry. As an example, the band-4 radiance of mature conifer forest on the TM test image is plotted with the cosine of incidence angle ($\cos \theta$) in Figure 4.1. The variation in the incidence angle is caused by topographic variation, and the cosine of incidence angle is used in this paper to describe the illumination geometry on a slope quantitatively. Larger values of $\cos \theta$ correspond to brighter slopes, the so-called sun-facing slopes, and smaller values correspond to darker slopes, slopes facing away from the sun.

Linear regression between the radiance and the cosine of incidence angle suggests that about 78% of the total variance correlates with topographic shading, but the scatter in this figure accounts for the other 22% percent of the variance. It is

important to understand where the scatter comes from because it will be the major source of variance in the topographically corrected image. Part of the scatter in Figure 4.1 is related to the natural variability within the vegetation community, i.e., the mature conifer forest, in the scene, but the rest must be attributed to a number of factors, including radiance measurement errors, DTM errors, registration errors, and local variations of elevation, environment and atmosphere. These factors introduce errors into the estimated irradiance, radiance and geometry and thus the applied photometric function in the general equation of radiation.

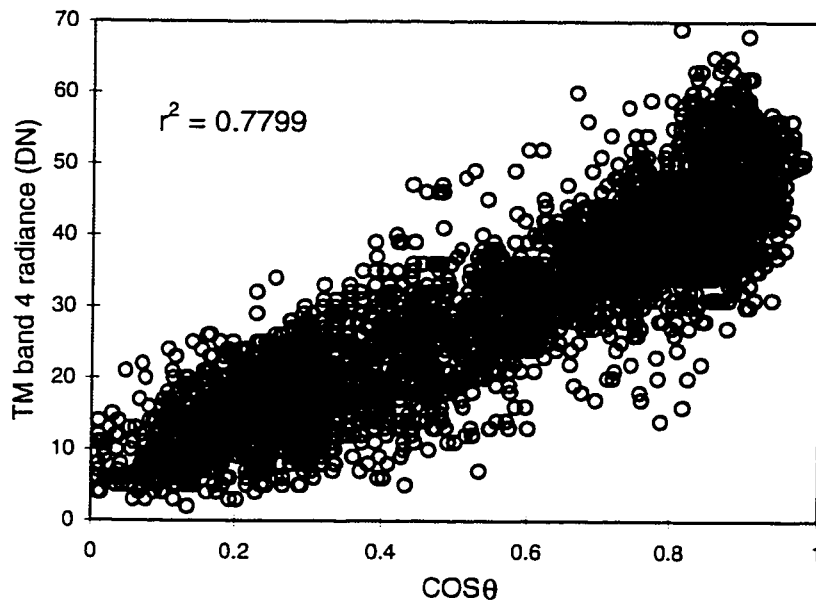


Figure 4.1 Scatter plot of radiance-geometry for a conifer stand (consisting of 3488 TM pixels). Notice the amount of scatter in this diagram is about the same for all slopes.

As a result, the observed radiance deviates from the model-predicted value which is calculated based on the photometric function with input of the estimated

geometry and irradiance. Let ε_g , ε_L , $\varepsilon_E E$, and ε_f represent the errors in illumination geometry (g), observed radiance (L), solar irradiance (E_S), and the photometric function (f), respectively, the observed radiance can be related to the true reflectance ρ_0 through

$$L - \varepsilon_L = \rho_0(E_S - \varepsilon_E E_S)[f(g - \varepsilon_g) - \varepsilon_f] \cos \theta / \pi. \quad (4.1)$$

where θ is the local solar incidence angle. Applying $f(g - \varepsilon_g) \approx f(g) - f'(g)\varepsilon_g$ and keeping only the zero- and first-order terms, we get

$$L = \rho_0 E_S f(g) \cos \theta / \pi - \rho_0 E_S [f'(g)\varepsilon_g + \varepsilon_f + f(g)\varepsilon_E] \cos \theta / \pi + \varepsilon_L. \quad (4.2)$$

If the error terms are omitted, (4.2) becomes the general equation for topographic correction by using photometric function $f(g)$. For clarity, the reflectance is re-scaled by letting $\rho_0 = \rho_0 E_S / \pi$ so that

$$L = \rho_0 f(g) \cos \theta + \varepsilon, \quad (4.3)$$

where ε is the residual of the fit or the difference between the observed and the model-predicted radiance,

$$\varepsilon = \varepsilon_L - \rho_0 [f'(g)\varepsilon_g + f(g)\varepsilon_E + \varepsilon_f] \cos \theta. \quad (4.4)$$

The residual depends not only on the accuracy of the photometric function, but also on the quality of data. The errors in illumination geometry, radiance, irradiance and photometric function are related to different sources, and specifically:

- 1) ε_E generally comes from the simplification that the solar irradiance on a pixel depends only on the solar incidence angle. This error results from the local variations of elevation and atmosphere condition, both of which will modulate the local intensity of solar irradiance at ground level (Meyer et al., 1993). Illumination from nearby hill slopes also adds local variability of total irradiance (Proy et al., 1989).
- 2) ε_g is the error in the estimated illumination geometry, resulted from errors in the DTM data (Conese et al., 1993). In addition, some misregistration of

the image to the DTM is inevitable and causes additional errors in the estimated geometry, particularly at pixels located near valley bottoms and mountain ridges.

- 3) ε_L includes the radiance measurement error and the variability in atmosphere path radiance.
- 4) ε_f represents the error in the photometric function, depending on the accuracy of photometric function.

Although the magnitudes and distributions of these errors are usually unknown for specific scenes, there is no reason to believe that the error in photometric function is always the major source of the residual of the fit. Consequently, the residual can not always be significantly reduced by using more accurate photometric models.

The value of the residual is apparently not measurable at individual pixels in most situations because the true reflectance is unknown. In fact, topographic correction models are usually evaluated from the RMS (root-mean squared) error of their fit to the data for a number of pixels selected from the same community in the scene. The RMS error, however, contains not only the deviations caused by the data errors but also the deviations caused by the real variability of reflectance from one pixel to another within the community in the scene. Therefore the RMS error itself is not sufficient to derive information on the magnitude of residuals at individual pixels.

On the other hand, it is important to differentiate the sources of scatter on a radiance-geometry diagram such as Figure 4.1 because only the scatter related to data errors will cause errors in the topographically corrected images. Although it is not possible to estimate the exact amount of scatter caused by the data errors, there are some qualitative features that permit an assessment of their relative significance comparing to the true reflectance variability. For example, if the scatter is caused only by natural variability of reflectance, the amount of scatter should be strongly correlated to topography because

$$L - \rho_0 f(g) \cos \theta = f(g) \varepsilon_\rho \cos \theta , \quad (4.5)$$

when dealing with perfect data, where ε_ρ denotes the natural variability of reflectance and is likely spatially-invariant within the community. Therefore, the scatter should be much stronger on the sun-facing slopes than on the slopes facing away from the sun because $f(g)$ is larger on the sun-facing slopes than on the slopes facing away from the sun. In contrast, if the scatter on a radiance-geometry diagram is mostly caused by data errors, it should not be strongly correlated with topography according to equation (4.4). (Precisely speaking, scatter related to ε_r , ε_L is not correlated with topography but are caused by ε_E and ε_f .) Instead, scatter should be correlated from one band to another and is proportional to the reflectance (except scatter caused by ε_L).

For this purpose, the residuals of the fit in TM bands 3, 4 and 5 DNs (digital number) for the same conifer stand are estimated for various topographic slopes (Fig. 4.2). From Figure 4.2 it can be observed that: 1) the standard deviations are not strongly correlated to topography, and their values on very dark slopes are not much smaller than that on sun-facing slopes; 2) the standard deviations in these bands vary with topography in a similar way, and are highly correlated. For example, the correlation coefficient is 0.95 between bands 4 and 5 (Fig. 4.3); and 3) the standard deviations increase from band 3 to band 5 to band 4, and their magnitudes are approximately proportional to the reflectance in these bands.

With above observations, it is concluded that data errors, rather than scene variability, are possibly the dominant source of scatter on the radiance-geometry diagram for the conifer stand in the test site. These errors will propagate into the estimated reflectance. Of all the errors, ε_L and ε_E are present in the satellite images when they are acquired, but they may be enhanced in topographically corrected images. ε_r and ε_f are additional errors introduced in topographic correction, and appear only on the corrected images. It could be very difficult to reduce these errors by

improving data quality or photometric function accuracy, therefore it is practically very desirable to find a way to minimize their effects in the corrected images.

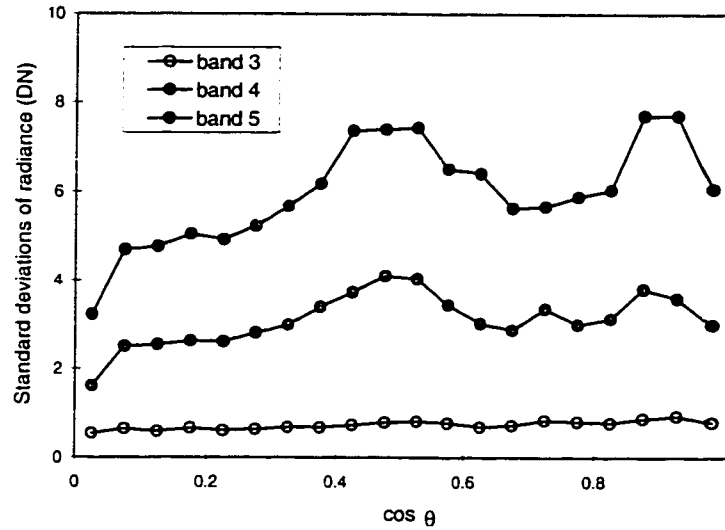


Figure 4.2 Standard deviations of TM bands 3, 4 and 5 radiance for the conifer stand on various slopes. Larger standard deviation corresponds to greater scatter on radiance-geometry diagram. Scatter is greater in band 4 than in band 5 and 3, but is not strongly correlated to topography.

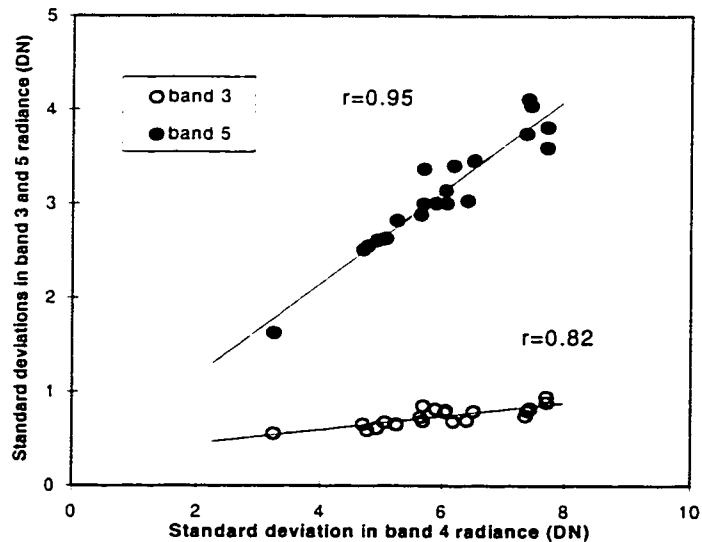


Figure 4.3 Correlation of the standard deviations in bands 3, 4 and 5 radiance. The strong correlation of standard deviations in different bands confirms that the scatter in these bands are more correlated to each other than to topography.

4.3 CONTEXTUAL TOPOGRAPHIC CORRECTION APPROACH

4.3.1 Formulation of the Contextual Approach

Conventionally, topographic correction has been made by normalizing the geometric term in equation (4.3) to estimate the reflectance

$$\hat{\rho}_1 = \frac{L}{f(g) \cos \theta}, \quad (4.6)$$

where $\hat{\rho}_1$ represents the reflectance estimated through “normalizing” the illumination geometry. If the residual in equation (4.3) is relatively small, the observed radiance will have a good correlation with the topography and the estimate by (4.6) will be close to the true reflectance. In practice, however, because the residual is usually significant, such estimated reflectance may greatly deviate from its true value. In the following, the approach based on equation (4.6) is referred as the conventional topographic correction approach because of its common use in the past.

Instead of the conventional “normalization” approach, it is also possible to compensate for the radiance difference caused by topographic shading to remove topographic effects. To illustrate this point, the radiance equation (4.3) is rewritten as

$$L = \rho_0 + \rho_0[f(g) \cos \theta - 1] + \varepsilon, \quad (4.7)$$

or equivalently

$$\rho_0 = L + \rho_0[1 - f(g) \cos \theta] - \varepsilon. \quad (4.7')$$

Therefore, neglecting the error term, the reflectance is simply

$$\hat{\rho}_2 = L + \rho_0[1 - f(g) \cos \theta], \quad (4.8)$$

where $\hat{\rho}_2$ represents the reflectance estimated through “compensating” the radiance by amount of $\rho_0[1 - f(g) \cos \theta]$. The true reflectance in the right side of equation (4.8), however, is unknown, so practically this approach is incomplete. To solve this problem, ρ_0 in (4.8) is approximated with a measurable variable, $\hat{\rho}_c$, such that

$$\hat{\rho}_2 = L + \hat{\rho}_c [1 - f(g) \cos \theta], \quad (4.9)$$

where $\hat{\rho}_c$ represents the reflectance used for measuring the amount of radiance required for compensation. There are variety of choices for defining $\hat{\rho}_c$, depending on specific requirements on corrected images. In two extremes, for example, $\hat{\rho}_c$ can be defined as either the average reflectance over the entire scene, or the reflectance at individual pixels estimated from the conventional approach. In the former case, the corrected image will show little contrast, only acceptable if the scene is relatively uniform. In the latter case, the “compensation” and “normalization” approaches lead to identical results and equation (4.9) degrades to the same form as in equation (4.6).

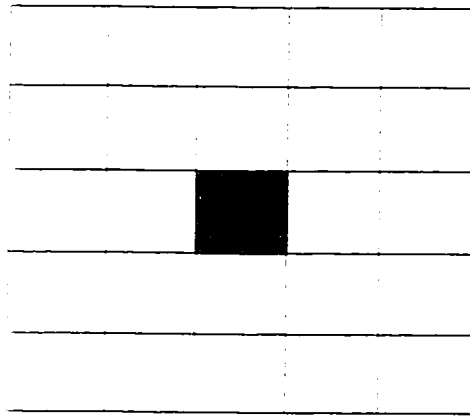


Figure 4.4 Spatial context of a pixel. Shown is a 5x5 square neighborhood of the center pixel (shaded). All the pixels in the square together consist of the spatial context of the center pixel. The size and shape of the spatial context of a pixel can be chosen according to image resolution, scene complexity, and data quality in practice.

In between, $\hat{\rho}_c$ may be defined as the local reflectance estimated from the information within the spatial contexts of individual pixels. To be specific, the spatial context of a pixel consists of all of its neighboring pixels which are within a specified distance from the pixel. For example, Figure 4.4 shows a 5x5 pixel, square-shaped

spatial context of the center pixel. The local reflectance for each pixel is then estimated from the radiance and geometry information on all pixels within its spatial context. The larger the spatial context is set, the more the “smoothing” effect will be. However, as long as the size of communities in the scene is larger than the spatial context, the local reflectance is expected to be a good approximate to the reflectance at individual pixels, with obvious exceptions at community perimeters.

4.3.2 Estimation of $\hat{\rho}_c$

With the spatial context predefined according to image resolution and scene complexity, the local reflectance can be simply estimated from

$$\hat{\rho}_c = \frac{\sum_{i=1}^N L_i}{\sum_{i=1}^N \cos \theta_i f(g_i)}, \quad (4.10)$$

where N is the total number of pixels in the spatial context and L_i and g_i are radiance and geometry at pixel i , respectively. If the errors in L and g are not highly correlated from pixel to pixel, $\hat{\rho}_c$ will be less affected by data errors than the reflectance estimated from equation (4.6) at individual pixels. Equation (4.10) can be refined if the spectral data on uncorrected images is used to identify community boundaries. Among all the pixels in the spatial context of a pixel, if $\hat{\rho}_c$ is estimated from information only on those with spectra similar to the spectrum of that pixel, it will better represent the true reflectance at that pixel. Using spectral information, the refined estimate of $\hat{\rho}_c$ is in general given by

$$\hat{\rho}_c = \frac{\sum_{i=1}^N w_i L_i}{\sum_{i=1}^N w_i \cos \theta_i f(g_i)}, \quad (4.11)$$

where the weight w_i for the i th pixel can be generally defined as

$$w_i = \cos(L_i, L). \quad (4.12)$$

Since the spectral shape is roughly independent of topography, in spectral space the directional difference (direction cosine) of two spectra in equation (4.12) is more

reliable than their distance in measuring their similarity. Here the weights in equation (4.11) are defined as

$$w_i = \begin{cases} 1 & \text{if } \cos(L_i, L) \geq S_0 \\ 0 & \text{otherwise} \end{cases}, \quad (4.13)$$

for simplicity, where S_0 ($0 \leq S_0 \leq 1$) is preset to define similar spectra quantitatively.

To interpret the local reflectance, $\hat{\rho}_c$, equation (4.3) is substituted into equation (4.11) to obtain

$$\begin{aligned} \hat{\rho}_c &= \frac{\sum_{i=1}^N w_i [\rho_i f(g_i) \cos \theta_i + \varepsilon_i]}{\sum_{i=1}^N w_i \cos \theta_i f(g_i)} \\ &= \hat{\rho} + \frac{\sum_{i=1}^N w_i \varepsilon_i}{\sum_{i=1}^N w_i \cos \theta_i f(g_i)} \end{aligned}, \quad (4.14)$$

where $\hat{\rho} = \frac{\sum_{i=1}^N w_i f(g_i) \cos \theta_i \rho_i}{\sum_{i=1}^N w_i \cos \theta_i f(g_i)}$ is the weighted (by $w_i \cos \theta_i f(g_i)$) average reflectance in the spatial context. The second term on the right side of this equation represents the average residual error of the fit. Without considering the error term in equation (4.14), $\hat{\rho}_c$ is just the reflectance averaged over all pixels within the spatial context, weighted according to their geometry and spectral shapes. Specifically, the pixels with similar spectra, located on bright slopes, mostly determine the value of $\hat{\rho}_c$. This is desirable, because the information from the less-shaded bright slopes is more reliable than from dark slopes and spectral similarity indicates possibly similar reflectances.

Of course, the weights used in estimating $\hat{\rho}_c$ can be defined based on other information. For example, the normalized difference vegetation index (NDVI) is widely used in differentiating land cover types. Spectral mixture analysis (e.g., Sabol et al., 1992) also provides a powerful tool for understanding surface composition. Occasionally, in-situ spectral measurements might be available. Such additional

information can all be used to obtain an estimate of $\hat{\rho}_c$ close to the true reflectance at individual pixels.

4.3.3 Error Propagation in the Contextual Approach

The objective of the contextual approach is to reduce errors in comparison to the conventional approach on the topographically corrected images. Such errors in the conventionally corrected images can be estimated by substituting equation (4.2) into (4.5) to get

$$\Delta_1 = \hat{\rho}_1 - \rho_0 = \frac{\varepsilon}{f(g)\cos\theta}, \quad (4.15)$$

where Δ_1 represents the error in the reflectance estimated with the conventional approach. Although $\cos\theta$ increases from 0 on completely shadowed slopes to 1 on brightest slopes, the residual of the fit (ε), however, does not strongly depend on topographic slopes as we have seen in Figure 4.2. Consequently the error in such corrected images, Δ_1 , is expected to be: 1) larger than the residual of fit (ε); 2) not uniform, i.e., larger on dark slopes than on bright slopes and 3) extremely large on severely shaded slopes where $\cos\theta \approx 0$.

Similarly, the error in the reflectance estimated with the contextual approach, Δ_2 , is found by substituting equation (4.6) into (4.9)

$$\Delta_2 = \hat{\rho}_2 - \rho_0 = \varepsilon + (\hat{\rho}_c - \rho_0)[1 - f(g)\cos\theta]. \quad (4.16)$$

Or applying equation (4.14) to get

$$\Delta_2 = \varepsilon + \frac{1 - f(g)\cos\theta}{\sum_{i=1}^N w_i \cos\theta_i f(g_i)} \sum_{i=1}^N w_i \varepsilon_i + (\hat{\rho}_c - \rho_0)[1 - f(g)\cos\theta]. \quad (4.17)$$

Therefore, errors in images corrected with the contextual approach come from three sources:

1) ε , the residual of the fit. This error is related to original images, DTM data and models used in topographic correction. Its reduction requires higher quality of data and more accurate photometric function models, neither of which is practical. However, the error related to ε is not exaggerated as in the conventionally corrected images.

2) $\sum_{i=1}^N w_i \varepsilon_i$, the weighted average residual of fit in the spatial context. It is related to the error in the estimated local reflectance (equation (4.14)). Since it is assumed that ε is spatially not strongly correlated, $\sum_{i=1}^N w_i \varepsilon_i$ over the spatial context of individual pixels will generally be reduced in proportion to the size of the spatial window. The magnitude of the related error in the corrected images is further controlled by a geometric term, $1 - f(g)\cos\theta$, so that the error due to $\bar{\varepsilon}$ is mostly limited to dark slopes where $f(g)\cos\theta \approx 0$. On bright slopes, $f(g)\cos\theta \approx 1$, and this error is negligible.

3) $\hat{\rho} - \rho_0$, the reflectance variation in the scene. It causes additional error in the estimated reflectance because the radiance is compensated according to the weighted average reflectance in the spatial contexts, instead of the reflectance at individual pixels. For pixels near community boundaries, the spatial contexts are mixed with pixels from different communities and cause the estimated $\hat{\rho}_c$ to deviate from the average reflectance of either community. As a consequence, the corrected images will show some blurring along community edges. This effect, certainly undesirable, is the major disadvantage of the contextual approach. For this reason the spectral information is used here to locate community boundaries and weight individual pixels as in equation (4.12). There is also a smoothing effect among pixels within pure communities, but it is not as obvious because the reflectance variation is not as strong within uniform communities. In addition, such smoothing effect may be

helpful in some applications because it reduces within-community reflectance variation and improves the separability among various communities. Similar to $\sum_{i=1}^N w_i \varepsilon_i$, the resulting error in corrected images is also limited to dark slopes, and is negligible on bright slopes.

Although the contextual approach has additional error sources because of the substitution of $\hat{\rho}_c$ for ρ_0 in equation (4.9), the total error in the corrected images is expected to be reduced in comparison to the conventional approach. The ratio of the errors from these two approaches is

$$\frac{\Delta_2}{\Delta_1} = f(g) \cos \theta + \left[\frac{\sum_{i=1}^N w_i \varepsilon_i}{\sum_{i=1}^N w_i \cos \theta_i f(g_i)} + (\bar{\rho} - \rho_0) \right] f(g) \cos \theta [1 - f(g) \cos \theta] / \varepsilon. \quad (4.18)$$

First, the errors are about the same with two approaches on bright slopes, where $f(g) \cos \theta \approx 1$. Second, the ratio goes to zero on dark slopes, where $f(g) \cos \theta \approx 0$, implying that errors on dark slopes have been greatly reduced by the contextual approach. Finally, on intermediate slopes, the error ratio depends on the magnitude of the residual of the fit. The error is reduced if the residual of the fit is larger than the natural scene variability but increased otherwise. Since there are so many factors involved, including image and data quality, scene complexity, and imaging conditions, both approaches may have advantages over the other under particular circumstances.

4.4 APPLICATION RESULTS

The contextual topographic correction approach has been tested on a 240×170 pixel subset of TM image that covers a coniferous forest. The widely used Lambert and Minnaert models, together with the SCS model which was developed especially for forested scenes (Gu and Gillespie, 1998), were used in different attempts with conventional topographic correction.

The SCS model was used in the contextual approach because it was found to fit the test data better than other two models (Gu and Gillespie, 1998). The spatial context of a pixel was defined as the 9×9 pixel square centered at that pixel. Within the spatial context, only the pixels with similar spectra, yielding $\cos(L_i, L) \geq 0.95$, were used to estimate $\hat{\rho}_c$. Only bands 3, 4 and 5 were chosen as representatives to examine the topographic effects and corrections for the visible, NIR and SWIR bands of TM images.

4.4.1 Variance Analysis

Similar results are obtained for each of the examined TM bands but, for clarity, only results in band 4 are displayed. Figure 4.5 compares the reflectance for the conifer stand estimated by using the conventional and the contextual approaches, both employing the SCS model. Clearly, the reflectance estimated with the conventional approach shows more scatter, which increases from sun-facing slopes to shaded slopes. In contrast, the reflectance variation on the shaded slopes has been significantly reduced to about the same level as on the bright slopes with the contextual approach (Fig. 4.5).

Because different topographic correction models likely lead to different estimates of mean reflectance (Gu and Gillespie, 1998), the mean-normalized standard deviations have been used to measure the variability of reflectance estimated by using different models and approaches. As shown in Figure 4.6, each curve depicts the variation of reflectance variability with topography. It is observed: 1) the variability of the reflectance estimated by the conventional approach, using different photometric functions, shows only slight differences; 2) In general., the variability rises from 0.13 to above 0.60 as the incidence angle increases from 0 to 90° , several times larger on the shaded slopes than on the bright slopes; and 3) the reflectance estimated by the

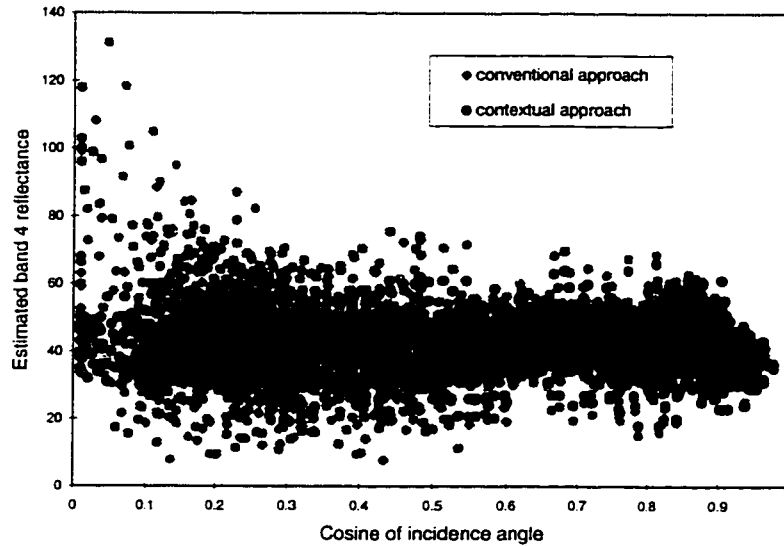


Figure 4.5 The estimated band 4 reflectance distributions for the same conifer stand as in Figure 4.1. The reflectance estimated with the conventional approach (gray solid circles) shows much more scatter than with the contextual approach (black solid circles).

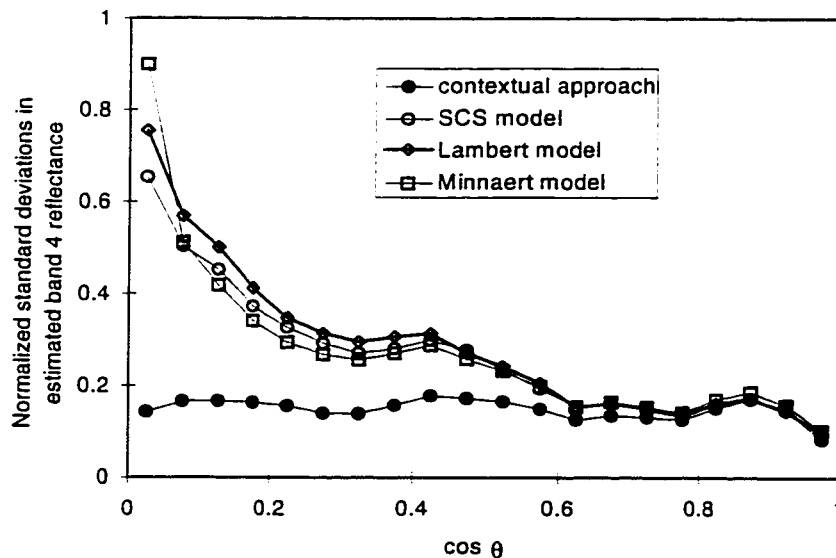


Figure 4.6 Comparison of the variability of reflectance estimated with different methods. The contextual approach produces more uniform reflectance estimates over various slopes, but the conventional approach causes much larger variability on shaded slopes than on sun-facing slopes, for all three tested photometric functions.

contextual approach is more homogeneous and topography-independent, with lower normalized standard deviations (0.13-0.18) than by the conventional approach.

The overall variability of estimated reflectance for all three bands was also calculated and summarized in Table 4.1. The last row in Table 4.1 gives the mean-normalized standard deviations of radiance on the brightest slopes ($\cos\theta \geq 0.95$), which approximately characterize the “true” levels of the natural scene variability (they are in fact equivalent to the total variability of reflectance caused by the natural scene variability and the errors in the image and the DTM). The overall variability of the estimated reflectance before topographic correction is very large (about 0.45) in all three bands. After the conventional topographic corrections, it has been significantly reduced but is still higher than the “true” variability. For example, for the SCS model, the variability is still higher by about 27%, 67% and 76% of the “true” variability in bands 3, 4 and 5, respectively. In contrast, the variability has been reduced by the contextual approach to about the same level as the “true” variability inferred from the data. Smoothing has obviously occurred in the contextual approach because the variability in bands 4 and 5 is slightly lower than the corresponding “true” values. However, because smoothing can only occur on dark slopes, the fact that variability remains about the same for all topographic slopes (Fig. 4.5 and 4.6) suggests the smoothing effect insignificant.

Table 4.1. Normalized standard deviation of the estimated reflectance for a conifer stand in the test site.

	Band 3	Band 4	Band 5
without correction	0.45	0.44	0.46
Lambert model	0.35	0.28	0.33
Minnaert model	0.33	0.27	0.31
SCS model	0.33	0.25	0.30
contextual approach	0.28	0.15	0.17
“true” variability	0.26	0.16	0.18

4.4.2 Visual Examination of Corrected Images

Figure 4.7 displays the test and terrain-corrected TM band 5 images. The topography is apparent on the uncorrected image (Fig. 4.7a), which shows dark shadows on steep northwestern slopes because of the low sun position (37.5° elevation). Variation in brightness is largely related to topography throughout the image, and provides little information regarding to the land cover types. For example, brighter features (e.g., clearcuts) in northwestern slopes are confused with darker features (e.g., forest) on the southeastern slopes because they have similar apparent brightness in the uncorrected image. Therefore, it is necessary to correct the topographic effects in the image in order to extract from it reliable information.

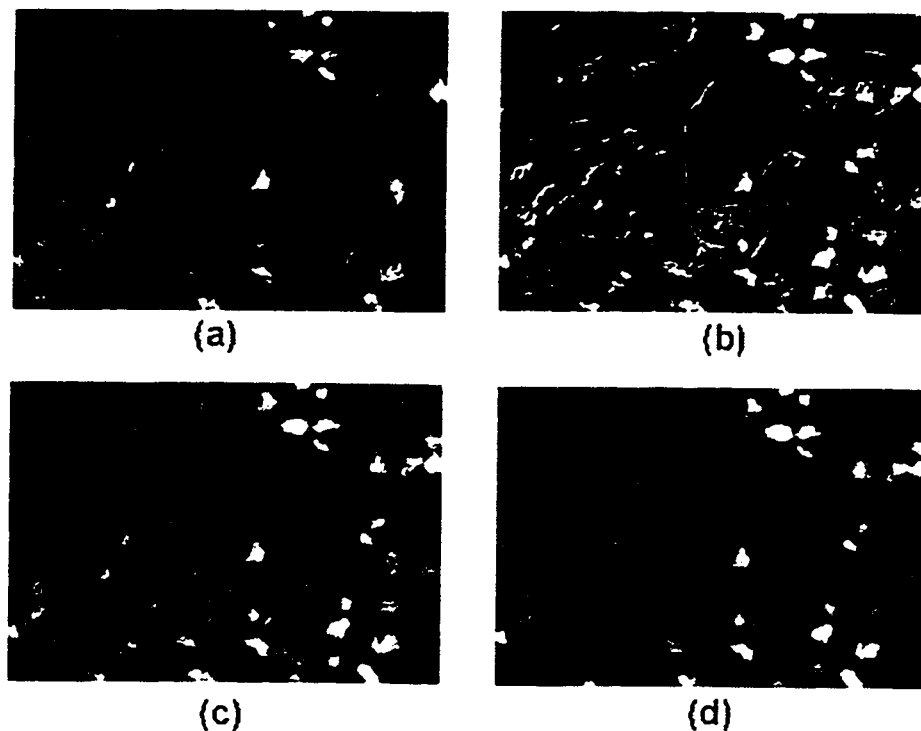


Figure 4.7 Band 5 TM images of the test site. (a) uncorrected; (b) conventionally corrected; (c) contextually corrected and (d) spatially filtered version of image (b). The image is 240×170 pixels.

There is no apparent topography in average on the conventionally corrected image (Fig. 4.7b), but the northwestern slopes appear to be “noisier” and show different textures from the southeastern slopes. The unrealistic high variability on the northwestern slopes will limit the accuracy of land cover type differentiation in spectral classifications, and possibly result in unreal classes in textural classifications. The contextual correction approach has produced an image which subdues abrupt tone variations from slopes facing the sun to slopes facing away from the sun (Fig. 4.7c). The fine textures are generally continuous and not abruptly interrupted across ridges and valleys, which is one of the characteristics on the conventionally corrected image (Fig. 4.7b). It is also encouraging that all boundaries between forest and non-forest communities are well preserved because of the high spectral contrast. The boundaries between different forest communities, however, are well preserved only on the sun-facing slopes. Some blurring occurs on northwestern slopes, and the amount of blurring is dependent of the spectral contrast between neighboring communities. In general, the smoothing effect is not apparent. This is a great advantage over the simple spatial filtering which is widely used to remove speckle or random noise in images. For example, when the weighted average filter of the same size (9×9) is applied to the conventionally corrected image, the resulting image (Fig. 4.7d) appears out of focus and most of the fine textures disappear, although edges between forest and non-forest still stand out because the weighted filtering was actually not applied along these boundaries of high spectral contrast. Therefore, the errors amplified in the conventionally corrected images can not be easily “removed” by simple spatial filtering.

4.4.3 Impacts on Classification Accuracy

Improved classification accuracy is one of the most important reasons for topographic correction, and it would be convincing evidence supporting one particular topographic correction over the others (Itten and Meyer, 1993). In the test scene are

four main cover types: mature and old-growth Douglas fir-hardwood communities, pole-stage conifers replanted after logging, hardwood-dominated communities in areas burned in the last century, and recent clear cuts. With forest survey data provided by the Six Rivers National Forest, four classes in the test site were defined: 1) mature/old-growth Douglas fir-hardwood stands (MO); 2) older pole-stage conifers (OP), replanted between 1965-1971; 3) younger pole-stage conifers (YP), replanted between 1976-1981; and 4) recent clearcuts (CC), replanted after 1985. At least 1000 pixels were identified for each of the four classes, which are distributed over a wide range of slopes. These pixels were classified using a maximum likelihood algorithm (Foody et al., 1992) to assess the separability among the four classes on the uncorrected, conventionally and contextually corrected images, respectively. Because the spectral means and variances used in the algorithm were estimated from the same pixels, the classification results only indicate how well the four classes are spectrally separable.

The results (Table 4.2) show that the overall classification accuracy was improved from 66.7% in the uncorrected image to 79.3% in the conventionally corrected image and 88.1% in the contextually corrected image, respectively. The SCS model was used in both approaches. Without any topographic correction, the brightness is mostly controlled by topography and separation of different communities largely relies on their color difference (Fig. 4.8a). By normalizing illumination geometry, the conventionally corrected image is directly related to ground reflectance, which is independent of topography, and the overall classification accuracy is improved (by 12.6%). The large errors in the corrected image, however, have limited the improvement since all classes show strong variability and form large clusters in the spectral space, resulting large overlaps among the classes (Fig. 4.8b). In the contextually corrected images, however, the errors are reduced so that each class corresponds to a denser cluster and the overlap among clusters is smaller (Fig. 4.8c). Therefore, although the means of different classes are separated at about the same

distances, the smaller variances lead to better and thus higher classification accuracy in the contextually corrected image than traditionally corrected image.

Table 4.2a. Classification accuracy in uncorrected image

class \ classified	MO	OP	YP	CC	total	accuracy
MO	999	142	1	0	1142	87.5%
OP	546	424	117	3	1090	38.9%
YP	183	206	709	99	1197	59.2%
CC	9	5	183	865	1062	81.5%
total	1737	777	1010	967	4491	
user's accuracy	57.5%	54.6%	70.2%	89.5%		66.7%

Table 4.2b. Classification accuracy in conventionally corrected image

class \ classified	MO	OP	YP	CC	total	accuracy
MO	1015	108	19	0	1142	88.9%
OP	130	789	165	6	1090	72.4%
YP	42	219	806	130	1197	67.3%
CC	2	3	107	950	1062	89.5%
total	1189	1119	1097	1086	4491	
user's accuracy	85.4%	70.5%	73.5%	87.5%		79.3%

Table 4.2c. Classification accuracy in contextually corrected image

class \ classified	MO	OP	YP	CC	total	accuracy
MO	1117	25	0	0	1142	97.8%
OP	6	976	105	3	1090	89.5%
YP	11	193	893	100	1197	74.6%
CC	0	0	92	970	1062	91.3%
total	1134	1194	1090	1073	4491	
user's accuracy	98.5%	81.7%	81.9%	90.4%		88.1%

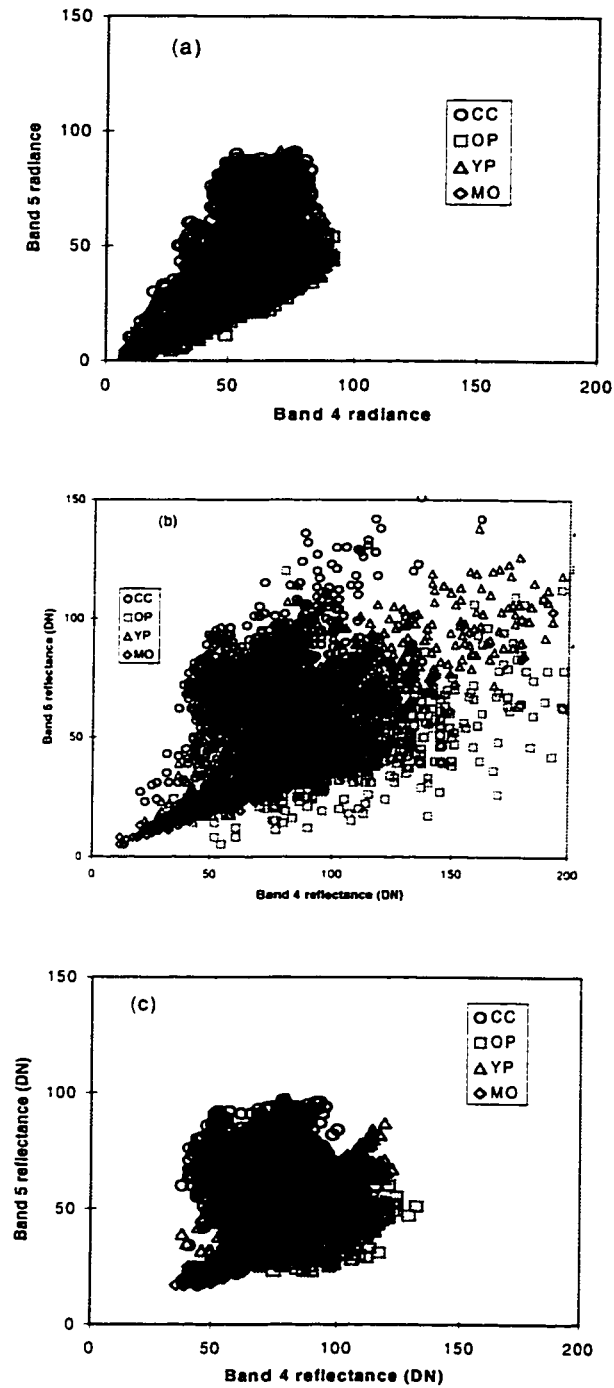


Figure 4.8 Spectral clusters of the four classes identified in the test site on uncorrected (a), conventionally corrected (b), and contextually corrected (c) images, respectively. Overlaps between different clusters are decreasing from (a) to (b) to (c).

For individual classes, the classification accuracy was improved by different amounts after terrain corrections (Fig. 4.9). For example, most of the older pole-stage conifer(OP) pixels were mis-classified as MO and YP in the uncorrected image, yielding an accuracy of only 38.9% (Table 4.2a). It is improved to 72.4% in the conventionally corrected image (Table 4.2b) and further improved to 89.5% in the contextually corrected image (Table 4.2c). But in comparison, the accuracy for identifying the recent clearcuts (CC) was not improved as much, about 8% and 9.8% respectively in the conventionally and contextually corrected images. Before terrain correction, these classes were mostly differentiated based on their spectra. More soil is exposed in recent clearcuts than forests of different ages, resulting relative higher reflectance in band 5 and making this class differentiable (with accuracy 81.5%) from others even without terrain correction (Table 2a). Spectra of older pole-stage conifers, however, mimic closely to those of mature/old growth, making OP much less identifiable based on spectral information only (Figure 4.8a). On the other hand, the OP class has higher albedo than the MO community so that they are well separable based on reflectance information on the terrain-corrected images (Figure 4.8 b and c).

When different photometric function models were applied for the conventional terrain correction, similar accuracy was achieved (Fig. 4.9). For example, the overall classification accuracy was 77.6% when using the Lambert model and 78.5% the Minnaert model, respectively. The accuracy differences (1-2%) with different photometric functions are insignificant in light of the ~9% improvement achieved with the contextual approach. Although these numbers are likely case-sensitive, they suggest the potential improvements achievable with the contextual topographic corrections.

4.5 DISCUSSION

The contextual topographic correction approach differs from the conventional, single-pixel-based approach largely in that it incorporates spatial contextual

information to compensate the illumination differences on various terrain slopes. It has the potential to reduce the errors in the corrected images resulted from the imperfection of data. The contextually corrected images, however, may appear to be smoothed with blurred community edges, and this is a drawback to the method. Therefore, whether the contextual or conventional approach has more advantages over the other is generally dependent of specific applications. For example, the contextual approach may be more appropriate for removing terrain effects in low-sun images of rough terrain with a DTM of poor accuracy and low resolution. On the other hand, the conventional approach may be more suitable for high quality data.

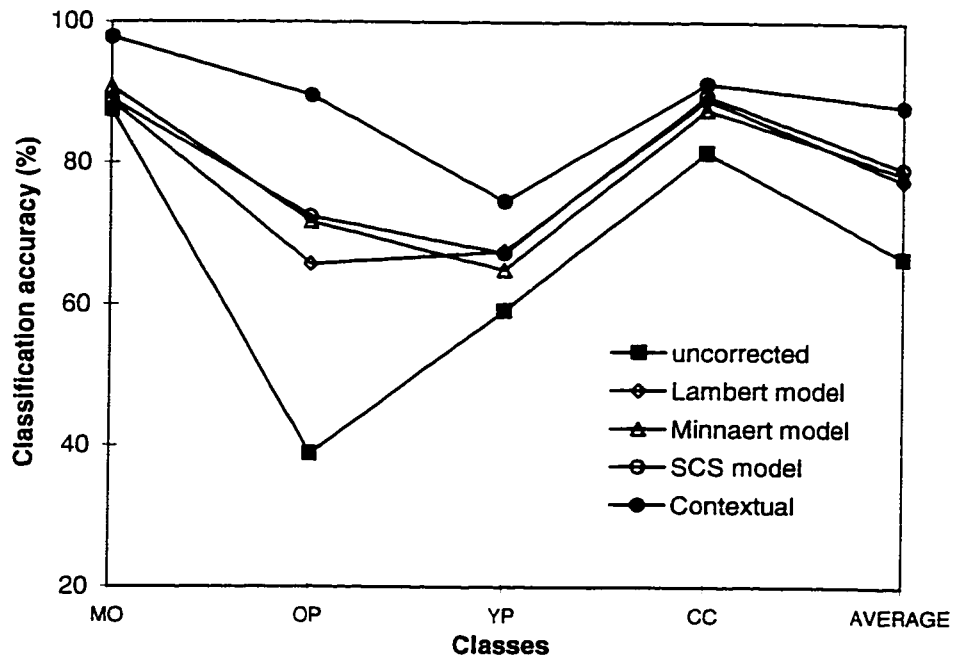


Figure 4.9 Classification accuracy improvements on the contextually corrected images. Classification accuracy was improved in conventionally corrected images in comparison to the uncorrected image, with similar magnitudes when using three different photometric functions. But the best classification was achieved in the contextually corrected image, yielding highest accuracy for all classes.

The contextual topographic correction approach is very flexible and capable of balancing error reduction and smoothing simply by varying the size of spatial context (neighborhood). In case errors are large and of major concern in the corrected images, a larger context can be defined to include more pixels. On the other hand, if data quality meets the accuracy requirements for specific purposes, smaller spatial contexts can be used to reduce the smoothing effects. As stated in Section 4.3, the conventional approach is just a contextual approach that uses the smallest size (1×1) of spatial context, which includes only the pixel to be corrected. Therefore, to take the advantage of the contextual approach, one key is to choose the size of the spatial context properly. Although it is not intended here to put any specific rules, the size of spatial context should in general be constrained to resolve the smallest mapping communities in the scene. Therefore, image resolution, scene complexity, and data quality all should be considered in choosing the size of the spatial context.

The contextual approach recovers more information loss due to topographic shading and shadowing, an inevitable result of measurement errors and data quantification. Since the errors are likely at the same level throughout the image, the lower radiance implies lower signal-noise ratios and more information loss on shaded slopes (Conese et al., 1993). The conventional approach fails to improve the signal-noise ratio on the shaded slopes since both radiance and noise are simultaneously “normalized.” As a consequence, the signal-noise ratio is not uniform, lower on slopes facing away from the sun than on sun-facing slopes, in the corrected images although they may appear to be free from topographic shading in average. The contextual information, however, is much less affected by such errors and thus “adds” signal to the shaded slopes during contextual compensation. In addition, the contextual information is added exactly according to the amount of information loss and, the more information lost to shading, the more decisive the contextual information will be. Therefore, the lost information is recovered more, and the signal-noise ratio is about the same throughout the corrected image.

Sub-pixel-scale mixing between adjacent communities along community boundaries occurs in all images. In addition, real optical systems collect energy not only from the specific scene element but also, in smaller amounts, from adjacent elements (Justice et al., 1989). Finally, not all natural community boundaries are sharp at the image scale. Therefore the transition from one community to another is usually not precisely defined on satellite images and may even extend through a few pixels. Although blurring is inevitable near community boundaries in contextually corrected images, it can be reduced by calculating $\hat{\rho}_c$ from spectrally weighted information in the spatial context, particularly along boundaries between communities of high spectral contrast. We need to be aware of the blurring effects, but they may not add noticeable ambiguities in discerning community edges in some situations. Otherwise we need to reduce the size of spatial context to control such blurring.

DTM records ground elevation rather than elevation of vegetation canopy, which actually determines the terrain effects in forest. Therefore the illumination geometry estimated from DTM is only approximately related to terrain effects, considering the variability of canopy heights. Particularly if canopy heights of adjacent communities differ greatly, such as clearcuts and old-growth, shadowing/high-lighting unrelated to topography will occur near these community boundaries. In such cases, even if a good correlation between DTM and satellite images is achieved over a large area, locally image brightness may be poorly correlated to DTM.

Considering the improvements in classification accuracy achieved in the test image with the contextual approach over the conventional, single-pixel-based topographic correction method, it is worthwhile to pay more attention to data errors and their effects in the corrected images. Developing more precise scene reflection models, for instance as done by Schaaf et al. (1994), is very important to improve understanding of terrain effects on satellite images. From the remote-sensing application point of view, however, it may be even more important to characterize and

minimize the most significant sources of errors in the corrected images. The contextual topographic correction approach is just one step in this direction. Although this approach reduces the effects of various errors in topographic correction, it does not remove them. More effort is needed to improve data quality of the DTM and satellite images, as well as the registration so that corrected images contain less errors and allow better scene characterization.

4.6 CONCLUSION

A contextual approach for correcting topographic effects on the radiometry of satellite images has been proposed and tested. To compensate for illumination variation on various topographic slopes, the approach uses information extracted from the spatial context of individual pixels. The advantage over the conventional pixel-based approach, which normalizes the lighting geometry based simply on the information at individual pixels, arises because such information has been deteriorated by various errors associated with the acquisition and co-registration of the image and DTM, particularly on the severely shaded slopes. As a result, more information on the shaded slopes, otherwise lost, has been recovered as the signal-noise ratio is improved.

The contextual approach is inherently subject to blurring, but this can be minimized by detecting community boundaries with spectral information. In this way, sharp community boundaries may be preserved except those between communities of low spectral contrast on severely shaded slopes. As the within-class variability is reduced, different cover types are more accurately differentiated on the contextually corrected images.

Although the proposed topographic correction approach has been examined only on a single Landsat TM image of one forest site, the correction should be similarly applicable for other satellite images. Its improvement over the traditional approach depends in part on the specific sensor system and imaging conditions, the available DTM accuracy, and terrain roughness and illumination conditions. The

contextual terrain correction method has the potential to improve the performance of remote-sensing analysis, especially over mountainous areas.

CHAPTER 5: A MULTI-SCALE TEXTURAL CLASSIFICATION ALGORITHM FOR INTERPRETATION OF SATELLITE IMAGES

5.1 INTRODUCTION

Classification is a major step in image interpretation, which links individual pixels in the satellite image to meaningful identities. By this procedure, the satellite measurements, usually radiance, are converted to information maps about land-cover types and surface composition on the ground. Such information can either be directly used by users or become the basic input for a database for reference. The fundamental basis for image classification relies on the spectral contrast between different classes that exhibit variations in brightness and/or color in satellite images. Spectral information alone may not be sufficient for the reliable separation of different land-cover types, however, because they may have similar spectra. In forest mapping, for example, the spectral differences between different forest communities are very subtle and spectrum-based forest mapping usually does not achieve the expected accuracy (e.g., Foody and Hill, 1996; Nel et al., 1994).

Recently, contextural and textural classification schemes have been highly favored for processing satellite images (e.g., St-Onge and Cavayas, 1997; Nel et al., 1994; Zenzo et al., 1987; Franklin et al., 1986; Kittler and Parman, 1985). The simple reason behind such efforts is that the spatial correlation in satellite images may reveal important information about the characteristic structures of different classes on the surface (e.g., Wudler et al., 1998; St-Onge and Cavayas, 1995). Incorporating such information is thus expected to improve the classification accuracy because spectrally similar classes may be very different in structure. This scenario is more likely to work

in high-resolution images because they will resolve surface structures better than low-resolution ones.

The spatial information can be used in image classification in two different ways, resulting two major categories of classifiers: contextural classifiers and textural classifiers. Contextural classifiers generally assume some kind of statistical models (e.g., a Markov Random Field, or MRF) to describe the spatial correlation of the ground "truth," and to localize the *prior* probability distribution required in statistical classification (e.g., Bouman and Shapiro, 1994; Besag, 1986; Kittler and Pairman, 1985; German and German, 1984). The contextural approach is mostly successful in classifying noisy images, or in image restoration (e.g., Besag, 1986). The major problem associated with the contextural approach is model justification: how to validate a parameterized statistical model to describe the distribution of ground truth. Estimation of model parameters can also be problematic because they usually have significant impacts on the accuracy and appearance of the final classification map (Besag, 1986). In addition, the ground "truth" has to be simultaneously estimated from the data, which may lead only to local, instead of supposed global, optimization. It is also disadvantageous for the statistical approach to handle scenes composed of units with various spatial scales.

The textural classifiers, on the other hand, estimate local statistical properties, the so-called textures, such as mean, variance and skewness, to characterize different classes (e.g., Nel et al., 1994; Lee and Philpot, 1991; Stormberg and Farr, 1986; Irons and Peterson, 1981; Haralick and Shanmugam, 1974). These statistical properties are treated as additional image "bands," and are used together with the original spectral data for image classification. One advantage of the textural approach is that the textural features, and thus the original data, are used directly and explicitly. With the textural classifiers, however, problems arise both with estimating the high-order statistics and with using them in an appropriate way. Practically, it is difficult to validate the extracted textural features as being truly related to individual classes. As a

matter of fact, false or unrealistic textures will always appear along unit boundaries (Tomia and Tsuji, 1990). Therefore, it is critical in the textural approach to identify unit boundaries, in order to avoid the artifactual textures which are not related to surface structures. Another problem related to the textural approach is how to use the extracted textural information in a statistical classification frame effectively, because textures are difficult to characterize well with a statistical distribution. In general, textural approaches, such as “region-growing” and “region-splitting” methods (Tomia and Tsuji, 1990), require a lot of experience and knowledge to implement for computer automation.

Because the contextual approach is best at handling multi-band (including textural bands) information and the textural approach at characterizing structural features, it is desirable to develop a hybrid algorithm that exploits their advantages while avoiding their drawbacks. With such an algorithm, the textural information can be extracted and used in a solid statistical framework together with the spectral information for separating spectrally similar classes. For this purpose, a multi-scale textural classification (MSTC) algorithm is developed here for classifying satellite images. In the following sections, the algorithm is derived and tested.

5.2 CHARACTERISTICS OF SATELLITE IMAGE CLASSIFICATION

Satellite image classification identifies land-cover classes with intrinsic variability, i.e., the natural scene variability. For example, a land-cover class may exhibit significant spectral variations from one location to another across the image. In comparison to the natural variability, the spectral scatter related to noise may be small, for example, 1-2 DN's (John Adams, pers. comm., 1998). Land-cover classes are generally defined in the scene according to average scene compositions over a relatively large spatial domain at characteristic scales (e.g., Lambin and Strahler, 1994; Hall et al., 1991). Such defined classes are usually characterized by following features:

1. they are directly related to field observations or common experiences;
2. they are explicitly or implicitly defined at certain spatial scales; and
3. they are meaningful to users.

To identify land-cover classes in satellite images, therefore, one needs to examine not only the spectral values of individual pixels, but also the spatial patterns or textures of spectral variation from pixel to pixel (e.g., Fung and Chan, 1994). Only with both the textural and spectral information can land-cover classes be completely described and thus accurately differentiated in satellite images.

The spatial scales for defining the field classes likely vary for different classes because of the complexity of natural and human-impacted surfaces (e.g., Lambin and Strahler, 1994; Woodcock and Strahler, 1987). For example, rivers are elongate in spatial extension, while timber harvesting often results in patches on landscapes. Knowledge of spatial scales is very valuable in manual interpretation of satellite images, and could also be utilized in computerized classification to improve mapping accuracy. The MSTC algorithm will include such knowledge as an input.

It is usually necessary to make certain assumptions to simplify classification algorithms. Here the key assumptions in deriving MSTC are listed and evaluated based on the specific characters of satellite images and their interpretation:

Assumption 1: if a pixel is from a particular class, it must fall into a pixel block, within which all pixels are from the same class. Thereafter we will call such a pixel block as a “uniform pixel block;”

Assumption 2: the probability of a uniform pixel block being from a particular class depends only on the measurements over the block;

Assumption 3: the measurements are conditionally independent, i.e., the spectrum at a specific pixel is determined only by its class membership.

The first assumption is inferred from the spatial continuity of land-cover classes in high-resolution images. It is consistent with the decision-making process in the field: when we say that a pixel belongs to a particular class, it implies that we have seen a

uniform pixel block of this class in the vicinity. This assumption is justified because classes are usually defined at certain spatial scales instead of at the scale of image resolution (Fung and Chan, 1994). In forest mapping, for example, classes are defined as forest stands which may be implicitly associated with minimum areal coverage: a group of trees does not necessarily comprise a stand. Depending on the scale of its definition, one pixel of coniferous trees may not be treated as a conifer stand by the field investigator. However, it may belong to a conifer stand if it is in the neighborhood of several other pixels of coniferous trees.

The second assumption corresponds to the loose correlation in “ground truth” at low spatial scales. Although the spatial continuity may be a necessity at the pixel scale, depending on the spatial scales of image and information map, it is not necessarily so at the scales of mapping units. In other words, uniform pixel blocks surrounding a uniform pixel block of a particular class can be from any class. Using the forest mapping example, a conifer stand may be next to other conifer stands, or hardwood stands, or clear cuts.

The third assumption is introduced largely because it greatly simplifies the derivation of the statistical classification algorithms (e.g., Besag, 1986). When the spatial correlation in measurements cannot be neglected, some modifications are necessary in order to apply the classification algorithms developed based on this assumption (Besag, 1986). Unfortunately, assumption 3 is generally not true for satellite images because the radiance measured at an individual pixel is always “contaminated” by the radiance leaving neighboring pixels (Justice et al., 1989). However, since neglecting the spatial correlation in measurements enhances the spatial continuity in the classification maps, violating the third assumption may only introduce ambiguities along boundaries between different land-cover classes. This is tolerable since some ambiguities arise simply because of intrapixel mixing. Nevertheless, this assumption should be examined and evaluated before using the proposed algorithm.

5.3 MULTI-SCALE TEXTURAL CLASSIFICATION (MSTC) ALGORITHM

5.3.1 Statistical Presentation

Assume that the spatially independent observation, $X = \{x_i, i \in R\}$, where each x_i is a p -dimensional vector, is related to a ground-truth map Y consisting of K units over a two-dimensional surface R . Now the goal is to find, under a certain decision rule, the realization of Y that is most likely to have generated the observation.

The whole image R can be partitioned into uniform regions $\{R_n\}$ which are complete and exclusive, i.e., $\bigcup_n R_n = R$ and $R_m \cap R_n = \emptyset$ for any $m \neq n$. In MSTC, the classification decision is made to maximize the *posterior* probability, that is

$$\begin{aligned} Y &= \arg \max \{ p(Y(R) / X) \} = \arg \max \{ p(Y(\bigcup_n R_n) / X) \} \\ &= \arg \max \{ p(\bigcup_n Y(R_n) / X) \}. \end{aligned} \quad (5.1)$$

where $p(\cdot)$ represents probability. Applying assumption 2 that the scene is uncorrelated at unit-scale, i.e.,

$$\begin{cases} p(\bigcup_n Y(R_n)) = \prod_n p(Y(R_n)) \\ p(Y(R_n) / X) = p(Y(R_n) / X(R_n)) \end{cases}, \quad (5.2)$$

it follows

$$p(\bigcup_n Y(R_n) / X) = \prod_n p(Y(R_n) / X(R_n)). \quad (5.3)$$

and now the task of classification is to solve the optimization problem

$$Y(R_n) = \arg \max \{ p(Y(R_n) / X(R_n)) \}. \quad (5.4)$$

This is the fundamental equation in the MSTC algorithm. It is interesting to compare (5.4) to the more familiar single-pixel-based maximum likelihood classification (MLC) rule (e.g., Deusen, 1995; Foody et al., 1992), i.e.,

$$y_i = \arg \max\{p(y_i / x_i)\}. \quad (5.5)$$

Apparently, MSTC and MLC both are within the Bayesian frame. They are different, however, in that MSTC evaluates consisting of a sample of a larger number of pixels than the MLC, which considers one pixel each time. Since the power of hypothesis test, which determines the accuracy of classification, increases with sample size, it is obvious that MSTC should be more accurate than the MLC. It is understandable, because the textures are contained in the measurements in the neighboring pixels and are involved in decision making.

Because observations at individual pixels are independent (assumption 3), the posterior probability in equation (5.4) is

$$p(Y(R_n) / X(R_n)) = p(y_i / X(R_n))p(Y_{-i} / y_i, X), \quad (5.6)$$

where y_i and Y_{-i} represent the class memberships of the i th pixel and all other pixels within the unit R_n respectively. Because R_n is assumed a uniform region and all pixels in it are from the same class, therefore,

$$p(y_j / y_i) = \delta(y_j - y_i) = \begin{cases} 0, & \text{if } y_j \neq y_i \\ 1, & \text{if } y_j = y_i \end{cases} \quad i, j \in R_n. \quad (5.7)$$

and

$$p(Y_{-i} / y_i, X) = 1. \quad (5.8)$$

Therefore,

$$p(Y(R_n) / X(R_n)) = p(y_i / X(R_n)), \quad (5.9)$$

or in a more symmetric form,

$$p(y_i / X(R_n), i \in R_n) = p(Y(R_n) / X(R_n)) = \left[\prod_{j \in R_n} p(y_j / X(R_n)) \right]^{\frac{1}{N}}, \quad (5.10)$$

where N represents the number of pixels in R_n .

Now apply the Bayesian theorem to the right side of equation (5.10) to get

$$p(y_i / X(R_n)) = \frac{p(y_i)p(x_1, x_2, \dots, x_N / y_i)}{p(x_1, x_2, \dots, x_N)} = \frac{p(y_i) \prod_{j \in R_n} p(x_j / y_i)}{\prod_{j \in R_n} p(x_j)}. \quad (5.11)$$

Assumption 3 has been applied again in order to get equation (5.11). Applying equation (5.7), the conditional probability in (5.11) can be converted to a more appealing form, i.e.,

$$p(x_j / y_i) = \sum p(x_j / y_j)p(y_j / y_i) = p(x_j / y_j). \quad (5.12)$$

By substituting (5.11) and (5.12) into (5.10), the formula to estimate the posterior probability is achieved,

$$p(y_i / X(R_n), i \in R_n) = \left[\prod_{j \in R_n} p(y_j) \right]^{\frac{1}{N}} \prod_{j \in R_n} \frac{p(x_j / y_j)}{p(x_j)}. \quad (5.13)$$

5.3.2 Defining uniform pixel blocks and estimating prior probabilities

Since the exact image partition and prior probability distribution are unknown, they must be estimated simultaneously during the classification procedure. This is accomplished in MSTC via an iterative algorithm.

At first, a uniform pixel block is defined for each class at each pixel, and it approximates the “true” unit partition. According to assumption 1, the existence of such uniform pixel blocks is guaranteed. The textures extracted from the uniform pixel block will indeed be less characteristic than those extracted from the actual unit, but they are still likely to be good approximations to the true textures. At least, such extracted textural information will help to characterize and differentiate different classes in the image better than the spectral information alone.

Because spatial scales of different classes may vary significantly (e.g., Woodcock and Strahler, 1987), there is no reason to assume that the uniform pixel blocks will be of the same size for all classes. This is also not required in the derivation of MSTC. Therefore, as an advantage, the scale information can be

incorporated into texture extraction in MSTC, simply by varying the size and shape of pixel blocks for different classes.

In most contextual and textural classification algorithms, the pixel block, or so-called spatial neighborhood, is centered at the pixel being considered. If a pixel is within a unit, such defined blocks may completely fall inside of the unit and thus are “uniform.” Along unit boundaries, however, such defined pixel blocks will certainly consist of pixels from different classes, and therefore will not be uniform. In the latter case, the textural or contextual information extracted from it will not relate to the true textures of the class to which the pixel belongs. Consequently, the pixel is likely to be misclassified.

To avoid false textures near unit boundaries, the concept of adaptive windows is adopted here to define uniform pixel blocks (Tomia and Tsuji, 1990). Because a pixel can belong to a number of pixel blocks, one needs to define a uniform pixel block of each class for each pixel. Specifically, the uniform pixel block of a specified class here is defined as the one which is mostly uniform and whose texture is most similar to the characteristic textures of that class. Or in terms of probability, the uniform pixel block of class k for pixel i is defined as

$$\begin{aligned} S_i^k &= \arg \max \{ p(Y(S_i^k) / X(S_i^k)) \} \\ &= \arg \max \left\{ \left[\prod_{j \in S_i^k} p(y_j = k) \right]^{1/N_k} \frac{\prod_{j \in S_i^k} p(x_j / y_j = k)}{\prod_{j \in S_i^k} p(x_j)} \right\}. \end{aligned} \quad (5.14)$$

where N_k is the number of pixels in the uniform pixel block S_i^k . Apparently, there are a total of K uniform pixel blocks, one for each class, for every pixel in the image. The posterior probability for the i th pixel being from class k is therefore,

$$p(y_i / X(S_i^k)) = \left[\prod_{j \in S_i^k} p(y_j) \right]^{1/N} \prod_{j \in S_i^k} \frac{p(x_j / y_j)}{p(x_j)}. \quad (5.15)$$

Without any prior knowledge other than the satellite measurements, the classification is initiated by assuming homogenous *a priori* for all classes across the image, i.e.,

$$p(y_i = k) = 1 / K . \quad (5.16)$$

The prior probabilities are then re-estimated, pixel by pixel, with the after-classification knowledge on the scene, simply by normalizing the posterior probabilities in (5.15), i.e.,

$$p(y_i = k) = \frac{p(y_i / X(S_i^k))}{\sum_{k=1}^K p(y_i / X(S_i^k))} . \quad (5.17)$$

The iterative estimation of the prior probability, as in (5.17), is equivalent to repeating the measurements at infinitesimal time intervals. As we have discussed in 5.2, the spectral variability within each class as expressed in $p(X/Y)$ is largely related to the spectral variation from one location to another. For a specific pixel, however, its spectrum is more like a deterministic event and the repeatedly observed spectra will show much smaller variation than the within-class variability. Consequently, any one observation provides nearly the same amount of information as infinite observations, given that they are accomplished in a very short period of time so that no change may occur. Therefore, the iterative estimation of prior probability is reasonable for processing satellite images, and it will converge to one of the two possibilities, zero (false) and one (true).

5.3.3 Implementation of MSTC

To summarize, MSTC classifies individual pixels based on their spectra and their spectral contexts as well. Specifically, when a pixel is considered for classification, a number of pixel blocks are first identified, each of which represents a possibly uniform unit (Fig. 5.1) of a certain class in the scene. Then the probabilities are evaluated for these pixel blocks to determine which of them is the most likely true

uniform pixel block of the corresponding class membership. It is then assigned as the class membership for the considered pixel.

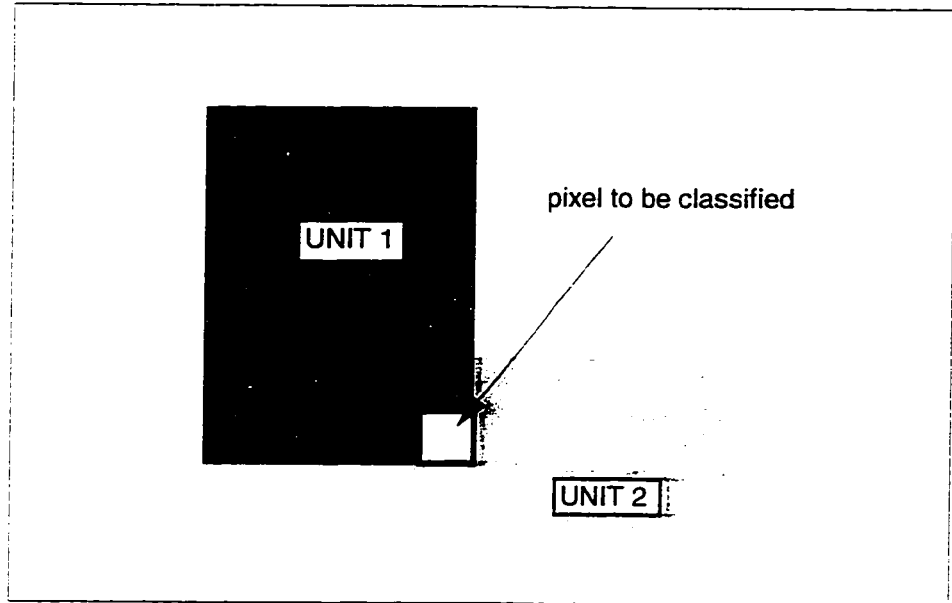


Figure 5.1 Sketch to show how spectral context information is defined in MSTC. The pixel (shaded) to be considered is put into pixel blocks that represent possible unit partitions at its location. The pixel blocks are then evaluated based on their spectra to find which of them is most likely a true unit.

Practically, the MSTC algorithm can be implemented as an iterative classification algorithm:

Step one: calculate $p(x_i / y_i = k)$ for $\forall i \in R$ and $\forall k \in \Omega$;

Step two: assume uniform *priori*, i.e. $p(y_i = k) = 1/K$ for $\forall i \in R$ and $\forall k \in \Omega$;

Step three: estimate $p(Y(S_i^k) / X(S_i^k))$ and to find S_i^k according to (5.14) for $\forall i \in R$ and $\forall k \in \Omega$;

Step four: calculate $p(y_i / x(S_i^k))$ based on (5.15) for $\forall i \in R$ and $\forall k \in \Omega$;

Step five: estimate $p(y_i = k)$ with equation (5.17) for $\forall i \in R$ and $\forall k \in \Omega$;

Repeat step three through five until convergence;

Step six: assign each pixel a class which maximizes $p(y_i / x(S_i^k))$.

5.3.4 Interpretation of MSTC

The term $\prod_{j \in S_i^k} p(x_j / y_j)$ in the posterior probability in equation (5.15) contains the texture features involved in the MSTC algorithm. It is interesting to see what the textural features are and how they affect the classification decision. For a representative case, each class k is assumed to follow a normal distribution characterized by its mean vector u_k and covariance matrix V_k , i.e.,

$$p(x_j / y_j = k) = \frac{1}{(\sqrt{2\pi})^p |V_k|^{1/2}} \exp\left[-\frac{1}{2}(x_j - u_k)' V_k^{-1} (x_j - u_k)\right]. \quad (5.18)$$

Therefore, the textural information used in (5.13) can be expressed as

$$\prod_{j \in S_i^k} p(x_j / y_j = k) = \frac{1}{(\sqrt{2\pi})^{N_i \times p}} \exp\{-0.5[\sum_{j \in S_i^k} (x_j - u_k)' V_k^{-1} (x_j - u_k) + N_k |V_k|]\}, \quad (5.19)$$

The exponential term, after dropping the constants, is

$$\Gamma = \frac{1}{N_k} \sum_j (x_j - u_k)' V_k^{-1} (x_j - u_k) + \log|V_k|. \quad (5.20)$$

However,

$$\begin{aligned} \sum_j (x_j - u_k)' V_k^{-1} (x_j - u_k) &= \sum_j [(x_j - \bar{x}) + (\bar{x} - u_k)]' V_k^{-1} [(x_j - \bar{x}) + (\bar{x} - u_k)] \\ &= \sum_j (x_j - \bar{x})' V_k^{-1} (x_j - \bar{x}) + 2 \sum_j (x_j - \bar{x})' V_k^{-1} (\bar{x} - u_k) + \sum_j (\bar{x} - u_k)' V_k^{-1} (\bar{x} - u_k) \\ &= N_k [Tr(\tilde{V} V_k^{-1}) + (\bar{x} - u_k)' V_k^{-1} (\bar{x} - u_k)] \end{aligned}$$

where $\bar{x} = \frac{1}{N_k} \sum_j x_j$, $\tilde{V} = \frac{1}{N_k} \sum_j (x_j - \bar{x})(x_j - \bar{x})'$ are the estimated mean vector and covariance matrix of the pixels in S_i^k respectively, and $Tr(V)$ denotes the trace of matrix V . Therefore,

$$\Gamma = (\bar{x} - u_k)' V_k^{-1} (\bar{x} - u_k) + Tr(\tilde{V} V_k^{-1}) + \log|V_k|. \quad (5.21)$$

The first term in (5.21), $\Gamma_1 = (\bar{x} - u_k)' V_k^{-1} (\bar{x} - u_k)$, measures the distance of the texture feature “mean” vector in S_i^k from the mean vector of class k , normalized by the covariance. It is straightforward to demonstrate that it reaches the minimum at

$$\bar{x} = u_k. \quad (5.22)$$

The second and third terms together $\Gamma_2 = Tr(\tilde{V} V_k^{-1}) + \log|V_k|$ describes the impact from another important texture feature “covariance” matrix. To find its minimum, the positive definite covariance matrix is written as

$$V_k = LDL', \quad (5.23)$$

where $D = \text{diag}\{\lambda_1, \lambda_2, \dots, \lambda_p\}$ is a diagonal square matrix with diagonal elements $\{\lambda_1, \lambda_2, \dots, \lambda_p\}$ being the eigenvalues of V_k and L is an orthogonal square matrix.

Thus

$$\begin{aligned} Tr(\tilde{V} V_k^{-1}) &= \sum_j (x_j - u_k)' V_k^{-1} (x_j - u_k) = \sum_j (x_j - u_k)' L' D^{-1} L (x_j - u_k) \\ &= \sum_j z_j' D^{-1} z_j = \sum_j z_j^2 / \lambda_j \end{aligned} \quad (5.24)$$

where $z_j = L(x_j - u_k)$, and

$$\log|V_k| = \log\left(\prod_j \lambda_j\right) = \sum_j \log \lambda_j. \quad (5.25)$$

Therefore

$$\Gamma_2 = \sum_j (z_j^2 / \lambda_j + \log \lambda_j). \quad (5.26)$$

Now set the partial derivatives

$$\frac{\partial \Gamma_2}{\partial \lambda_j} = -\frac{z_j^2}{\lambda_j^2} + \frac{1}{\lambda_j} = \frac{(z_j^2 - \lambda_j)}{\lambda_j^2} = 0, \quad (5.27)$$

to get

$$\lambda_j = z_j^2, \quad \text{for } j=1,2,\dots,p, \quad (5.28)$$

which leads to

$$\begin{aligned} Tr(\tilde{V}) &= \sum_j (x_j - \bar{x})'(x_j - \bar{x}) = \sum_j (x_j - \bar{x})' L' L (x_j - \bar{x}) = \sum_j z_j^2 = \sum_j \lambda_j \\ &= Tr(V_k) \end{aligned} \quad (5.29)$$

The minimum of Γ_2 is reached when the estimated covariance of the pixels in S_i^k equals the covariance matrix of the class k . Because the trace of a matrix has been widely used to measure the differences between matrices, it simply means that the more similar the estimated covariance matrix to class k , the more likely these pixels are from class k .

5.3.5 Comparison with pure contextual/textural approaches

The MSTC algorithm is a hybrid textural classification algorithm. This is shown in equation (5.15) via which the posterior probabilities are estimated and the classification decisions are made. The prior probabilities in (5.15) reflect the constraint on spatial continuity in the ground truth, similar to the contextual approach. The conditional probabilities, as discussed in last section, contain information about the textures in the image which are used in the textural approaches. This unique feature results certain advantages for MSTC over both the contextual and textural approaches.

The contextual approach assigns a pixel class membership based on its spectrum, with constraint imposed by the memberships at nearby pixels. It thus heavily relies on the statistical model (including its parameters) used to describe the ground truth. Lack of justification of such models leads to difficulties in evaluating the reliability of its product. In addition, initialization of ground truth can be erratic when

it is based on MLC in case classes are spectrally similar. In contrast, MSTC assumes no statistical models, nor parameters. The ground truth in MSTC is recursively estimated based on the textural information and plays a less important role than in the contextual approaches. Thus it is expected that MSTC should not be so sensitive to the initialization as the statistical approach.

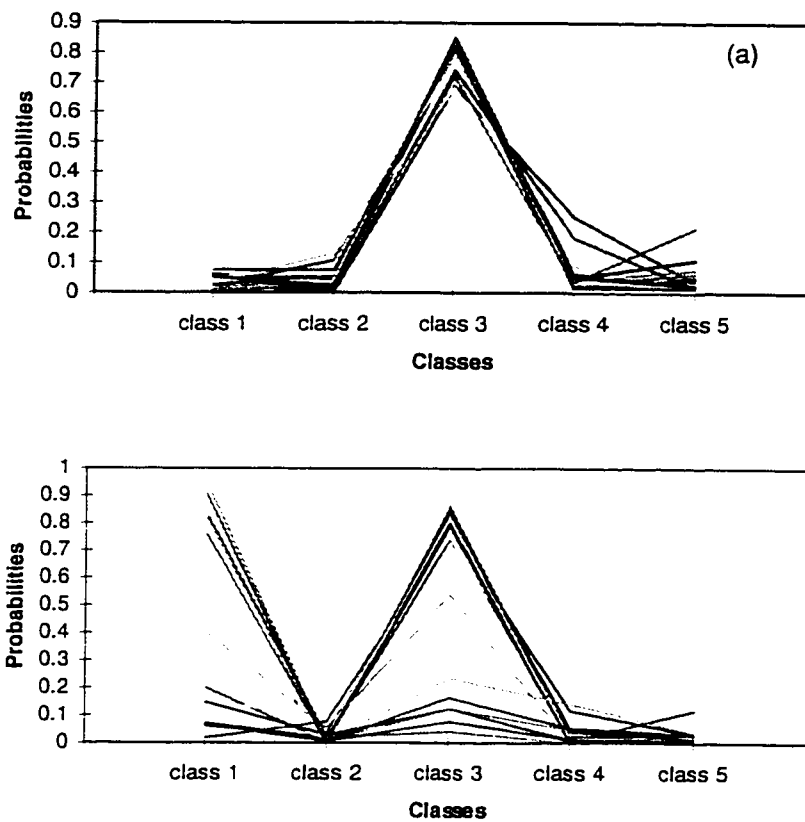


Figure 5.2 Probability distribution in a uniform pixel block (a) and a mixed pixel block (b). Notice in (b) that the probability distributions of individual pixels have different peaks corresponding to their true memberships.

Contrasting to the pure textural classifiers which blindly estimate textural features in spectral images, MSTC searches for uniform pixel blocks to extract textural

features. Because the pure textural approach can not evaluate whether a pixel block is uniform or not, it usually extracts false textures along unit boundaries. This may lead to misclassification of unit boundaries to a third class (Tomia and Tsuji, 1990). Although not reliably detectable from estimated textures, however, pixel blocks lying over unit boundaries consist of pixels with significantly varying probabilities. If a pixel block is uniform, the probability distributions of its pixels will also be similar, peaked at the class corresponding to the ground truth (Fig. 5.2a). When a pixel block is not uniform, consisting of pixels from different classes, the probability distributions will peak at different classes accordingly (Fig. 5.2b). As a result, the product of the probabilities for these pixels will be smaller than in uniform blocks. Therefore, MSTC can detect and avoid non-uniform pixel blocks. By identifying the mostly uniform pixel blocks, MSTC is expected to extract true textures and perform well even near unit boundaries.

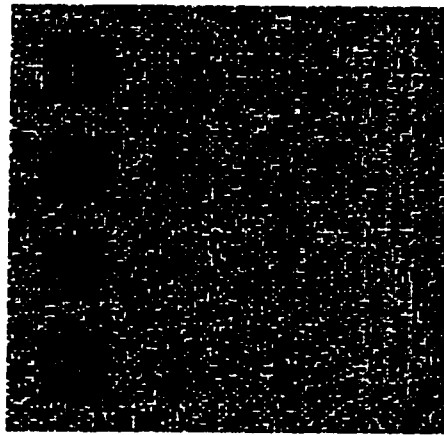
5.4 TEST ON SYNTHETIC IMAGES

5.4.1 Image description

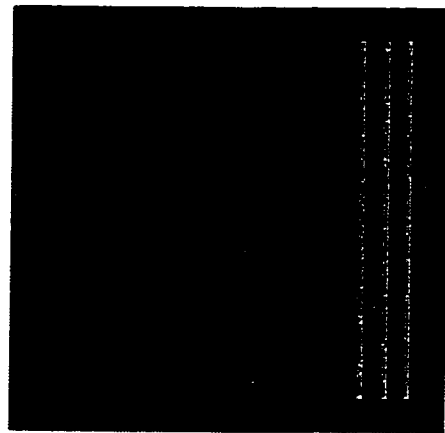
MSTC is first tested in a two-channel synthetic image (Fig. 5.3a) of the known truth (Fig. 5.3b). The image consists of five classes, which all follow normal distributions with the same variance but with different means. As shown in Table 5.1, the spectra are quite similar among these classes. As a result, they are not very separable based upon their spectra alone. The spatial scales of these classes are also significantly different from each other for the purpose of testing the scale effects. For example, classes 1 (squares) and 2 (discs) are large in comparison to classes 4 (rectangles) and 5 (lines).

Table 5.1. Features of Classes in the synthetic image

Class	Spectral Mean		Spectral Variance		Structure	Block Size
	Channel 1	Channel 2	Channel 1	Channel 2		
1	42.5	50	25	25	squares	5x5
2	50	42.5	25	25	discs	5x5
3	50	50	25	25	background	5x5
4	50	57.5	25	25	rectangles	3x9
5	57.5	50	25	25	lines	1x21



(a)



(b)

Figure 5.3 The synthetic testing image (a) and the truth map that generates it (b).

For comparison, MLC, a spectral classifier, and ICM (Besag, 1986), a contextual classifier, are also used to classify the test image. According to ICM, every pixel is classified based on its spectrum and the class memberships at its nearby pixels. Based on the Bayesian theorem, if the spatial correlation of the truth map can be described by MRF model, the posterior probability (for the i th pixel being from class k) is

$$p(k / x_i, Y(s_i)) = \frac{p(x_i / k)p(k / Y(s_i))}{p(x_i)} \propto p(x_i / k)e^{\beta\mu_k} \quad (5.30)$$

where μ_k is the total number of pixels from class k in the spatial neighborhood s_i , and β is model parameter. ICM labels individual pixels to maximize the posterior probability in (5.30). Parameter β characterizes the intensity of spatial correlation, and plays an important role in ICM's performance. If $\beta = 0$, i.e., there is no spatial correlation at all, ICM is identical to MLC. As β increases, which implies increasing spatial correlation, the classified map will be spatially more uniform. It has been suggested that gradually increasing β during the iteration may lead to slightly better performance than choosing a fixed β (Besag, 1986). This appears to be true to the simulated image, and β is gradually increased from 0.5 to 1.5 during the iteration, which is found to give the best performance in the test image.

Only supervised classifications were conducted, with the spectral means and variances from Table 5.1 as input for all three classifiers.

5.4.2 Evaluation of classification results

Figure 5.4 shows the classification results produced by the three classifiers. The MLC gives a very noisy classification map (Fig. 5.4a), which shows virtually no spatial continuity. Due to large overlaps in brightness among some of the classes, many pixels are misclassified, yielding an average classification accuracy of only 60.3% (Table 5.2, Fig. 5.5). Visually, the classified image exhibits no similarity at all to the "truth" map. Instead, it mimics the data image (Fig. 5.3a). Therefore, the classified image provides little additional information than the unclassified image itself.

The ICM algorithm results a cleaner and more accurate map (Fig. 5.4b) than the MLC. The average classification accuracy is improved to 88.5% (Table 5.2, Fig. 5.5). In particular, larger units (classes 1 and 2) are quite well defined and labeled.

However, the smaller units (classes 3, 4 and 5) are not as well classified, yielding relatively low accuracy. Especially, great confusion occurs nearby the line features (class 5), where ICM performs poorest and the misclassification rate is very high. From Figure 5.6a, which shows the distribution of misclassified pixels (bright) in the ICM-classified map (Fig. 5.4b), it is estimated almost 50% of the pixels are misclassified in the vicinity of the line features. This illustrates an important point: spatial scale is an important factor to be considered in designing textural classifiers. Failure to reflect the variation in spatial scales may possibly limit classifier's performance.

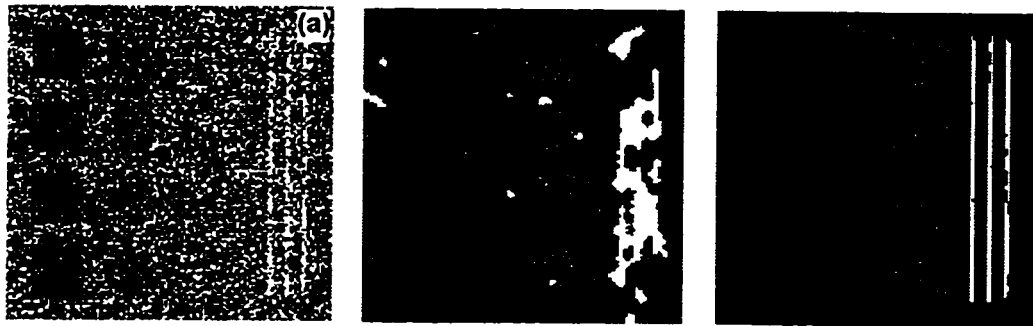


Figure 5.4 Classification maps produced by the MLC (a), the ICM (b), and the MSTC (c) algorithms, respectively.

Table 5.2. Classification accuracy of different classifiers in the synthetic image

Class	MLC	ICM	MSTC
1 (squares)	71.1%	98.4%	97.4%
2 (discs)	67.6%	98.1%	97.1%
3 (background)	27.6%	86.6%	99.6%
4 (rectangles)	69.6%	94.3%	94%
5 (lines)	65.8%	65%	92.7%
Average	60.3%	88.5%	96.2%

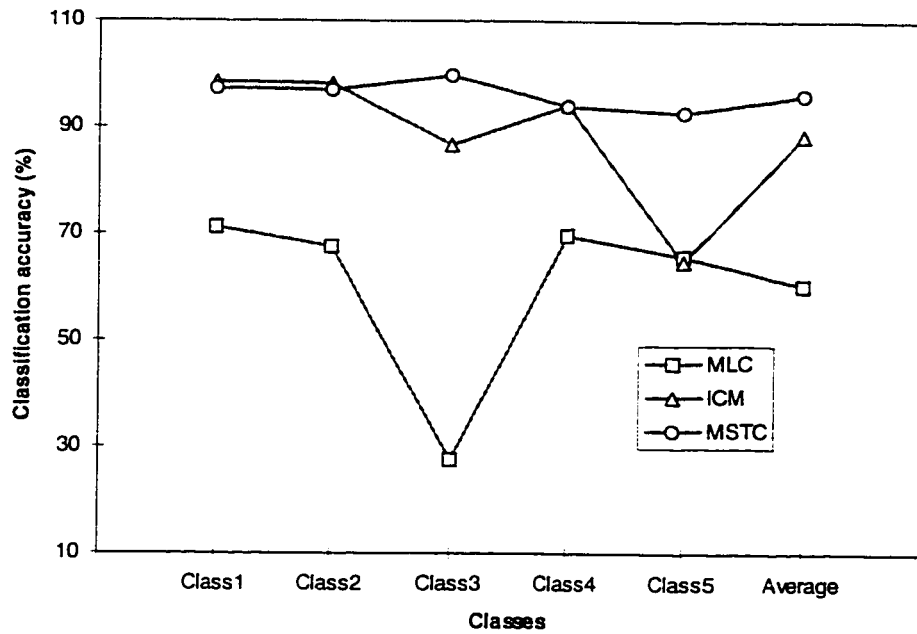


Figure 5.5 Classification accuracy of the MLC (squares), the ICM (triangles) and the MSTC (circles).

The MSTC algorithm produced the most accurate classification map (Fig. 5.4c), almost identical to the truth map. The average classification accuracy improved to about 96.2% (Table 5.2), about 7.7% and 35.9% improvements over the ICM and MLC, respectively. Comparing to ICM, the MSTC algorithm is particularly advantageous in identifying the smaller units. Although they are still not detected as accurately as the larger units, the smaller units are much better classified by MSTC. For example, the classification of the line features has been significantly improved from 65% with ICM to 92.7% with MSTC, an impressive improvement of nearly 38%. From accuracy point of view, MSTC clearly outperforms ICM and MLC for the testing image.

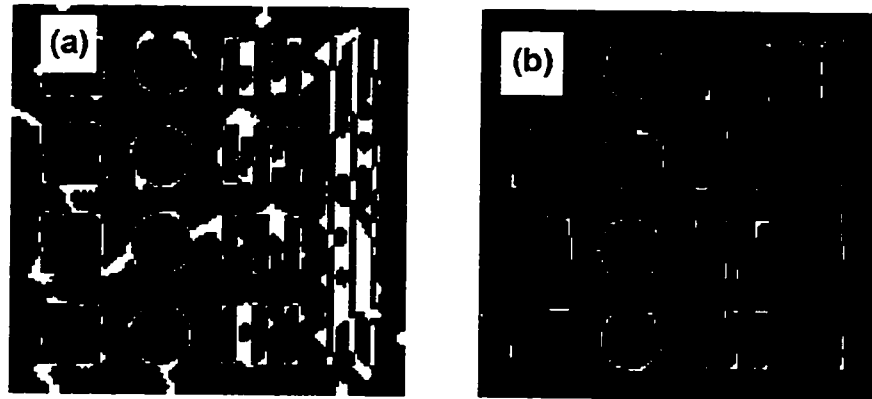


Figure 5.6 Distribution of misclassified pixels on classification maps produced by ICM (a) and MSTC (b). The misclassified pixels are highlighted (bright) against the correctly classified pixels (dark).

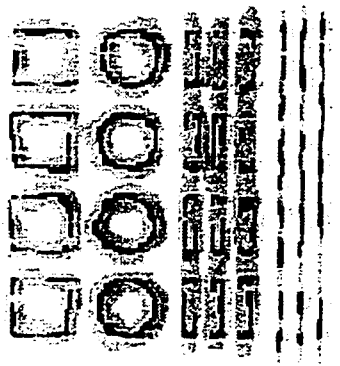


Figure 5.7 Probability distribution of the MSTC classification map. Low probability values (darker) characterize unit boundaries and indicate the uncertainties in the classification map.

The pixels misclassified by MSTC are largely distributed around unit boundaries (Fig. 5.6b), in contrast to their concentration near smaller units in the ICM-classified map (Fig. 5.6a). This is tolerable, because ambiguity is inevitable near unit boundaries, particularly so in natural scenes (Fisher, 1997). In addition, the misclassified pixels in MSTC classification map are characterized with lower posterior

probabilities, and thus the classification results at these pixels are of less certainty, than the correctly classified pixels (Fig. 5.7). Therefore, the MSTC also provides information on the reliability of its classification maps.

5.4.3 Sensitivity on initialization

Since both ICM and MSTC are iterative classifiers, it is important to examine if they are sensitive to the initialization. A good algorithm should not be sensitive to the variations in initialization, and should converge to similar results for different initializations. For this purpose, several classifications have been conducted with different initializations by varying the prior probabilities, which include:

1. assigning uniform prior probabilities, i.e., $p(1 \leq k \leq 5) = 0.2$;
2. assigning random prior probabilities, i.e., $p(1 \leq k \leq 5) = \text{random}(0,1)$;
3. assigning single-color prior probabilities, i.e., assuming all pixels in the image being from class 3: $p(3) = 0.9$, $p(k \neq 3) = 0.025$.

Figure 5.8 shows the classification results produced by ICM, which differ from each other significantly. Because all other inputs for the classifier are identical, the difference in initialization is the only cause for the striking differences in the classification maps. Although there are only three tests, it is sufficient to say that ICM is heavily dependent of initialization. Therefore, it is critical to start with a good guess on the truth map in order to implement ICM successfully. This can be a major disadvantage in practical applications.

In contrast, MSTC has converged to exactly the same classification maps for these three initializations. Several other tests are performed and the results have confirmed that MSTC converges to the same map as Figure 5.4c, independent of initialization. Therefore, MSTC appears to be independent of initialization, at least for the tested cases and the test image. Unfortunately, it remains unknown if there is always a unique stable solution to which MSTC will converge in other images with

different properties. As a non-linear system, MSTC has too many degrees of freedom to examine its full solution space by analytical approaches. Exhaustive search of numerical solutions seems unrealistic, too.

It is clear, however, that MSTC should be less sensitive to initialization than ICM because it depends more on the conditional probabilities (data) than on the prior probabilities (initialization).

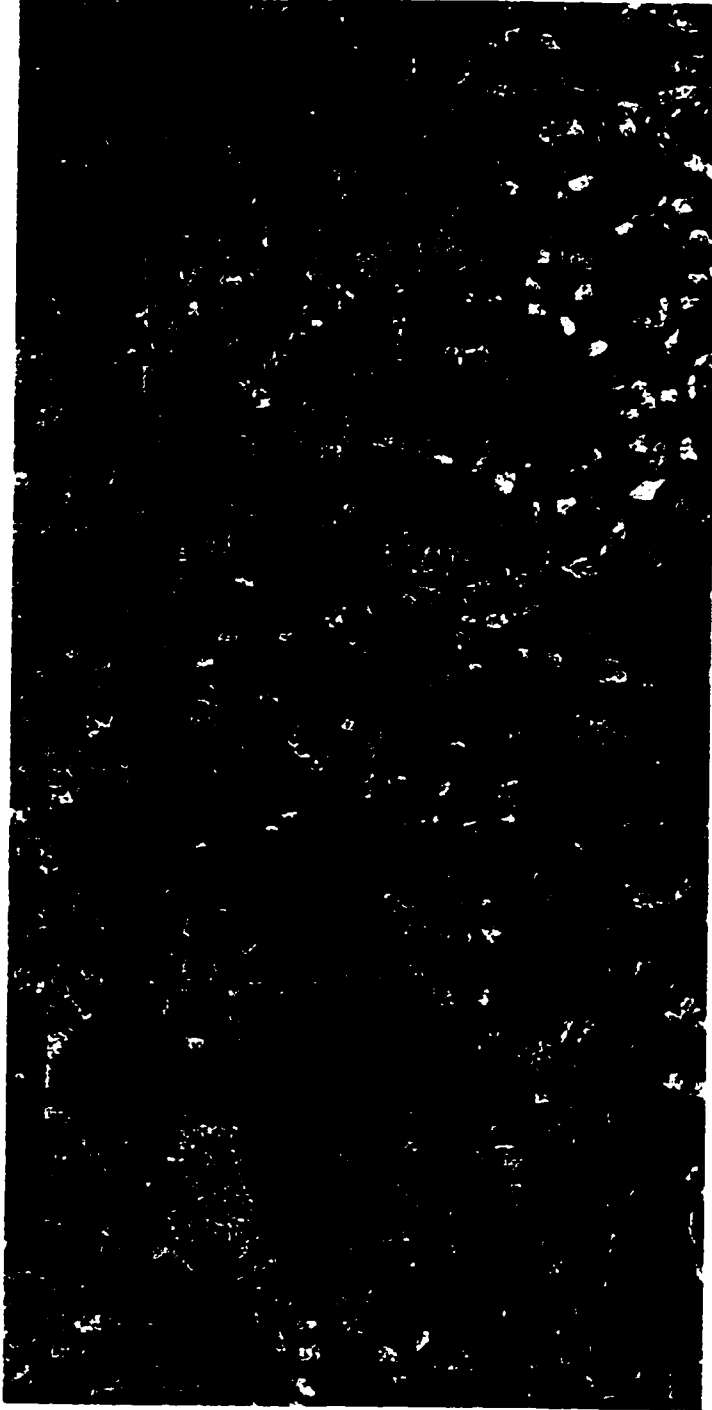


Figure 5.8 Classification maps produced by the ICM with different initializations. (a) uniform prior probability, (b) random prior probability and (c) single-color prior probability. The great differences between these maps indicate ICM's dependence on the initialization.

5.5 TESTS ON TM IMAGES OF FORESTS

The MSTC is also applied to a subset of TM image (Fig. 5.9) over the Bluff Creek watershed, Six Rivers National Forest, California. The scene is differentiated into five major classes, water (WATER), open-canopy forest on serpentine substrate (OPEN), old-growth and mature regrowth (OLD), 10-50 year old pole-stage regrowth (POLE), and new replantation (replanted within 10 years) and clear cuts (CC).

The classifiers were first trained ground-truth information, which was compiled based on the data provided by the U.S. Forest Service and by field inspection. About 30% of the data were chosen randomly to estimate the spectral



**Figure 5.9 Pseudo-color TM image of the Bluff Creek, Six Rivers National Forest, California.
Bands 3, 4 and 5 are displayed as blue, green and red, respectively.**

means and variances for each of the five land-cover types, which show some degree of spectral similarities and overlaps (Fig. 5.10). The rest of the data were then classified with MLC and MSTC, respectively.

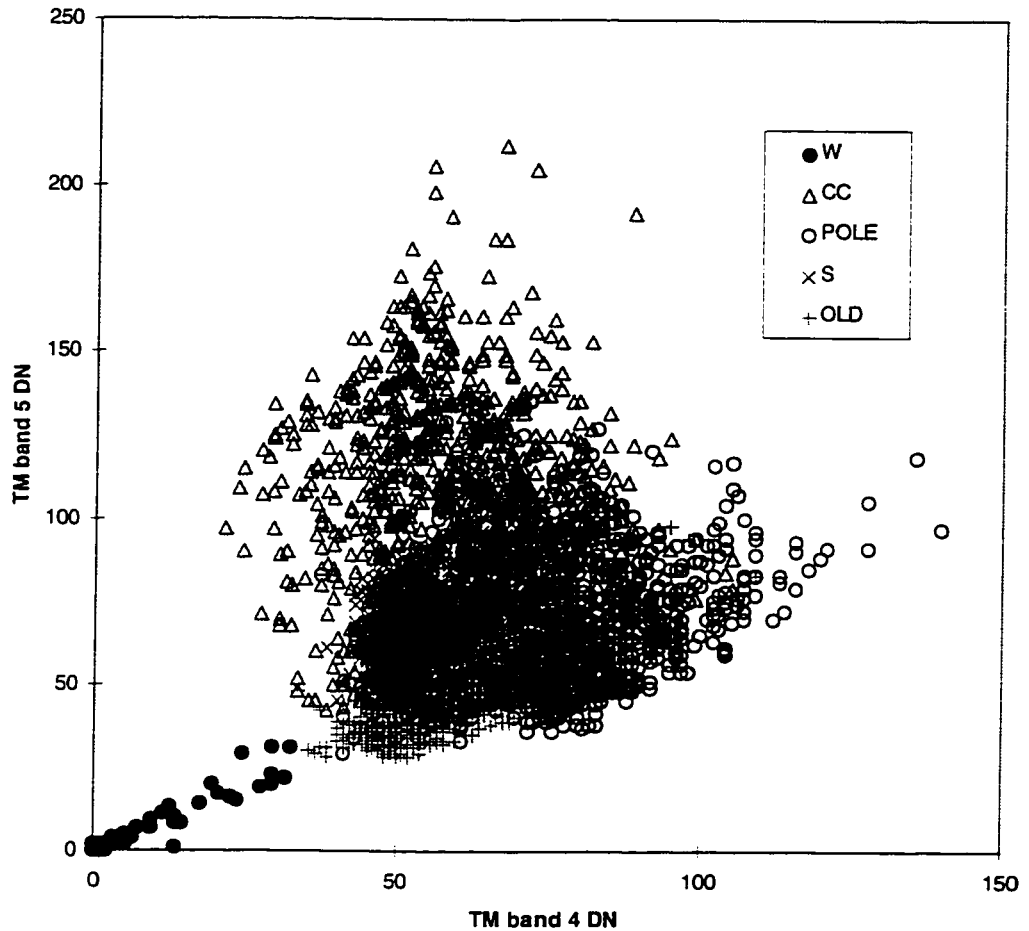


Figure 5.10 TM band 4 and 5 spectral contrasts between different land cover types defined in the testing image. Water has very distinct spectra, but there are overlaps between the other four classes.

Figure 5.11 shows the classification results produced by the MLC, which yields an overall accuracy of 70% (Table 5.3). Between classes of large spectral contrast, such as water vs others, the misclassification rate is low. Spectrally similar classes, however, such as POLE and CC (Fig. 5.10), are characterized by low classification accuracy (Table 5.3). In general, the classified image appears a little noisy and shows limited spatial continuity.

Table 5.3. Classification accuracy in the TM image by MLC and MSTC

Class	WATER	OPEN	OLD	POLE	CC	overall
MLC	95.5%	89.7%	90.5%	64.4%	63.3%	70.0%
MSTC	98.5%	96.8	94.1%	71.6%	76.8%	78.8%

The MSTC produces a more accurate map (Fig. 5.12) than the MLC, with an overall classification accuracy of 78.8%, nearly 9% improvement over the MLC. In particular, a large improvement is achieved in separating spectrally similar classes. For example, the accuracy of identifying CC, which has large spectral overlaps with all other classes except water, has improved from 63.3% to 76.8%, a 13.5% improvement. Moreover, the classified image appears less “noisy” than the MLC-classified image, and defines unit boundaries well.

Although the MSTC has improved the classification accuracy over MLC by about 9%, it has not come close to the improvement achieved in the synthetic image. Similar results also happen to other classifiers which show great advantages in synthetic images but result in less improvements in classifying satellite images (e.g., Bouman and Shapiro, 1994). As one of the many possible reasons for this general phenomenon, errors in describing the statistical distributions of individual classes may account for much of the loss of the performance. Even if samples of large populations may be well characterized, significant deviations from the assumed distributions may occur locally in satellite images (Skidmore, 1989). As a result, the classifiers can not accomplish the achievements of which they are theoretically capable. How to deal with

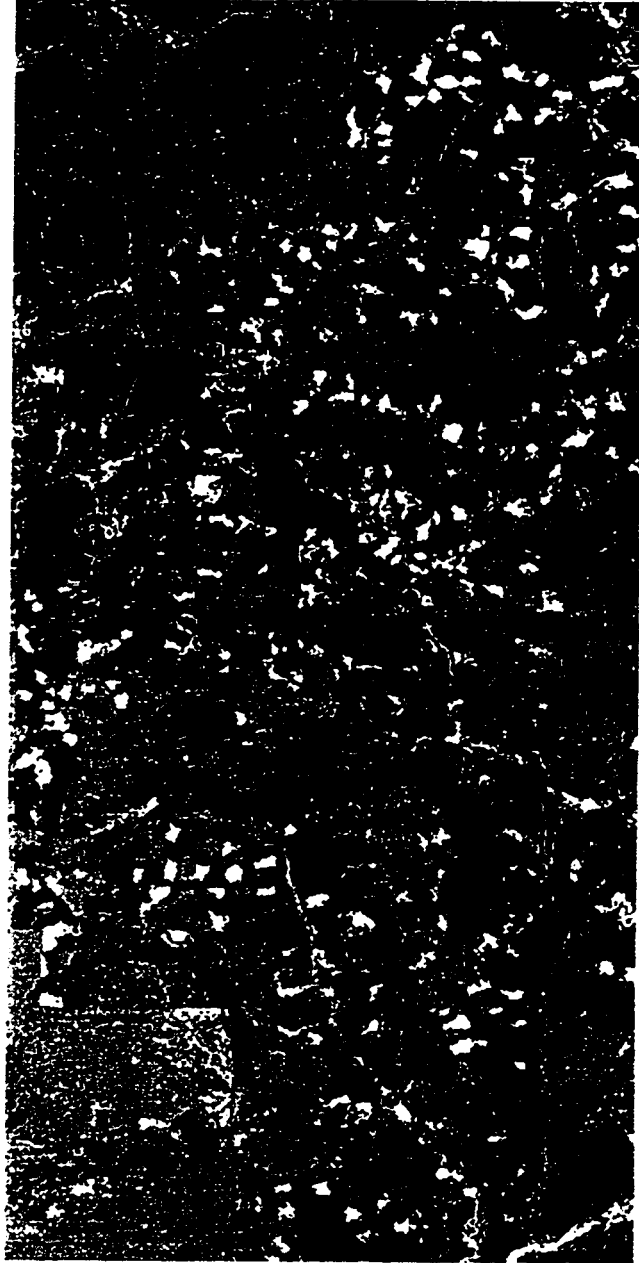


Figure 5.11 Classification map of the testing TM image produced by MLC.



Figure 5.12 Classification map of the testing TM image produced by MSTC.

the localized spectral variation within individual classes remains an important topic for study, for the practical applications of the MSTC as well as other sophisticated classifiers.

5.6 SUMMARY

Spatial structures in natural scenes contain textural information that can improve the classification accuracy of satellite images. The new Multi-Scale Textural Classification (MSTC) algorithm has been developed that uses both the image texture and spectral data to classify satellite images within a Bayesian framework. It assumes that the scene is highly correlated at the pixel-scale but uncorrelated at the unit-scale.

One key feature in the MSTC is that the textural features are estimated at different scales for different units so that small-scale units can now be preserved instead of being “smoothed” out. In addition, since for any pixel in any unit, there exists at least one pixel block which completely falls into the unit, the textural features estimated from such a uniform pixel block define the “true” textures at the location of that pixel. Whether a pixel block is uniform in composition is judged based on the likelihood functions of all the pixels within it. In this way, the false textures near unit boundaries are identified and disregarded. When only the “true” textures are considered in classifying the image, the ambiguity near unit boundaries is resolved.

The MSTC algorithm does not explicitly calculate the textures when classifying individual pixels. Instead, it directly uses the spectral data at the nearby pixels from which the “true” textural features are extractable. When units are normally distributed, for example, the implicitly considered textural features in the MSTC algorithm are mean and variance. Obviously, the textural features will be different in case the distributions are different.

The MSTC algorithm yields accuracy of 95% or higher on a computer-simulated forest image which is otherwise classified at accuracy of 65% with a Maximum Likelihood Classifier (MLC), and 88% with a contextual classifier (ICM).

The MSTC was found to be insensitive to the initial conditions under which the iterative algorithm is implemented. In contrast, the ICM shows great dependence on initialization, and yields significantly different results when initial condition changes. In addition, the MSTC also provides information on the reliability of classification results at individual pixels. The misclassified pixels, which are mostly distributed near unit boundaries, have generally lower posterior probabilities than the correctly classified pixels.

When applied to a set of Landsat Thematic Mapper images over the Bluff Creek Watershed, Six Rivers National Forest, California, the accuracy of the MSTC algorithm reaches 78.8%, nearly 9% higher than the accuracy achieved with the MLC.

CHAPTER 6: SUMMARY

This research has been focused on incorporating structural information into interpretation of satellite images. With such a goal, the structural effects on surface reflection were first studied with computer-simulated forest canopies. It was found that structure is indeed a key factor that controls the spectrum, albedo and radiance distribution of the simulated canopies. Such results justified the effort toward developing new tools for making use of surface structural information in image interpretation.

There are four types of spatial scales involved in satellite image interpretation, related to 1) surface structure, 2) interaction of light with surface, 3) interesting ground features, and 4) image resolution. The characteristics of satellite images largely depend on these four scales. The last two scales are particularly important regarding image interpretation. If the interesting features are not resolved, satellite measurements correspond to the “mixtures” of various features, and image interpretation is a subpixel-scale inversion problem. If the interesting features are resolved, their structures provide important information for their identification and the image interpretation is generally a pattern recognition problem, although it still requires background knowledge on their fine-scale structures in order to relate spectral classes to ground features. This understanding should be the general principle of image interpretation and the basis for developing subsequent image processing techniques to use structural information.

The layered spectral mixture analysis (LSMA) model is a good example to illustrate the significance of considering structural characteristics in subpixel-scale spectral mixture analysis. Because of structure, spectral mixing at pixel-scale is not unambiguously correlated to the compositional mixing in the ground. Thus simple

spectral mixture models which do not consider surface structure have difficulties to link endmember fractions to the areal abundance of interested features. In the LSMA model, image endmembers are defined at specific spatial scales and have characteristic structures, and endmember spectra are chosen to reflect the illumination variations within structured endmembers. As a result, the LSMA model is more suitable for analyzing images of highly structured scenes. As tests suggested, the new model predicts canopy closure with better accuracy than the simple spectral mixture model, and the accuracy improvement ranges from about 9% on smooth canopies to 27% for rough canopies.

A topographic correction model (SCS) was proposed to remove topographic effects on Landsat TM images of forests. Because trees are generally geotropic, topography does not change the illumination geometry at individual tree elements, although the amount and pattern of shadows within tree canopy do change on various slopes. On sun-facing slopes, a larger area of tree canopy is illuminated and thus appears to be brighter than on the slopes facing away from the sun. Therefore, it is the total area of sunlit tree crowns, rather than the irradiance, in individual pixels that should be normalized to remove the topographic effects. The SCS model was proved to be better than the cosine correction model, and to perform at least equally as well as some more complicated models, such as the Minnaert correction model and the c-correction model, on two TM test images.

The commonly observed high variance in topographically corrected images are usually attributed to imperfection of models that describe surface reflectance distributions. But careful examination suggests that various errors related to instrument noise, DEM accuracy, registration mismatch, and model simplifications may be the dominant source of variance. The contextual topographic correction approach was proposed to reduce the error effects. This approach compensates for variations in satellite-measured radiance due to topographic variations according to the "local" reflectance in a spatial neighborhood. Since the local reflectance can be more

reliably estimated than the reflectance at individual pixels, this new approach effectively reduced the errors in the corrected images. Comparing to the conventional, single-pixel-based topographic correction approach, the image corrected with the new approach appears less noisy and has a higher signal-noise ratio. Consequently, different land-cover classes are more separable in the contextually corrected image than in the conventionally corrected images.

The multi-scale textural classification (MSTC) algorithm was another model developed to use spatial information in processing satellite images. The MSTC model directly uses the textural information contained in the satellite measurements to enhance the characterization and identification of different land-cover classes. One unique feature of the MSTC algorithm is the simultaneous estimation of the class membership and the texture via an iterative approach. As a result, the MSTC is not sensitive to various initializations. This model is also able to treat complicated scenes which consist of features of various characteristic scales. The test on a synthetic image suggests that the MSTC is a much better classifier than the commonly used spectral classifiers, such as MLC, with classification accuracy improved from 60.3% to 96.2%. When applied to a TM image of forest, the MSTC algorithm yielded the overall accuracy of 78.8%, about 9% higher than the accuracy of 70% achieved with the MLC.

As demonstrated by the above four models, there is a great potential to improve the reliability of information extracted from satellite images simply by considering structural information. A great effort should thus be made in this direction because the accuracy of satellite image interpretation has hindered the application of remote-sensing data in many areas. Whereas developing new models and algorithms is necessary in order to incorporate the structural information, it is equally important to accumulate more field data to characterize the structural effects on various aspects of surface reflection. In-situ measurements at scales close to satellite image resolutions are particularly lacking, and data suitable to study the scale-dependence of satellite images are virtually non-existent. This lack hinders the understanding and the use of

structural information. Therefore, the remote-sensing community should work together to find an efficient way to collect such data. I believe that the currently available satellite data have not been exploited well and such an effort will be more effective than designing new instruments for some, if not many, remote-sensing applications.

BIBLIOGRAPHY

- Abuelgasim, A. A., and A. H. Strahler (1994), Modeling of bidirectional radiance measurements collected by the Advanced Solid-State Array Spectroradiometer (ASAS) over Oregon transect conifer forests, *Remote Sens. Environ.* 47, 261-275.
- Adams, J. B., and T. B. McCord (1986), Spectral mixture modeling: A new analysis of rock and soil types at the Viking Lander 1 site, *J. Geophys. Res.* 91, 8098-8122.
- Adams, J. B., D. E. Sabol, V. Kapos, R. Almeida Filho, D. A. Roberts, M. O. Smith, and A. R. Gillespie (1995), Classification of multispectral images based on fractions of endmembers: Application to land-cover change in the Brazilian Amazon, *Remote Sens. Environ.* 52, 137-154.
- Adams, J. B., M. O. Smith and A. R. Gillespie (1993), Image Spectroscopy: Interpretation based on spectral mixing analysis, in *Remote Geochemical Analysis: Elemental and Mineralogical Composition*, by C. M. Pieters and P. Englert (editors), LPI and Cambridge University Press, 145-166.
- Adams, J. B., M. O. Smith and A. R. Gillespie (1989), Simple model for complex natural surfaces: A strategy for the hyperspectral era of remote sensing, *Proc. IGARSS'89/ 12th Canadian Symposium on Remote Sensing I*, 16-21.
- Besag, J. (1986), On the statistical analysis of dirty pictures, *J. Roy. Statist. Soc. B48*, 259-302.
- Borel, C. C., S. A. W. Gerstl, and B. J. Powers (1991), The radiosity method in optical remote sensing of structured 3-D surfaces, *Remote Sens. Environ.* 36, 13-44.
- Bouman, C. A., and M. Shapiro (1994), A multiscale random field model for Bayesian image segmentation, *IEEE Trans. Image Processing*, 3, 162-177.

- Civco, D. L. (1989), Topographic normalization of Landsat Thematic Mapper digital imagery, *Photogramm. Eng. Remote Sens.* 55, 1303-1309.
- Collins, J.B., and C. E. Woodcock (1996), An assessment of several linear change detection techniques for mapping forest mortality using multitemporal Landsat TM data, *Remote Sens. Environ.* 56, 66-77.
- Conese, C., M. A. Gilabert, F. Maselli, and L. Bottai (1993), Topographic normalization of TM scenes through the use of an atmospheric correction method and digital terrain models, *Photogramm. Eng. Remote Sens.* 59, 1745-1753.
- Deering, D.W., E.M. Middleton, and T.F. Eck (1994), Reflectance anisotropy for a spruce-hemlock forest canopy, *Remote Sens. Environ.* 47, 242-260.
- Deusen, P. C. V. (1995), Modified highest confidence first classification, *Photogramm. Eng. Remote Sensing*, 61(4), 419-425.
- Fisher, P. (1997), The pixel, a snare and a delusion, *Int. J. Remote Sens.* 18, 679-685.
- Foody, G. M., N. A. Campbell, N. M. Trodd, and T. F. Wood (1992), Derivation and application of probabilistic measures of class membership from the maximum-likelihood classification, *Photogramm. Eng. Remote Sens.*, 58(9), 1335-1341.
- Foody, G. M., and R. A. Hill (1996), Classification of tropical forest classes from Landsat TM data, *Int. J. Remote Sens.* 17, 2353-2367.
- Franklin, J., T. L. Logan, C. E. Woodcock, and A. H. Strahler (1986), Coniferous forest classification and inventory using Landsat and digital terrain data, *IEEE Trans. Geosci. Remote Sens.* GE-24(1), 139-149.
- Fung, T., and K.-C. Chan (1994), Spatial composition of spectral classes: A structural approach for image analysis of heterogeneous land-use and land-cover types, *Photogramm. Eng. Remote Sen.* 60(2), 173-180.
- Geman S., and D. German (1984), Stochastic relaxation, Gibbs distributions, and the Bayesian restoration of images, *IEEE Trans. Patt. Anal. Machine Intell.* 6, 721-741.

- Gillespie, A. R. (1992), Spectral mixture analysis of multispectral thermal infrared images, *Remote Sens. Environ.* 42, 137-145.
- Gillespie, A. R., M. O. Smith, J. B. Adams, S. C. Willis, A. F. Fischer and D. E. Sabol (1990), Interpretation of residual images: spectral mixture analysis of AVIRIS images, Owens Valley, California, *Proc. Airborne Sci. Workshop: AVIRIS*, JPL Publ. 90-54, pp243-270.
- Gong, P., R. Pu, and B. Yu (1997), Conifer species recognition: An exploratory analysis of in situ hyperspectral data, *Remote Sens. Environ.* 62, 189-200
- Gu, D. , and A. R. Gillespie (1998), Topographic normalization of TM images of forests based on subpixel sun-canopy-sensor geometry, *Remote Sens. Environ.* 64, 166-175.
- Gu, D. , A. R. Gillespie, J. Adams, and R. Weeks (1998), A statistical approach for topographic correction of satellite images by using spatial context information, *IEEE Trans. Geosci. Remote Sens.*, in press.
- Gu, X.F., G. Guyot, and M. Verbrugge (1992), Evaluation of measurement errors in ground surface reflectance for satellite calibration, *Int. J. Remote Sens.* 13, 2531-2546.
- Hall, F. G., D. B. Botkin, D. E. Streble, K. D. Woods, and S. J. Goetz (1991), Large-scale patterns of forest succession as determined by remote sensing, *Ecology* 72(2), 628-640.
- Hapke, B. (1981), Bidirectional reflectance spectroscopy, 1, Theory, *J. Geophys. Res.* 86, 3039-3054.
- Haralick, R. M., and K. S. Shanmugam (1974), Combined spectral and spatial processing of ERTIS imagery data, *Remote Sens. Environ.* 3, 3-13.
- Hill, J., and B. Sturm (1991), Radiometric correction of multitemporal Thematic Mapper data for use in agricultural land-cover classification and vegetation monitoring, *Int. J. Remote Sens.* 12, 1471-1491.

- Hugli, H., and W. Frei (1983), Understanding anisotropic reflectance in mountainous terrain, *Photogramm. Eng. Remote Sens.* 49(5), 671-683.
- Hyppanen, H. (1996), Spatial autocorrelation and optimal spatial resolution of optical remote sensing data in boreal forest environment, *Int. J. Remote Sens.* 17, 3441-3452.
- Irons, J. R., and G. W. Petersen (1981), Texture transform of remote sensing data, *Remote Sens. Environ.* 11, 359-370.
- Itten, K.I., and P. Meyer (1993), Geometric and radiometric correction of TM data of mountainous forested areas, *IEEE Trans. Geosci. Remote Sens.* 31, 764-770.
- Johnson, P. E., M. O. Smith, S. Taylor-George, and J. B. Adams (1983), A semiempirical method for analysis of reflectance spectra for binary mineral mixtures, *J. Geophys. Res.* 88, 3557-3561.
- Justice, C. O., B. L. Markham, J. R. G. Townshend, and R. L. Kennard, Spatial degradation of satellite data, *Int. J. Remote Sens.* 10, 1539-1561.
- Kittler J., and D. Pairman (1985), Contextual pattern recognition applied to cloud detection and identification, *IEEE Trans. Geosci. Remote Sens.* GE-23 (6), 855-863.
- Kleman, J. (1987), Directional reflectance factor distribution of two forest canopies, *Remote Sens. Environ.* 23, 83-86.
- Koch, B., U. Ammer, T. Schneider and H. Wittmeier (1990), Spectroradiometer measurements in the laboratory and in the field to analyse the influence of different damage symptoms on the reflection spectra of forest trees, *Int. J. Remote Sens.* 11, 1145-1163.
- Lambin, E. F., and A. H. Strahler (1994), Indicators of land-cover change for change-vector analysis in multitemporal space at coarse spatial scales, *Int. J. Remote Sens.* 15, 2099-2119.
- Lee, J.-H., and W. D. Philpot (1991), Spectral texture pattern matching: a classifier for digital imagery, *IEEE Trans. Geosci. Remote Sens.* 29, 545-554.

- Li, W.-H. (1997), Significance of multiple scattering in remotely sensed images of natural surfaces, Ph.D. Dissertation, University of Washington, Seattle, Washington.
- Liang, S., and A.H. Strahler (1994), Retrieval of surface BRDF from multiangle remotely sensed data, *Remote Sens. Environ.* 50, 18-30.
- Marceau, D. J., D. J. Gratton, R. A. Fourier, and J.-P. Fortin (1994), Remote sensing and measurement of geographical entities in a forested environment 2. The optical spatial resolution, *Remote Sens. Environ.* 49, 105-117.
- Markham, B. L., and J. R. G. Townshend (1981), Land cover classification accuracy as a function of sensor spatial resolution, in *Fifteenth international symposium on remote sensing of environment*, Ann Arbor, 1075-1090.
- Meyer, P., K. I. Itten, T. Kellenberger, S. Sandmeier, and R. Sandmeier (1993), Radiometric corrections of topographically induced effects on Landsat TM data in an alpine environment, *ISPRS J. Photogramm. Remote Sens.* 48(4), 17-28.
- Milne, B. T. (1992), Heterogeneity as a multiscale characteristic of landscapes, in *Toward a unified ecology: complexity in ecological system series*, edited by T.F.H. Allen and T. W. Hoekstra, Columbia University Press, New York.
- Minnaert, N. (1941), The reciprocity principle in lunar photometry, *Astrophys. J.* 93, 403-410.
- Moffett, J. L., and J. Besag (1996), Spatial and probabilistic classification of forest structures using landsat TM data, presented at the *Second International symposium on spatial accuracy assessment in natural resources and environmental sciences*, Fort Collins, Colorado, May 21-23.
- Mustard, J. F., and C. M. Pieters (1987), Quantitative abundance estimates from bidirectional measurements, *Proc. Lunar Planet. Sci. Conf., 17th, Part 2, J. Geophys. Res.* 92, E617-626.

- Nel, E. M., C. A. Wessman, and T. T. Veblen (1994), Digital and visual analysis of thematic mapper imagery for differentiating old growth from younger spruce-fir stands, *Remote Sens. Environ.* 48,291-301.
- Olsson, H. (1995), Reflectance calibration of thematic mapper data for forest change detection, *Int. J. Remote Sens.* 16, 81-96.
- Pax-Lenney, M., and C. E. Woodcock (1997), The effect of spatial resolution on the ability to monitor the status of agricultural lands, *Remote Sens. Environ.* 61, 210-220.
- Proy, C., D. Tanre, and P.Y. Deschamps (1989), Evaluation of topographic effects in remotely sensed data, *Remote Sens. Environ.* 30, 21-32.
- Ranson, K.J., J.R. Irons, and D.L. Williams (1994), Multispectral bidirectional reflectance of northern forest canopies with the Advanced Solid-State Array Spectroradiometer (ASAS), *Remote Sens. Environ.* 47, 276-289.
- Roberts, D. A., J. B. Adams, and M. O. Smith (1990), Predicted distribution of visible and near-infrared radiant flux above and below a transmittant leaf, *Remote Sens. Environ.* 34, 1-17.
- Roberts, D. A., M. O. Smith, and J. B. Adams (1993), Green vegetation, nonphotosynthetic vegetation, and soil in AVIRIS data, *Remote Sens. Environ.* 44, 255-269.
- Roberts, D. A., M. O. Smith, and J. B. Adams, D. E. Sabol, A. R. Gillespie, and S. C. Willis (1990), Isolating woody plant materials and senescent vegetation from green vegetation in AVIRIS data, *Proc. Airborne Science Workshop*, JPL Publication 90-54, pp42-57.
- Sabol, D. E., JR., J. B. Adams, and M. O. Smith (1992), Quantitative subpixel spectral detection of targets in multispectral images, *J. Geophys. Res.* 97(E2), 2659-2672.

- Schaaf, C. B., X. Li, and A.H. Strahler (1994), Topographic effects on bidirectional and hemispherical reflectances calculated with a geometric-optical canopy model, *IEEE Trans. Geosci. Remote Sens.* 32, 1186-1193.
- Shoshany, M. (1989), Secondary reflection effect on sensor response for a V-shaped Valley, *Int. J. Remote Sens.* 10, 1197-1206.
- Shoshany, M. (1993), Roughness-reflectance relationship of bare desert terrain: an empirical study, *Remote Sens. Environ.* 45, 15-27.
- Skidmore, A. K. (1989), Unsupervised training area selection in forest using a nonparametric distance and spatial information, *Int. J. Remote Sens.* 10, 133-146.
- Smith, J. A., T. L. Lin, and K.J. Ranson (1980), The Lambertian assumption and Landsat data, *Photogramm. Eng. Remote Sens.* 46, 1183-1189.
- Smith, M. O., S. L. Ustin, J. B. Adams, and A. R. Gillespie (1990), Vegetation in deserts: II. A regional measure of abundance from multispectral images, *Remote Sens. Environ.* 31, 1-26.
- St-Onge, B. A., and F. Cavayas (1997), Automated forest structure mapping from high resolution imagery based on directional semivariogram estimates, *Remote Sens. Environ.* 61, 82-95.
- St-Onge, B. A., and F. Cavayas (1995), Estimating forest stand structure from high resolution imagery using the directional variogram, *Int. J. Remote Sens.* 16, 1999-2021.
- Stromberg, W. D., and T. G. Farr (1986), A Fourier-based textural feature extraction procedure, *IEEE Trans. Geosci. Remote Sens.* GE-24, 722-731.
- Syren, P. (1994), Reflectance anisotropy for nadir observations of coniferous forest canopies, *Remote Sens. Environ.* 49, 72-80.
- Taylor, V.R., and L.L. Stowe (1984a), Reflectance characteristics of uniform earth and cloud surfaces derived from Nimbus-7 ERB, *J. Geophys. Res.* 89, 4987-4996.

- Taylor, V.R., and L.L. Stowe (1984b), Atlas of reflectance patterns for uniform earth and cloud surfaces (Nimbus-7 ERB—61 days), *NOAA Tech. Rep. NESDIS 10*, Natl. Oceanic and Atmos. Adm., Washington, D.C.
- Teillet, P.M, B. Guindon, and D. G. Goodenough (1982), On the slope-aspect correction of multispectral scanner data, *Canadian J. Remote Sens.* 8(2), 84-106.
- Tomita, F., and S. Tsuji (1990), *Computer analysis of visual textures*, Kluwer Academic Publishers, Boston.
- Townshend, J. R. G., and C. O. Justice (1995), Spatial variability of images and the monitoring of changes in the normalized difference vegetation index, *Int. J. Remote Sens.* 16, 2187-2195.
- Townshend, J. R. G., and C. O. Justice (1995), The spatial variation of vegetation changes at very coarse scales, *Int. J. Remote Sens.* 11, 149-157.
- Walthall, C. L., J.M. Norman, J.M. Welles, G. Campbell, and B.L. Blad (1985), Simple equation to approximate the bidirectional reflectance from vegetation canopies and bare soil surfaces, *Appl. Opt.* 24, 383-387.
- Weeks, R., M. Smith, K. Pak, and A. Gillespie (1997), Inversion of SIR-C and AIRSAR data for the roughness of geological surfaces, *Remote Sens. Environ.* 59, 383-396.
- Weeks, R. J., M. Smith, K. Pat, W.-H. Li, A. Gillespie, and Bi. Gustafson (1996), Surface roughness, radar backscatter, and visible and near-infrared reflectance in Death Valley, California, *J. Geophys. Res.* 101, 23077-23090.
- Woodcock, C. E., and A. H. Strahler (1987), The factor of scale in remote sensing, *Remote Sens. Environ.* 21, 311-322.
- Wulder, M. A., E. F. LeDrew, S. E. Franklin, and M. B. Lavigne (1998), Aerial image texture information in the estimation of northern deciduous and mixed wood forest leaf area index (LAI), *Remote Sens. Environ.* 64, 64-76.

Zenzo, S. D., R. Bernstein, S. D. Degloria, and H. G. Kolsky (1987). Gaussian maximum likelihood and contextual classification algorithms for multicrop classification, *IEEE Trans. Geosci. Remote Sens.* GE-25 (6). 805-814.

VITA

Degui Gu
University of Washington
1998

PERSONAL INFORMATION

Date of Birth: May 24, 1966

Place of Birth: Heilongjiang, China

EDUCATION

Ph.D. Geophysics Program, University of Washington, Seattle, Washington,
June, 1998.

M.S. Seismology and Geology, Institute of Geology, State Seismological
Bureau, Beijing, China. December, 1988.

B.S. Department of Geophysics, Peking University, Beijing, China. July,
1986.

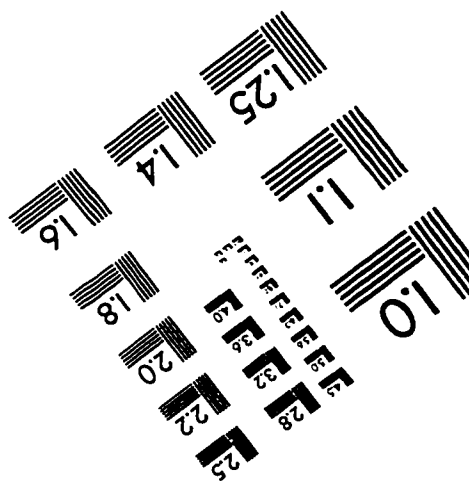
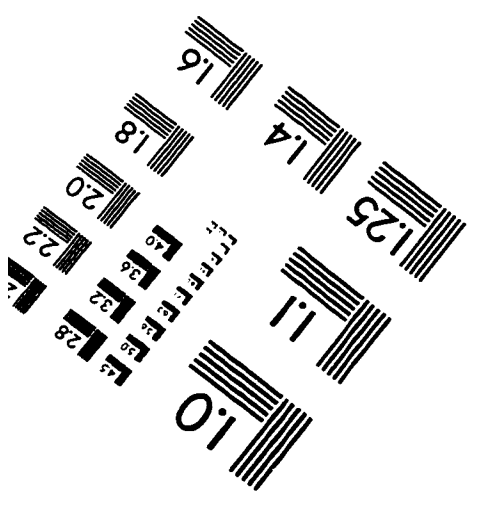
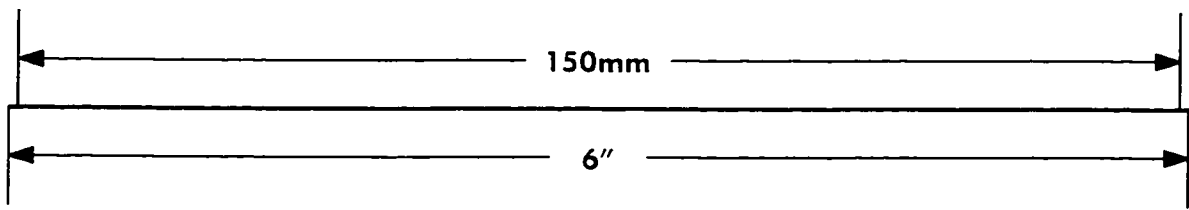
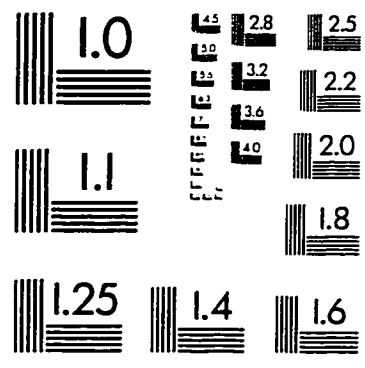
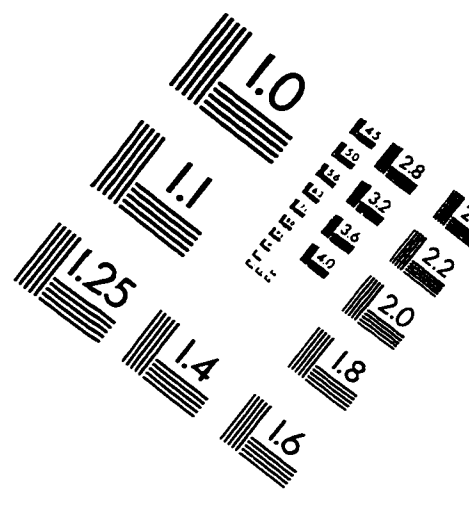
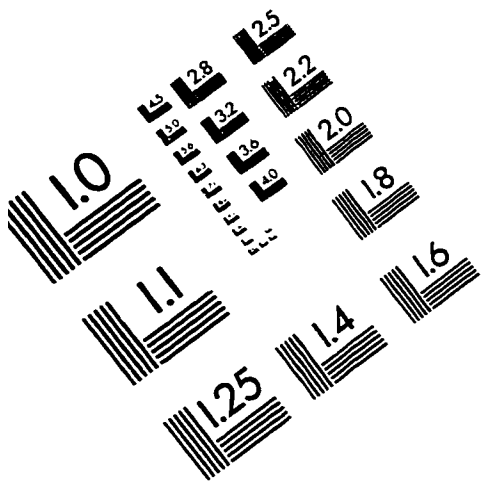
PUBLICATIONS

Gu, D., A. Gillespie, J. Adams and R. Weeks, 1998, A statistical approach for
topographic correction of satellite images by using spatial contextual
information, *IEEE Trans. Geosci. Remote Sens.*, in press.

Gu, D. and A. Gillespie, 1998, Topographic normalization of TM images of
forests based on subpixel sun-canopy-sensor geometry, *Remote Sens.
Environ.* 64, 166-175.

- Gillespie, A., J. Adams, M. Smith, D. Gu, D. Sabol, and J. Zukin, 1995, Forest mapping potential of ASTER, *J. Remote Sens. Soc. Japan*, 15(1),62-71
- Gillespie, A., W.-H. Li, D. Gu, J. Adams, A. Kahle, 1995, Measuring change in forests with EOS/ASTER (Abstract), *EOS Trans. AGU*, 76(46), 132.
- Dong, R., D. Gu and H. Ran, 1993, Application of renewal process and probability assignment model to calculating earthquake occurrence probability for potential seismic source areas (in Chinese), *Seismology and Geology*, Vol. 15, No. 3, 239-246.
- Zhang, Y. and D. Gu, 1993, Regional geological settings of great earthquakes in the western China and its adjacent areas, in *CONTINENTAL EARTHQUAKES-Selected Papers of the Second International Conference on Continental Earthquakes, IASPEI Publication Series for the IDNDR*, Vol. 3, 376-383, Seismological Press, Beijing, China.
- Gu, D., 1992, On earthquake recurrence and its uncertainty (in Chinese), *technical report*, Institute of Geology, State Seismological Bureau, Beijing, China.
- Gu, D. and Y. Zhang, 1990, The probability distribution model and its application to earthquake risk analysis (in Chinese), *Earthquake Research in China*, Vol. 6, No. 1, 39-46.

IMAGE EVALUATION TEST TARGET (QA-3)



APPLIED IMAGE, Inc
1653 East Main Street
Rochester, NY 14609 USA
Phone: 716/482-0300
Fax: 716/288-5989

© 1993, Applied Image, Inc., All Rights Reserved